Engineering microbial rhodopsins to expand the optogenetic toolkit

Dissertation Advisor: Professor Adam E. Cohen Veena Venkatachalam

Engineering microbial rhodopsins to expand the optogenetic toolkit

Abstract

Cellular lipid membranes can – and often do – support a transmembrane electric field, serving as biological capacitors that maintain a voltage difference between their two sides. It isn't hard to see why these voltage gradients matter; the electrical spiking of neurons gives rise to our thoughts and actions, and the voltage dynamics of cardiomyocytes keep our hearts beating. Studies of bioelectricity have historically relied on electrode-based techniques to perturb and measure membrane potential, but these techniques have inherent limitations. I present new optogenetic methods of studying membrane potential that will broaden the scope of electrophysiological investigations by complementing traditional approaches.

I introduce the microbial rhodopsin Archaerhodopsin-3 (Arch), a transmembrane protein from *Halorubrum sodomense*. The fluorescence of Arch is a function of membrane potential, allowing it to serve as an optical voltage reporter. We use time-dependent pump-probe spectroscopy to interrogate the light- and voltage- dependent conformational dynamics of this protein, to elucidate the mechanism of voltage-dependent fluorescence in Arch.

I then present two new methods for imaging voltage using engineered variants of Arch. Both techniques take advantage of the unique photophysical properties of Arch(D95X) mutants. The first method, Flash Memory, records a photochemical imprint of the activity state – firing or not firing – of a neuron at a

user-selected moment in time. The Flash Memory technique decouples the recording of neural activity from its readout, and can potentially allow us to take large-scale snapshots of voltage (e.g. maps of activity in a whole mouse brain). The second method allows for the quantitative optical measurement of membrane potential. This technique overcomes the problems that typically hinder intensity-based measurements by encoding a measurement of voltage in the time domain.

Finally, I present a method to visualize cellular responses to changes in membrane potential. I engineer mutants of Channelrhodopsin-2 (ChR2), a light-gated cation channel from *Chlamydomonas reinhardtii* that is used for optical control of neural activity, and use these optogenetic actuators in conjunction with GFP-based sensors to study the activity-dependent behavior of cultured neurons.

Table of Contents

Citations to Previously Published Work

Chapter 1 is partially adapted from [1]:

> Park J*, Werley CA*, Venkatachalam V, Kralj JM, Dib-Hajj SD, Waxman SG, Cohen AE [*equal contribution]. (2013) Screening fluorescent voltage indicators with spontaneously spiking HEK cells. *PLoS One* 8:e85221.

Chapter 2 is adapted from [2]:

> Maclaurin D*, Venkatachalam V*, Lee H, Cohen AE [*equal contribution] (2013) Mechanism of voltage-sensitive fluorescence in a microbial rhodopsin. *Proc Natl Acad Sci USA* 110:5939-5944.

Chapter 3 is adapted from [3]:

> Venkatachalam V, Brinks D, Maclaurin D, Hochbaum DR, Kralj JM, Cohen AE (2014) Flash memory: photochemical imprinting of neuronal action potentials onto a microbial rhodopsin. *J Am Chem Soc* 136:2529-2537.

Chapter 4 is adapted from [4]:

> Hou JH, Venkatachalam V, Cohen AE (2014) Temporal Dynamics of Microbial Rhodopsin Fluorescence Reports Absolute Membrane Voltage. *Biophys J* 106:639-648.

Chapter 5 is adapted from a manuscript currently in submission:

> Venkatachalam V, Cohen AE (2014) Imaging GFP-based reporters in neurons with mutli-wavelength optogenetic control. *Submitted*.

Acknowledgments

I think that the light-induced conformational gymnastics of microbial rhodopsins make them some of the coolest proteins around, and I have enjoyed exploring their (very complicated) world over the past few years. However, the research that I will share with you in this thesis was not the highlight of my time in graduate school. Rather, it was the people that I've met over the past four years who have made this experience so unique and amazing. If I had to choose between the knowledge I've gained over the course of my PhD and the wonderful friends that I've made during my tenure in the Cohen Lab, there would be absolutely no contest. (Sorry, Arch!)

I would like to start with a sincere thank you to my advisor, Adam Cohen. His enthusiasm for learning is infectious, and the way in which he ignores the barriers between traditional scientific disciplines has been inspirational. He has created an environment where physicists, chemists, biologists, and neuroscientists work together, and he not only keeps track of projects spanning these diverse disciplines, but also manages to guide them forward with his uncanny scientific intuition. I have yet to figure out how he manages to do all that he does; but I am lucky to have benefited from Adam's dedication to the lab and his willingness to sit down and discuss puzzling or interesting results at any time of the day or night. Adam is a gifted scientist and a caring mentor, and I am glad that I had the chance to work with and learn from him.

I would also like to thank my labmates in the Cohen Lab for being the world's best colleagues. To start out, I'd like to thank the original "Team PROPS": Joel Kralj,

Daniel Hochbaum, and Adam Douglass. Joel was the first rhodopsin photophysicist of the group, and we had a lot of fun patching Arch(D95X) mutants together when I joined the lab. This work is presented in Chapter 1. Daniel has also been a friend and colleague from the start, and I couldn't imagine going through my Ph.D. without him. In addition to lighting up the lab with his sunny personality, he routinely invests a lot of time and effort to make things work (often thanklessly). I benefitted immensely from his efforts, particularly his work on optimizing primary neuronal culture.

I want to emphasize the substantial contributions of those who should be listed as co-authors on this thesis, all of whom taught me a great deal. In particular, I am grateful to Dougal Maclaurin, my buddy in studying the photophysics of WT Arch. We pondered many confusing photocycle topologies as we waded through the swamp of photophysics over the course of 2012, and I think the journey would have been quite maddening if I hadn't shared it with someone as good-natured and intelligent as Dougal. Dougal helped me grow comfortable with homebuilt microscopes and all the instrumentation associated with them. The work that we did together is presented in Chapter 2. In addition, Dougal and I started the Flash Memory project together.

I also thank Daan Brinks, who joined me on the Flash Memory project shortly after he joined the lab. Daan and I spent a lot of quality time together patching cells and designing waveforms to probe the photophysics of Arch(D95X) mutants. Daan was kind enough to let me pull things together and write the first draft of our manuscript while he moved on to tackle the world of two-photon voltage imaging, but the data presented in our paper was a true collaborative effort. Our work is presented in Chapter 3.

I thank Jennifer Hou for pushing through the infamous summer of absolute voltage with me. Her drive, work ethic, and attention to detail were inspirational. Despite the fact that I was supposedly teaching her electrophysiology, I am pretty sure that I wound up learning a lot more from her than she learned from me! The work that I did with Jen is presented in Chapter 4.

Several other lab members directly contributed to the work in this thesis. Hohjai Lee performed the transient absorption experiments of Chapter 2 with Dougal and me. Peng Zou performed the bistability screen in Section 3.5 with me. Christopher Werley designed and built the microscope that I used to acquire the data in Chapter 5. Lucy Rosenbaum, Tony Shen, Vedha Nathan, Jonathan Gootenberg, and Katherine Williams helped with molecular biology, and Nik Smedemark-Margulies and Vaibhav Joshi provided valuable assistance with primary neuronal cell culture. Alexander Fields kindly gave me his thesis to use as a template for this thesis.

Although their work isn't presented here, I would like to thank all the members of the Cohen lab with whom I overlapped for camaraderie and stimulating discussions: Sami Farhi, Sabrina Leslie, Yiqiao Tang, Min Ju Shon, Nan Yang, Halil Bayraktar, Alexander Fields, Jeehae Park, Miao-Ping Chien, Bogdan Bintu, Xin Tang, Shan Lou, Yoav Adam, Stefano Boccardo, Emil Hansson, Alexander Yi, Jeff Fosdick, and Maggie Kenar.

I thank Jim Hogle and Michele Jakoulov of the Harvard Biophysics Program for their guidance and support, and for organizing retreats, clambakes, dinners, and barbecues that provided some much-appreciated opportunities for both education and relaxation. I also thank everyone at Harvard's MD-PhD program for their support during

these grad school years. I thank my preliminary qualifying exam committee members – Gary Yellen, Nao Uchida, and Emily Balskus – for their kindness and patience during my PQE, and I thank my dissertation advisory committee members – Gary Yellen, Venkatesh Murthy, and Nao Uchida – for their advice and encouragement during the final stages of my PhD. I thank Florian Engert for joining Gary Yellen and Venkatesh Murthy on my defense committee.

I wouldn't be where I am today without the support of my family and friends. Matthew, thanks for supporting me throughout this crazy adventure. Vivek, I am glad that my lab was across the street / down the road from you; it was nice knowing that my smarter, wiser, older brother was never more than 5 minutes away. Mom and dad – thank you, for everything!

I received funding from an NIH Medical Scientist Training Program (MSTP) grant T32GM07753-33 and a Herchel Smith Fellowship. The work in this thesis was also supported by PECASE award N00014-11-1-0549, the Harvard Center for Brain Science, NIH grants 1-R01-EB012498-01 and New Innovator grant 1-DP2-OD007428, and the Harvard/MIT Joint Research Grants Program in Basic Neuroscience.

Part I

Developing voltage imaging techniques

1
Introduction

Archaerhodopsin-3 (Arch, Uniprot P96787) is a microbial rhodopsin derived from the Dead Sea microorganism *Halorubrum sodomense*. Like all microbial rhodopsins, Arch contains seven transmembrane alpha helices with the chromophore retinal covalently bound via a Schiff base to a lysine in the protein core. In the wild, Arch serves as a light-driven outward proton pump, capturing solar energy for its host [5]. Recently, neuroscientists realized that we could exploit this natural function of Arch to control membrane potential with light. Indeed, upon expression in neurons, Arch acts as an optogenetic neural silencer: illumination with green light generates a hyperpolarizing photocurrent, which suppresses neural firing [6].

Several years ago, our lab discovered another interesting and incredibly convenient property of Arch: voltage-dependent fluorescence. At high voltages, Arch fluoresces more brightly than at low voltages. By expressing Arch in rat hippocampal neurons, my predecessors in the Cohen lab made the first single-trial optical recordings of action potentials in mammalian neurons [7].

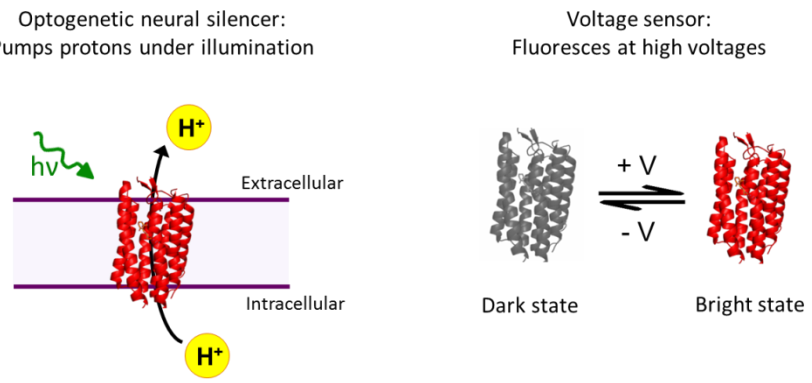

Figure 1-1. Archaerhodopsin-3 has two roles in optogenetics. Arch is well known as a light-driven outward proton pump that can hyperpolarize cells (left). For this reason, it has been widely used as a light-driven neural silencer. In our lab, we focus on a less well-known property of Arch: voltage-dependent fluorescence (right). If the proton-pumping ability of Arch is broken, it can be used as a non-perturbative voltage sensor, enabling optical recording of action potentials in neurons.

In Part I of this thesis, I expand upon our lab's early work by characterizing the mechanism of voltage-sensitive fluorescence in Arch (Chapter 2), and engineering new voltage-imaging techniques inspired by the unique photophysics of Arch(D95X) mutants (Chapters 3 & 4). In this brief introductory chapter, I describe the preliminary experiments that motivated me to explore Arch photophysics in greater depth.

1.1 Preliminary attempts to engineer better voltage sensors

Archaerhodopsin-3 is an excellent voltage sensor for many reasons, including remarkable photostability, a sub-millisecond response time, and high sensitivity [8]. However, the unmodified wild-type (WT) protein has some shortcomings. WT Arch translocates protons out of the cell, and therefore lowers membrane potential, under illumination with imaging light at 640 nm (Fig. 1-1). While this is why Arch is desirable as

an optogenetic silencer, this property becomes highly undesirable when Arch is used as a voltage sensor. In addition, the fluorescence of Arch is dim compared to GFP, making it difficult to visualize Arch on many microscopes. (There is a lot to say about the brightness of Arch, but I will defer that discussion to Chapter 2 of this thesis; for now, it is enough to know that WT Arch is functionally ~50x dimmer than GFP.) My first project in the lab was to engineer better versions of Arch. Our design objective was to modify the protein to make it brighter and non-perturbative, while maintaining its voltage sensitivity, speed, and photostability.

1.1.1 Selecting an opsin

Before launching into a screen of Arch mutants, I wanted to double check that we were starting with the best possible protein backbone. Our lab had previously characterized the voltage sensitivity of Archaerhodopsin-3, so it was the obvious choice; but we had never looked at Archaerhodopsin-1, which is 93% homologous to Arch-3. I was curious to see whether Arch-1 could also act as a voltage sensor; if so, was it even better than Arch-3? I compared the voltage sensitivity of Arch-1 to that of Arch-3 under red illumination (640 nm, 500 W/cm^2). Both proteins were expressed in HEK-293T cells, and fluorescence was recorded on an EMCCD camera while transmembrane voltage was controlled using patch-clamp electrophysiology. The results of this experiment are shown in Fig. 1-2.

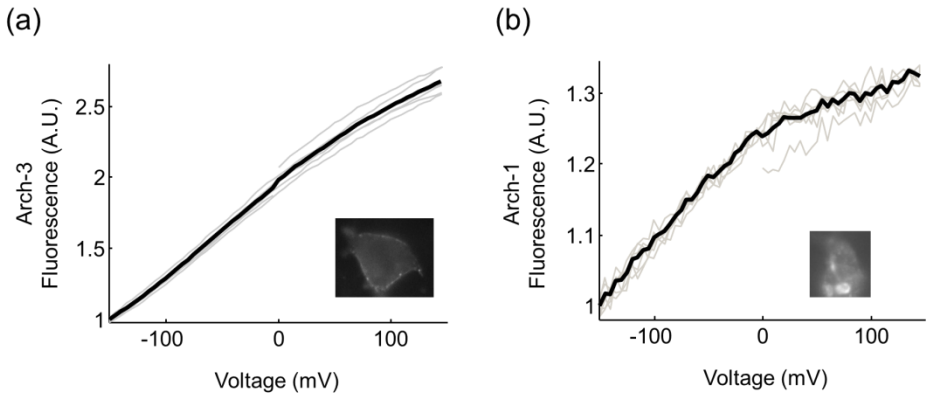

Figure 1-2. Fluorescence vs. voltage for both (a) Archaerhodopsin-3 and (b) Archaerhodopsin-1. Fluorescence is normalized to baseline fluorescence at -150 mV. Inset shows fluorescence of a representative cell expressing each sensor. Archaerhodopsin-3 shows better voltage sensitivity and membrane trafficking than Arch-1.

Arch-3 showed superior membrane localization to Arch-1, and was ~5 times more voltage sensitive than Arch-1. Thus, we abandoned Arch-1, and did not pursue further characterization of this protein. Throughout this thesis, "Arch" is used to refer solely to Archaerhodopsin-3.

Although Arch-1 turned out to be suboptimal, this experiment did confirm what we already suspected – voltage-sensitive fluorescence is not a very unique property in the world of microbial rhodopsins. A thorough screen of all proton-pumping microbial rhodopsins might reveal a multitude of excellent voltage sensors.

1.1.2 Generation of an Arch(D95X) mutant library

After selecting Arch-3 as our backbone for mutagenesis, we needed to generate a library of new, and hopefully better, voltage sensors. Prior studies had shown that mutation of residue 95 from aspartate to asparagine would abolish proton pumping in Arch, so we focused our efforts on modification of this key residue [7].

A library of Arch(D95X) mutants was generated by performing saturation mutagenesis of residue Asp95 in Archaerhodopsin-3 in the pET-28b vector using the primers D95X_FWD:

5'-CAGGTACGCC**NNK**TGGCTGTTTACCACCCCACTTCTG

and D95X_REV:

5'-GTAAACAGCCA**MNN**GGCGTACCTGGCATAATAGATATCCAACATTTCG.

The 25 μL saturation mutagenesis reaction contained: 50 ng template DNA (WT Arch in pET-28b); 60 nM of each primer (D95X_FWD and D95X_REV); 0.5 μL PfuUltra high-fidelity DNA polymerase (Stratagene); 2.5 μL of 10x PfuUltra buffer (Stratagene); and 300 μM dNTPs. The reaction conditions were: (1) 95 ºC for 5 minutes; (2) 95 ºC for 45 s; (3) 53 ºC for 50 s; (4) 72 ºC for 10 minutes; (5) repeat steps 2-4 24 times; (6) 72 ºC for 10 minutes. These constructs were used for expression in *E. coli*.

To express mutants in HEK-293T cells, the Arch(D95X) library was cloned (using Gibson Assembly, New England Biolabs) into a lentiviral mammalian expression vector containing a ubiquitin promoter (Addgene plasmid 22051 cut with the restriction enzymes BamHI and AgeI [9]). The library consisted of Arch(D95X) fused to C-terminal eGFP. These constructs were used for all experiments in HEK-293T cells.

An inverted epifluorescence microscope was used to image both E. coli and HEK cells. Arch was excited at 640 nm (~500 W/cm^2), while GFP was excited at 473 nm (~1 W/cm^2). Fluorescence emission was recorded on an EMCCD. E. coli were imaged on 1% agarose pads in minimal media, as described in ref. [10]. HEK-293T cells expressing different Arch(D95X) mutants were imaged in Tyrode's buffer (125 mM NaCl, 2 mM KCl,

3 mM $CaCl_2$, 1 mM $MgCl_2$, 10 mM HEPES, and 30 mM glucose at pH 7.3; adjusted to 305–310 mOsm with sucrose), and their membrane potential was controlled via whole-cell voltage clamp. The control voltage was a triangle wave between -150 mV and +150 mV, for 3 cycles at a sweep rate of 25 mV/s. All experiments were performed at 25° C.

1.1.3 Results of Arch(D95X) screen for voltage sensitivity in E. coli

Our initial plan was to screen mutants for brightness and voltage sensitivity in E. coli. To test the feasibility of this method, we expressed WT Arch in E. coli and visualized fluorescence from some of these cells under excitation at 640 nm (500 W/cm^2). We hoped that by imaging Arch fluorescence as these E. coli underwent transient spontaneous depolarization (see ref. [10]), we could get a sense of how good our voltage indicator was. Typical results from six "blinking" cells expressing WT Arch are shown in Fig. 1-3.

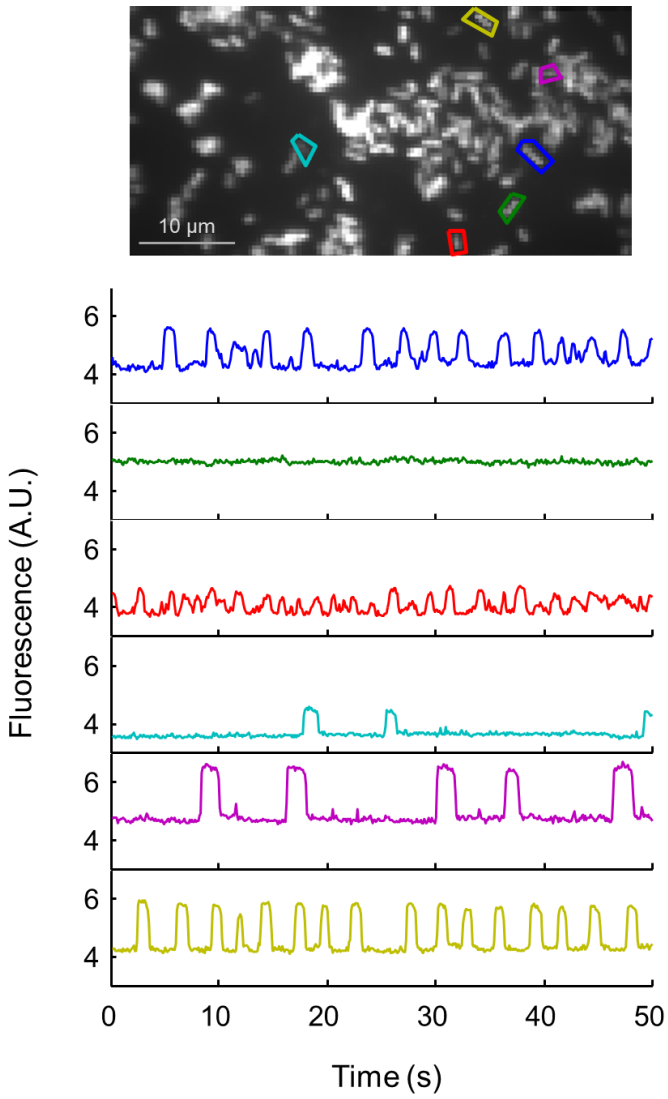

Figure 1-3. Fluorescence imaging of WT Arch in E. coli. Image of E. coli expressing WT Arch (top), with fluorescence traces vs. time of 6 selected cells (bottom). We initially hoped to screen for better Arch mutants in E. coli, but cell-to-cell variability in voltage dynamics and Arch expression levels made this difficult.

Our exploration of this screening method (Fig. 1-3) revealed several possible pitfalls. We were concerned by the heterogeneity of spontaneous voltage dynamics in E. coli. As Fig 1-3 shows, the magnitude of a blink – while generally consistent within a given cell – was not consistent from cell to cell, even when all cells were expressing the same sensor. This heterogeneity would confound our efforts to quantify the voltage

sensitivity of individual sensors. Another issue that worried us was the cell-to-cell variability in protein expression levels, which made it difficult to quantify the brightness of each sensor. In an attempt to control for variable expression levels, we expressed an Arch-GFP fusion protein in E. coli, with the goal of using GFP fluorescence as a proxy for overall protein expression level. However, the fusion protein was poorly tolerated by E. coli.

In addition to these concerns about the robustness of E. coli as a screening platform, we feared that the vastly different lipid compositions of bacterial and mammalian cell membranes might lead us to select for sensors that were optimized for bacterial use, rather than neuronal expression. Additionally, we were unable to measure response speed, photocurrent, or membrane trafficking of our sensors in E. coli. For all of these reasons, we decided to characterize our 20 Arch variants using patch-clamp electrophysiology in mammalian cells. This method, while labor-intensive, could provide us with quantitative information about voltage sensitivity for all of our putative sensors, along with measurements of their brightness, photocurrent, membrane trafficking, and response speed.

1.1.4 Results of Arch(D95X) screen in HEK-239T cells

The results of our Arch(D95X) screen in HEK-293T cells are summarized in Figure 1-4. Most mutants generated a negligible photocurrent (<5 pA under 500 W/cm^2 illumination at 640 nm, compared with >100 pA for the WT protein under the same illumination conditions), with the notable exception of Arch(D95E), which generated a photocurrent comparable to that of the WT protein. Mutation of Asp95 slowed down

the speed of the protein's response to a step in voltage, with only Arch(D95E) and Arch(D95G) responding as fast as the WT protein (achieving 80% of their maximal fluorescence response to a voltage step between -70 mV and +30 mV in <5 ms).

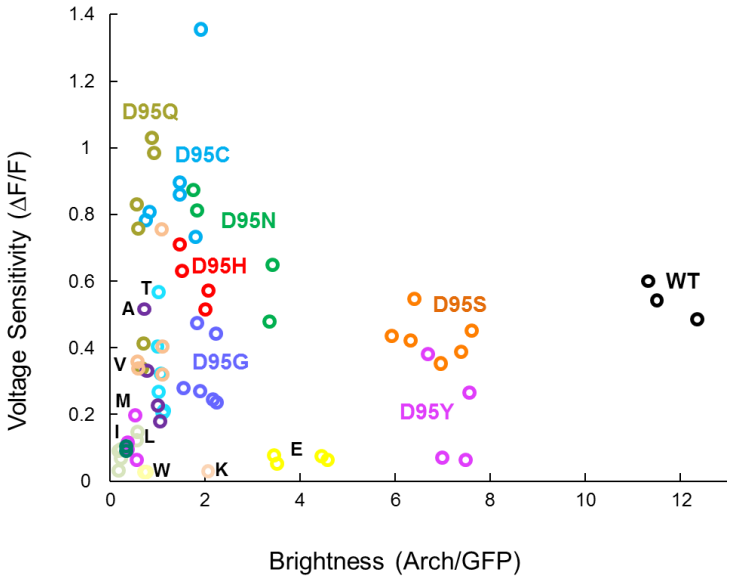

Figure 1-4. Voltage Sensitivity vs. Brightness of Arch(D95X) mutants. Voltage sensitivity was calculated as the change in protein fluorescence upon increasing the membrane potential from -100 mV to +100 mV, normalized to the fluorescence at -100 mV. Brightness was calculated by taking the ratio between Arch fluorescence at 0 mV and eGFP fluorescence. Arch was illuminated at 640 nm (500 W/cm^2); GFP was illuminated at 473 nm (~1 W/cm^2). The x-axis is in arbitrary units.

Although we tried to be rigorous in our screening of these mutants, several issues came up. We suffered from some dish-to-dish variation in the health of our HEK cells over the course of this study, which could have influenced our measurements of voltage sensitivity and brightness. For example, the voltage sensitivity of the WT protein is underestimated by Fig. 1-4, which places it at 60% [WT Arch usually shows a voltage sensitivity of at least 100% (see Fig 1-2a)]. We also failed to use completely flat-field illumination, which may have influenced the accuracy of our brightness measurements; this error could be as high as ~30%.

Despite these flaws, our screen still identified sensitive and non-perturbative mutants of Arch that allowed us to visualize changes in membrane potential with millisecond time resolution. Unfortunately, no mutant was more fluorescent than the WT protein, and any observed increases in sensitivity relative to the WT protein were small.

1.2 Arch(D95X) mutants have incredibly interesting photophysical properties

In the course of our screen of Arch(D95X) mutants, we discovered some puzzling photophysical properties of these mutants. These observations, presented below, hint at the complex light- and voltage- dependent dynamics of Arch.

1.2.1 Voltage and illumination influence Arch dynamics in non-intuitive ways

In general, we were struck by the variation in protein behavior that arose from mutation of a single amino acid. For example, the shape of the fluorescence vs. voltage (F vs. V) curve is not the same for all mutants (Fig. 1-5). The region of peak voltage sensitivity is similar for WT Arch, Arch(D95H), and Arch(D95S), with these mutants showing maximum (and nearly linear) voltage sensitivity over the physiologic range of -100 mV to +40 mV. Other mutants show peak sensitivity at higher membrane potentials; these mutants include Arch(D95L), Arch(D95M), and Arch(D95Q).

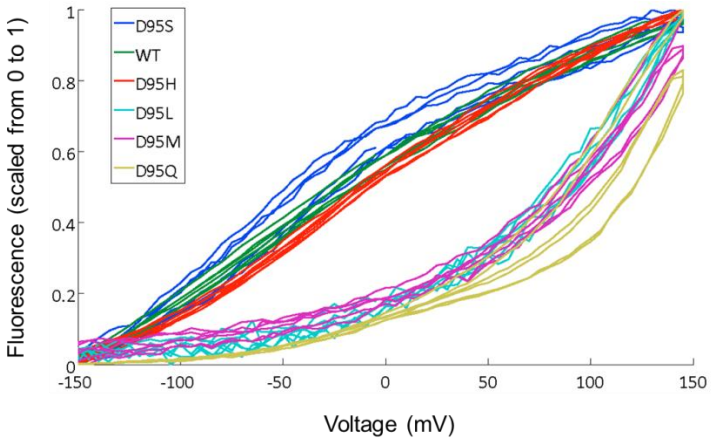

Figure 1-5. Fluorescence vs. voltage curves for six different Arch mutants. All traces are normalized to their maximal values to highlight the differences between the shapes of these curves; note that the region of peak voltage sensitivity varies among these mutants.

For some mutants, the story is even stranger. Arch(D95Y) has a non-monotonic F vs. V curve; fluorescence increases as a function of voltage between -100 mV and +25 mV, but this relationship reverses at higher voltages (Fig. 1-6). Fluorescence is also affected in non-intuitive ways by adding illumination light of a different wavelength. Addition of 473 nm excitation light to 640 nm excitation light restored monotonic voltage sensitivity in Arch(D95Y).

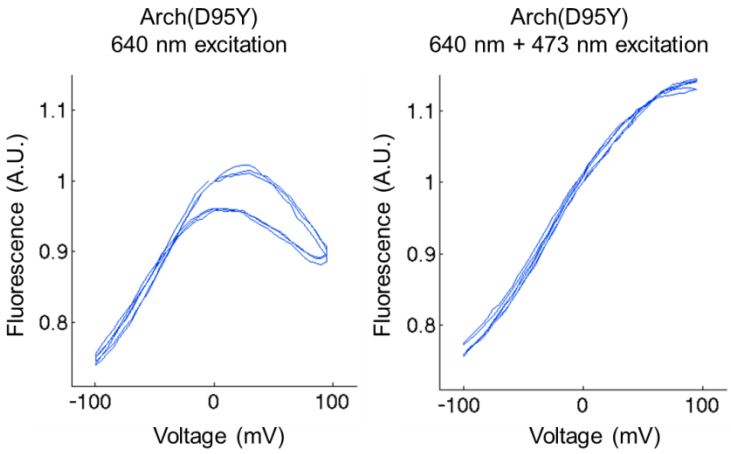

Figure 1-6. Blue light restores monotonic voltage sensitive fluorescence in Arch(D95Y). Fluorescence vs. voltage for Arch(D95Y) under 640 nm illumination alone (left), and under 640 nm illumination + 473 nm illumination (right).

For fun, we varied the temporal dynamics of illumination and voltage while imaging some mutants, as in Figure 1-7. Intriguingly, we noticed that the initial fluorescence of some Arch mutants (e.g. Arch(D95N), Fig. 1-7) is a function of the membrane voltage during the previous illumination period. This finding motivated us to develop the Flash Memory technique of Chapter 3.

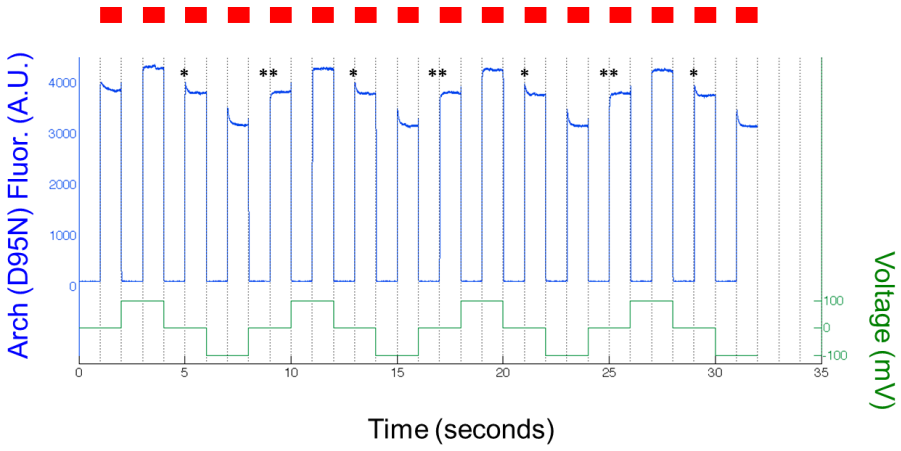

Figure 1-7. Fluorescence of Arch(D95N) in response to a time-varying voltage and illumination protocol. Fluorescence of Arch(D95N) (blue trace) when illuminated with flashes of 640 nm light (red bars), while voltage is varied between 0, +100, and -100 mV (green trace at bottom). Note the difference in fluorescence at 0 mV between the timepoints indicated by (*) vs. those indicated by (**); this finding is explored in great detail in Chapter 3.

1.2.2 Next steps

The results presented in this introduction offer a cursory glimpse into the fascinating world of Arch. Heterologous expression of this sensor in E. coli allows us to watch bacteria blink, and expression of Arch in neurons allows us to see action potentials. In addition, mutation of a single amino acid in Arch (Aspartate 95) completely changes the behavior of this protein.

Before continuing to screen for better voltage sensors, we decided to take a closer look at the mechanism of Arch. We were intrigued by the complex photophysical behavior of this protein, and we hoped that expanding our understanding of voltage-sensitive fluorescence in Arch could guide our efforts to engineer better voltage sensors. The studies that we did to elucidate the mechanism of voltage sensitivity in WT Arch are presented in the next chapter. For those who are fascinated by Figure 1-7, do not

despair; I will come back to explore some of the interesting properties of Arch(D95X) mutants in Chapters 3 and 4.

2
Photophysics of Archaerhodopsin-3

An understanding of the mechanism underlying voltage-sensitive fluorescence in micrpbial rhodopsins would aid in the design of improved voltage indicators. We asked: what states can the protein adopt, and which states are fluorescent? How does membrane voltage affect the photostationary distribution of states? Here we present a detailed spectroscopic characterization of Archaerhodopsin-3 (Arch). We performed fluorescence spectroscopy on Arch and its photogenerated intermediates in *E. coli* and in single HEK 293 cells under voltage-clamp conditions. These experiments probed the effects of time-dependent illumination and membrane voltage on absorption, fluorescence, membrane current, and membrane capacitance. The fluorescence of Arch arises through a sequential three-photon process. Membrane voltage modulates protonation of the Schiff base in a 13-*cis* photocycle intermediate ($M \rightleftharpoons N$ equilibrium); not in the ground state as previously hypothesized. We present experimental protocols for optimized voltage imaging with Arch and we discuss strategies for engineering improved rhodopsin-based voltage indicators.

2.1 Introduction

Optical recording of membrane potential promises new insights into the individual and collective dynamics of neurons [11, 12], cardiac cells [13], developing

embryos [14] and even microbes [15]. Despite decades of effort [12, 16, 17], development of effective voltage indicators remains a challenge. We recently discovered that the endogenous fluorescence of some microbial rhodopsin proteins responds sensitively and quickly to changes in membrane voltage [7, 10]. Yet the mechanisms by which these proteins fluoresced and sensed voltage remained obscure. A detailed photophysical understanding of GFP proved essential to its optimization and diversification [18]. Thus we adopted a similar approach for Arch. The aims of this chapter are (1) to identify optimal imaging conditions for Arch and (2) to explain how Arch functions as a voltage indicator.

Illumination with orange or red light excites Arch fluorescence; emission is in the near infrared, peaked at 710 nm [7]. Fluorescence is sensitive to membrane voltage; with excitation at 640 nm, fluorescence increased two-fold from -150 mV to +150 mV, with a response time of ~0.6 ms. However, Arch has two undesirable attributes as a voltage indicator. First, the fluorescence is very dim, requiring intense laser illumination to be detectable. Second, illumination of Arch slightly perturbs the membrane potential: under typical illumination for imaging (640 nm, 230 W/cm2), Arch generates an outward photocurrent in neurons of 34 ± 7 pA (n = 7 cells), which hyperpolarizes the membrane by 6.2 ± 1.1 mV. A mechanistic understanding of Arch could guide efforts to engineer improved performance.

(a)

```
Ar 1     MDPIALTAAVGA DLLGDGRPET LWLGIGTLLM LIGTFYFIVK GWGVTDK 49
Ar 3    -MDPIALQAGY-- DLLGDGRPET LWLGIGTLLM LIGTFYFLVR GWGVTDK 47
BR      MLELLPTAVEGVS QAQITGRPEW IWLALGTALM GLGTLYFLVK GMGVSDP 37
          :: :.  .     :    ****  :**.:** **  :**:**:*: * **:*

EAR EYYSITILVP GIASAAYLSM FFGIGLTEVQ VGSEMLDIYY ARYADWL 99
DAR EYYAVTILVP GIASAAYLSM FFGIGLTEVT VGGEMLDIYY ARYADWL 97
DAK KFYAITTLVP AIAFTMYLSM LLGYGLTMVP FGGEQNPIYW ARYADWL 87
:*: ::*::* *** .** : **** ::* *** *  .*.*   **: *******

FTT PLLLLDLALL AKVDRVSIGT LVGVDALMIV TGLVGALSHT PLARYTW 149
FTT PLLLLDLALL AKVDRVTIGT LVGVDALMIV TGLIGALSHT AIARYSW 147
FTT PLLLLDLALL VDADQGTILA LVGADGIMIG TGLVGALTKV YSYRFVW 137
*** ********** ...*: :* : ***.*.:**  ***:***::.    *: *

WLF STICMIVVLY FLATSLRAAA KERGPEVAST FNTLTALVLV LWTAYPI 199
WLF STICMIVVLY FLATSLRSAA KERGPEVAST FNTLTALVLV LWTAYPI 197
WAI STAAMLYILY VLFFGFTSKA ESMRPEVAST FKVLRNVTVV LWSAYPV 187
* : ** .*: :** .*  .: : * :.  ****** *:.*  :.:* **:***:

LWI IGTEGAGVVG LGIETLLFMV LDVTAKVGFG FILLRSRAIL GDTEAPE 249
LWI IGTEGAGVVG LGIETLLFMV LDVTAKVGFG FILLRSRAIL GDTEAPE 247
VWL IGSEGAGIVP LNIETLLFMV LDVSAKVGFG LILLRSRAIF GEAEAPE 237
:*: **:****:*  *.******** ***:****** :********: *::****

PSA GAEASAAD- 260
PSA GADVSAAD- 258
PSA GDGAAATSD 249
*** *  .:*:.
```

(b)

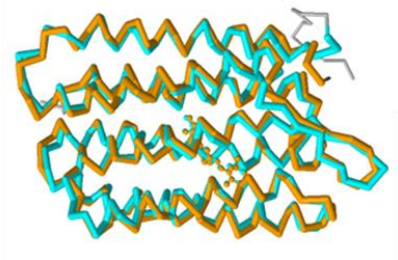

(c)

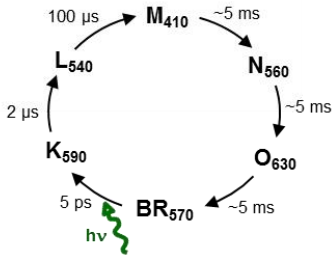

Figure 2-1. Comparison of Arch-3, Arch-1, and Bacteriorhodopsin. (a) Sequence alignment via ClustalW2. Arch-1 (Uniprot P69051) and Arch-3 (Uniprot P96787) share 93% amino acid identity. Arch-3 and BR share 61% amino acid identity. All key residues in the proton-pumping pathway (yellow) are shared except for S193 in BR (T203 in Arch-3). This residue is part of the extracellular proton release group. The first 13 amino acids of BR are removed in a posttranslational modification. BR residue numbering has been adjusted to reflect spectroscopic convention. (b) Structural alignment of Arch-1 (pdb 1UAZ) [19] with BR (pdb 1FBB) by jFATCAT. No structural adjustment was allowed. The RMSD between the structures was 1.07 Å. (c) Simplified version of the BR photocycle with absorption maxima of each state, adapted from [20].

The photocycle of Arch is likely similar to that of its close homologue bacteriorhodopsin (BR) (Fig. 2-1), which we take as a template. Light-induced

isomerization of retinal in BR induces a series of conformational shifts that moves one proton across the membrane. In the ground state (*g*) the retinal is in an all-*trans* conformation and the Schiff base is protonated. Absorption of a green or yellow photon induces photoisomerization to a 13-*cis* conformation (*g* → *L*), followed by proton transfer from the Schiff base to an acceptor on the extracellular side (*L* → M_1). The Schiff base then switches accessibility to the cytoplasmic side (M_1 → M_2), where a proton donor reprotonates the Schiff base (M_2 → *N*). The donor takes up a proton from the cytoplasm and the retinal thermally isomerizes back to all-*trans* (*N* → *O*). Finally, the acceptor releases its proton to the proton-release complex on the extracellular side (*O* → *g*). Figure 2-2 provides a visual summary of these proton movements.

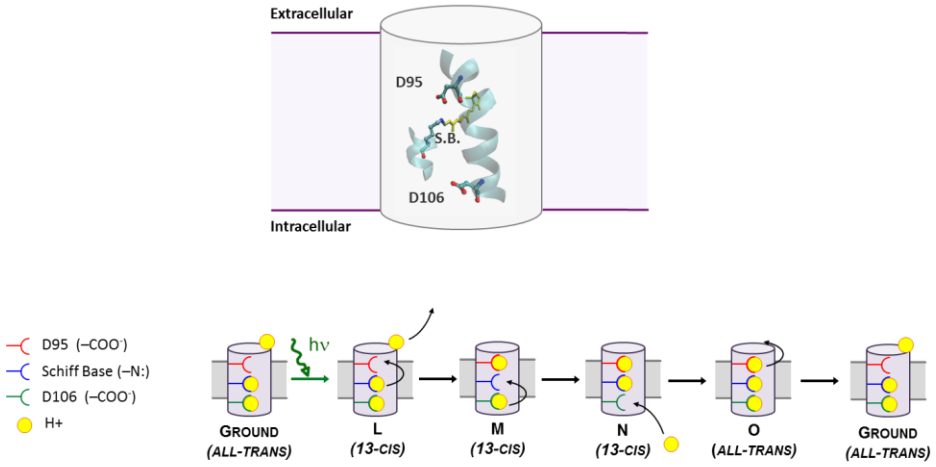

Figure 2-2. Proton movement in the photocycle of Arch-3. Simplified cartoon of one cycle of the Arch photocycle (omitting the short-lived K state and ignoring back-reactions and branches) showing how a proton moves from the cytoplasmic side to the extracellular side. In BR, D85 is the proton acceptor, and D96 is the proton donor. These residues correspond to D95 and D106, respectively, in Arch-3.

All photocycle intermediates except for *M* have overlapping absorption spectra peaked between 550 and 630 nm; due to the deprotonated Schiff base, the *M*

intermediates absorb maximally at 410 nm. While the photocycle was initially viewed as a series of sequential steps [21, 22], kinetic evidence suggests rapid equilibrium among the states within the 13-*cis* manifold [23, 24, 25]. Excitation of photocycle intermediates generates off-pathway states, some of which have been reported to be fluorescent [26, 27, 28, 29].

We previously speculated that voltage acted by modifying the protonation of the Schiff base in the ground state of Arch. Yet illumination at 230 W/cm^2, typical for imaging, corresponds to > 10^4 photon absorption events per molecule per second. Microbial rhodopsin photocycles typically last ~10 ms. Thus under photostationary imaging conditions, the population of the ground state is likely negligible. Each photocycle intermediate has a different charge distribution, and thus the relative energy of intermediates depends on membrane voltage. A realistic model must acknowledge that fluorescence and voltage sensitivity could arise anywhere in the photocycle.

Early transient absorption measurements on BR in vesicles indicated that hyperpolarizing voltage slowed the decay of an *M* state [30, 31, 32]. However, the membrane voltage was not precisely known in these experiments. Measurements of photocurrents in BR under patch-clamp conditions further indicated a voltage-dependent *M*-state decay [33, 34, 35]. *Acetabularia* rhodopsin behaved similarly, but a differing kinetic model led to the conclusion that voltage primarily acted to slow the *O*-state decay [36].

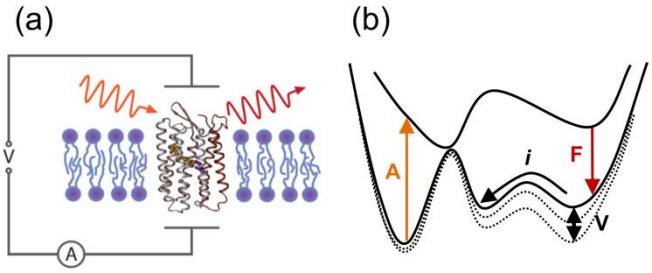

Figure 2-3. Multimodal spectroscopy of a microbial rhodopsin. (a) Optical and electrical perturbations induce fluorescence and photocurrent responses. Rhodopsins have strong cross-modality couplings (illumination modulating current; voltage modulating fluorescence) as well as nonlinear optical and electrical responses. (b) Dynamics on a potential energy landscape. Absorption (A), fluorescence (F), and photocurrent (i) probe distinct types of transitions, while voltage modulates the shape of the landscape.

Here we combine patch-clamp measurements with fluorescence spectroscopy of Arch and its photogenerated intermediates (Fig. 2-3). In section 2.2.1 we characterize the fluorescence, photocurrent, and voltage sensitivity spectra of Arch and the non-pumping mutant Arch(D95N) under steady state illumination. This information enables straightforward optimization of imaging parameters and is intended for readers wishing to perform voltage-imaging experiments. In section 2.2.2 we study the transient absorption and transient fluorescence of Arch to characterize the photocycle. In section 2.2.3 we combine optical with electrical measurements to probe cross-couplings between illumination and current; and between voltage and fluorescence. We conclude that fluorescence arises through a sequential three-photon process, and that membrane voltage tips the relative balance of an *M*-like and an *N*-like intermediate.

2.2 Results

2.2.1 Optimization of voltage-imaging

We sought to determine the illumination conditions (wavelength and intensity) most conducive to voltage imaging and least perturbative to membrane potential. The apparatus consisted of an inverted epifluorescence microscope equipped with multiple laser lines, combined with a patch-clamp electrophysiology rig. We expressed Arch in HEK293T cells and recorded fluorescence and photocurrent as a function of illumination wavelength, illumination intensity, and membrane voltage. All experiments were performed at 25 ºC unless otherwise indicated.

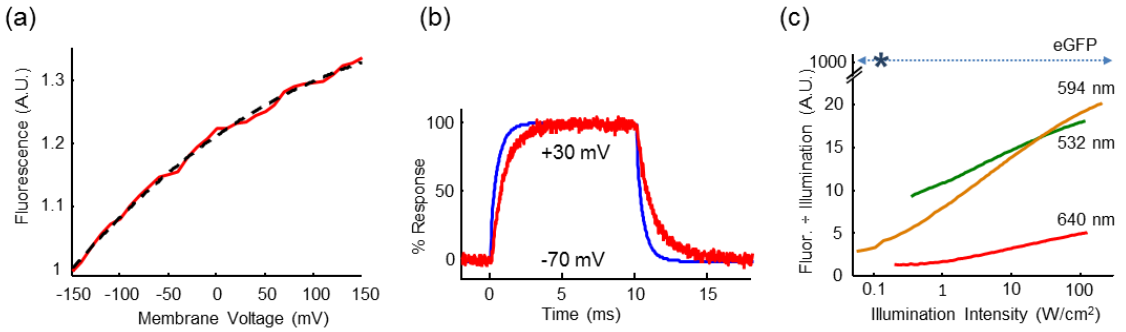

Figure 2-4. Arch as a voltage indicator. (a) Voltage-sensitive fluorescence of Arch (exc. 594 nm, 1000 W/cm^2, em. 660 – 760 nm). Dashed line is a fit to a two-state Boltzmann distribution. (b) Fluorescence response (red) to a voltage step from -70 mV to +30 mV (blue). The time constant of the voltage step arose from capacitive charging of the membrane. (c) Ratio of fluorescence to illumination intensity (F/I), as a function of illumination intensity. Under intense illumination, Arch is only 50-fold dimmer than eGFP.

Under steady-state high intensity illumination (1000 W/cm^2, 594 nm), Arch fluorescence increased by $\Delta F/F$ = 35% between -150 mV and +150 mV (Fig. 2-4a; under 640 nm illumination the sensitivity was $\Delta F/F$ = 100% for the same voltage range [7]). We used a photomultiplier to measure the fluorescence response to a step in applied voltage (Fig. 2-4b). The membrane voltage lagged the applied voltage by ~0.4 ms due to

the *RC* charging time of the membrane. After accounting for this lag analytically, we found that the protein step response had a time constant of 0.6 ms.

A puzzle in our initial experiments was the relative ease with which we imaged Arch in the microscope, compared to the reported extremely low fluorescence quantum yield (10^{-4} – 10^{-3}) of all known microbial rhodopsins [28, 37, 38]. The fluorescence of BR was reported to increase faster than linearly with increasing excitation intensity [39]. We thus measured Arch fluorescence, *F*, as a function of illumination intensity, *I*, (exc. 532 nm, 594 nm, or 640 nm; em. 660 – 760 nm) in a sample of fractionated *E. coli* membranes containing an Arch-eGFP fusion (Fig. 2-4c). Indeed, the relative brightness of Arch (*F*/*I*) increased at higher illumination intensity, growing 10-fold between 0.05 W/cm^2 and 200 W/cm^2 (exc. 594 nm). In contrast, eGFP showed *F*/*I* independent of illumination intensity (exc. 488 nm; em. 511 – 551 nm).

We previously reported that under dim illumination Arch was 500-fold dimmer than eGFP [7]. Our present results show that under intense illumination Arch is only 50-fold dimmer than eGFP. We measured the photocurrent as a function of illumination intensity and observed saturation behavior: under intense illumination, additional light did not lead to additional photocurrent (Fig. 2-5).

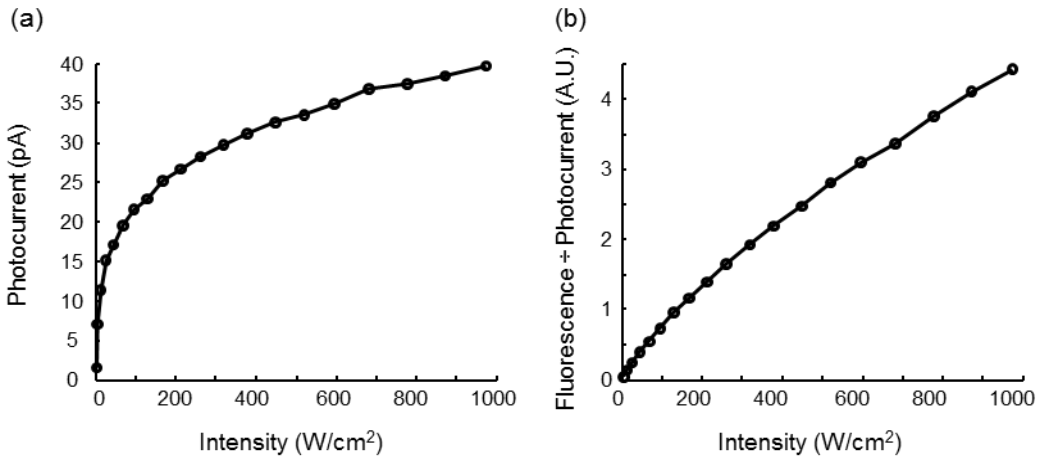

Figure 2-5. Saturation of Arch photocurrent at 594 nm. (a) Steady-state photocurrent in a HEK cell expressing Arch, as a function of illumination intensity at 594 nm. Membrane voltage was held at 0 mV by whole-cell patch clamp. The cell was alternately exposed to 50 ms of illumination and 50 ms of darkness. The plot shows the average difference in membrane current between these conditions. Each data point represents the average of 6 measurements. (b) Fluorescence per pA of photocurrent, recorded on the same cell as in (a). At higher illumination intensity, the fluorescence signal grew superlinearly, while the photocurrent saturated. Thus fluorescence measurements yield maximum signal relative to perturbation to membrane potential when the illumination was concentrated on a small piece of a cell. If fluorescence and photocurrent were both linear in illumination intensity, the graph in (b) would be a horizontal line.

We visually demonstrated the nonlinear increase in Arch fluorescence with increasing illumination intensity in a cuvette of purified Arch-eGFP fusion protein (Fig. 2-6). The cuvette was illuminated with focused CW illumination at 473 nm (2 μW, to excite eGFP) and 594 nm (5 μW, to excite Arch). While eGFP fluoresced throughout the beam path, Arch fluoresced predominantly at the focus. This nonlinear increase in Arch fluorescence occurred at an intensity ~10^{10}-fold lower than typically required for two-photon microscopy, implying a sequential multi-photon process in Arch, in contrast to the coherent multi-photon excitation commonly observed with pulsed femtosecond excitation.

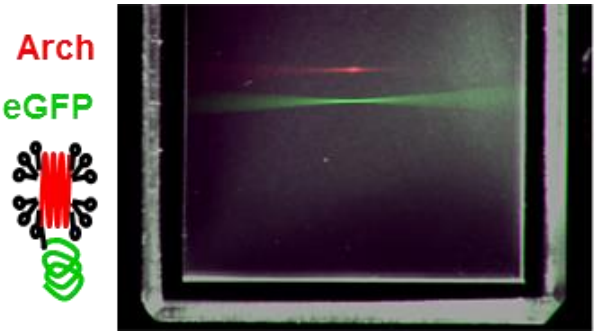

Figure 2-6. Visual demonstration of nonlinear dependence of Arch fluorescence on CW illumination intensity. Two laser beams were focused inside a cuvette containing an Arch-eGFP fusion. The top beam (594 nm) excited fluorescence from Arch. The identically shaped bottom beam (473 nm) excited fluorescence from eGFP. Arch fluorescence was localized to the focus while eGFP fluorescence occurred throughout the beam. Image is a pseudo-colored composite of three exposures taken under different camera settings.

We measured four key action spectra of Arch: photocurrent, ground-state absorbance, fluorescence excitation, and voltage sensitivity of fluorescence (see detailed methods in section 2.4.9). Due to the nonlinear dependence of Arch fluorescence on illumination intensity, we took care to maintain constant illumination intensity of 10 W/cm^2 across all wavelengths.

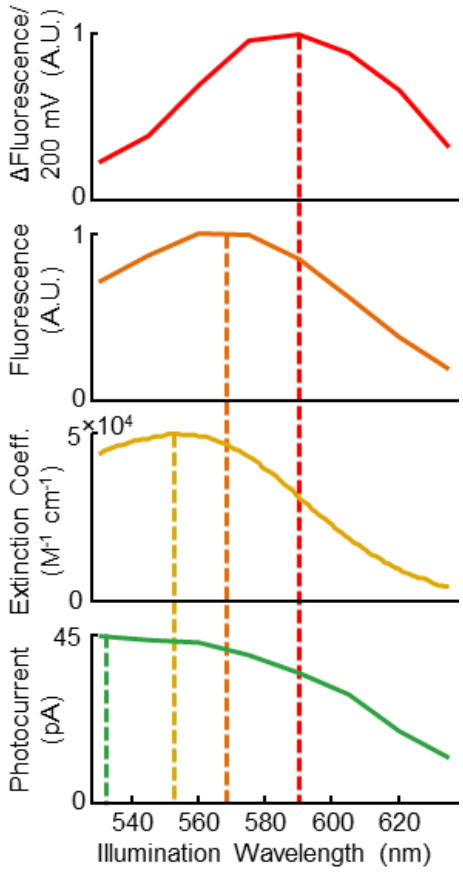

Figure 2-7. Action spectra of Arch. These spectra are distinct for different quantities (voltage sensitive fluorescence, fluorescence, absorption, and photocurrent).

Arch generated the largest photocurrent when excited at 530 nm (typically ~40 pA), absorbed maximally at 552 nm (extinction coefficient 50,300 $M^{-1}cm^{-1}$), showed maximal fluorescence (F) when excited at 570 nm and exhibited maximal change in fluorescence (ΔF) upon a voltage step when excited at 590 nm. Due to the differing spectra of F and ΔF, the peak in the fractional voltage sensitivity, $\Delta F/F$, occurred at a different wavelength (640 nm; Fig. 2-8a) than the peak in ΔF (590 nm; Fig. 2-7). These differing spectra further indicate that optical excitation of multiple states is involved in determining the photo-response of Arch.

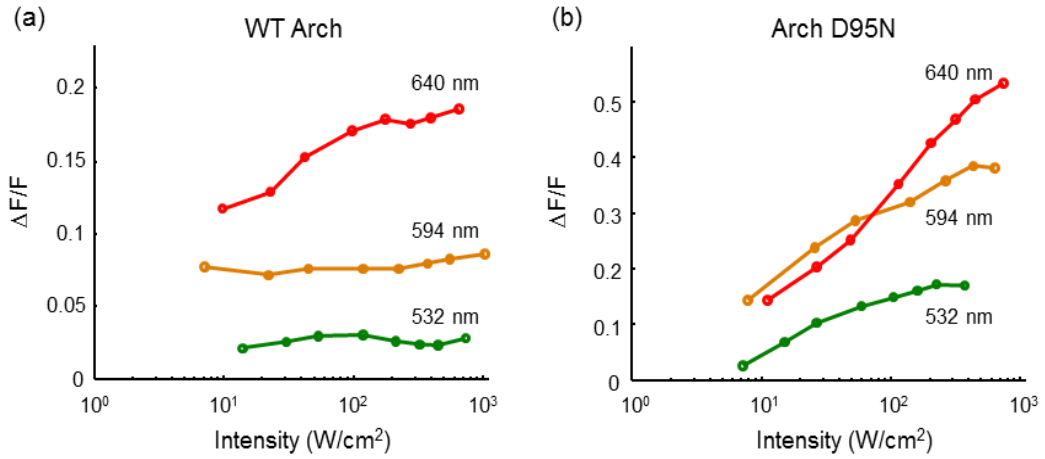

Figure 2-8. Voltage sensitivity vs. illumination intensity for Arch and Arch(D95N). (a) Voltage sensitivity (ΔF/F) of Arch WT increased nearly two-fold between 10 W/cm² and 650 W/cm² under illumination at 640 nm, while voltage sensitivity was independent of illumination intensity under illumination at 532 nm and 594 nm. Note that the parameter plotted here, ΔF/F, is different from the absolute change in fluorescence, ΔF, which is plotted in Figure 2e. (b) In contrast, the voltage sensitivity of Arch D95N increased markedly with illumination intensity at all three wavelengths. Sensitivity increased 5x between 10 W/cm² and 700 W/cm² at 640 nm. These results imply that fluorescence of Arch WT is dominated by a single fluorescent species, with possibly a weak contribution from a red-shifted voltage-insensitive state. Fluorescence of Arch(D95N) appears to have contributions from voltage sensitive and insensitive states, with the photostationary equilibrium shifting toward the voltage sensitive state(s) at higher illumination intensity.
HEK cells expressing Arch WT or Arch(D95N) were subjected to whole-cell voltage clamp and exposed to illumination of specified wavelength and intensity. Fluorescence was recorded on an EMCCD. At each wavelength, intensity was increased in steps (1.6 seconds per step) from 0 to ~800 W/cm². At each intensity, membrane voltage was stepped between -70 mV and +30 mV four times at a frequency of 2.5 Hz. The entire waveform was repeated 2x per cell to ensure stability of the system. ΔF/F was calculated as the change in fluorescence over 100 mV (between -70 mV and +30 mV) divided by the fluorescence at -70 mV of the 150 most responsive pixels (as determined using the weighting algorithm outlined by Kralj *et al.* [7]). In (a) and (b) data is averaged over $n = 2$ cells.

These findings inform the choice of optics used to image Arch. To maximize voltage sensitivity and to minimize photocurrent, the illumination should be red or orange. While green illumination produces comparatively strong fluorescence, this fluorescence is not sensitive to voltage. With conventional fluorophores one can trade exposure time for illumination intensity to maintain a constant signal. Due to the multi-

photon excitation of Arch, this tradeoff is not possible. Illumination with an LED or arc lamp produces barely detectable fluorescence, while intense illumination (typically from a laser) leads to a robust signal.

We previously introduced the mutant Arch(D95N) as a non-pumping voltage reporter. We characterized Arch(D95N) just as we had characterized the WT protein (Fig. 2-9). This mutant had a slower response time than wild-type Arch, with a minor (~20%) component occurring in < 1 ms, and a major (~80%) component lasting 36 ms rising, 30 ms falling at 25 ºC. Remarkably, at 35 ºC the fast component grew significantly, accounting for ~55% of the response. These results will be useful to researchers interested in using Arch(D95N) as a voltage indicator. The fractional voltage sensitivity of wild-type Arch, $\Delta F/F$, was relatively insensitive to illumination intensity between 10 – 1000 W/cm^2, while for Arch(D95N) $\Delta F/F$ increased 3 to 5-fold over this range, depending on the excitation wavelength (Fig. 2-8b).

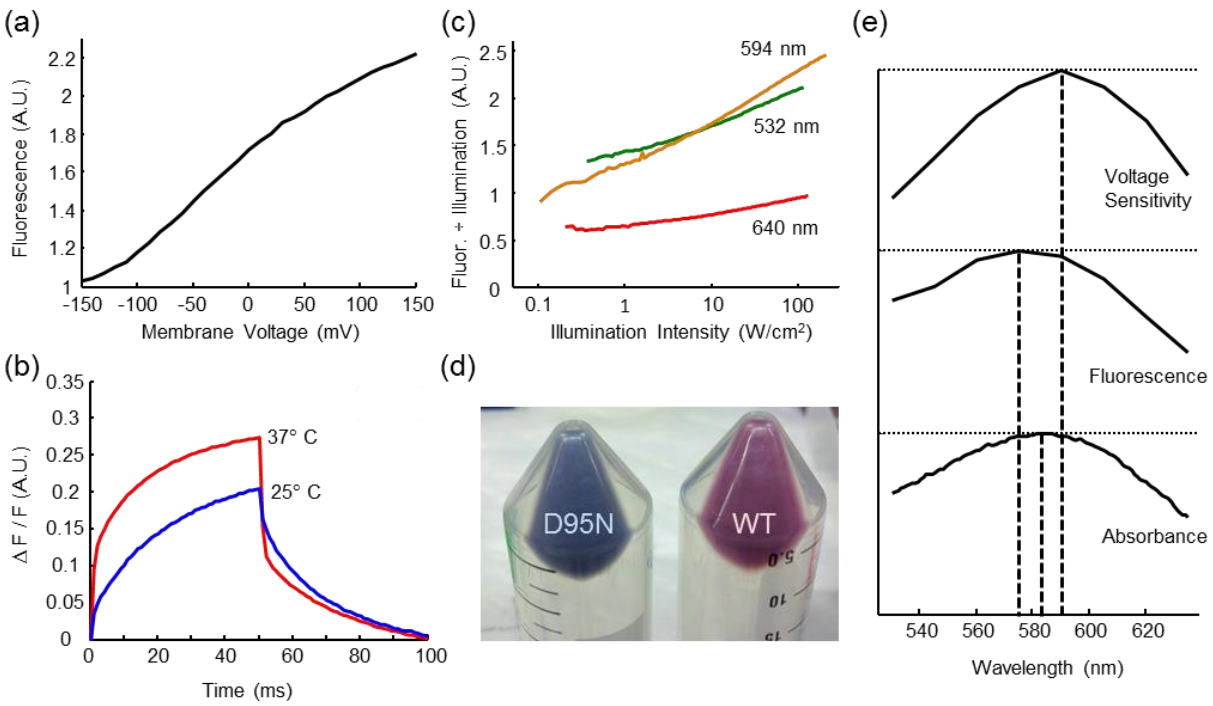

Figure 2-9. Characterizing Arch(D95N). (a) Voltage-sensitive fluorescence of Arch(D95N) (exc. 594 nm, 1000 W/cm², em. 660 – 760 nm) in HEK cells at 25 °C. Membrane voltage was controlled via whole-cell patch clamp. Fluorescence was recorded on an EMCCD camera. (b) Fluorescence response to a voltage step between -80 mV and +20 mV at two temperatures. (c) Ratio of fluorescence to illumination intensity (F/I), as a function of illumination intensity, showing the nonlinear response of Arch(D95N) fluorescence. (d) Picture of *E. coli* expressing Arch(D95N) (left, blue) and Arch (right, purple), demonstrating the difference in ground-state absorption spectra of these two species. (e) Action spectra for Arch(D95N) (analogous to those obtained for WT Arch in Figure 2(e)). Arch(D95N) did not generate a detectable photocurrent.

2.2.2 Photocycle of Arch

Transient absorption spectra of detergent-solubilized Arch were recorded with excitation by a nanosecond pulsed Nd:YAG laser at 532 nm (Fig. 3a, b). These spectra closely matched corresponding spectra of Archaerhodopsin 1 [40] and BR [41]. The pH-dependent transient absorption (Fig. 4c, below) suggested a slowing of *M* formation at pH 6, consistent with proton release preceding M formation. Formation of *O* was slower at pH 8, indicating that proton uptake preceded *O* formation.

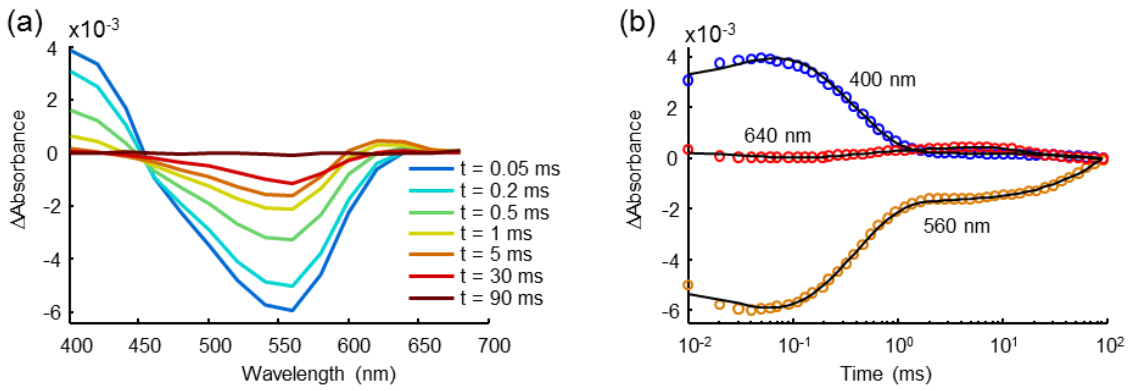

Figure 2-10. Time-resolved absorption spectroscopy of Arch. (a) Transient absorption spectra showing early rise of a blue-shifted *M* intermediate, and late rise of a red-shifted *O* intermediate. (b) Time-dependent absorption data are well described by a fit to four exponential decays.

As with BR, Arch showed dark adaptation. When left in the dark for several minutes Arch spontaneously converted into a state with increased initial fluorescence upon onset of illumination (Fig. 2-11). In BR, dark adaptation corresponds to conversion from all-*trans* retinal to a mixture of all-*trans* and 13-*cis* retinal [42].

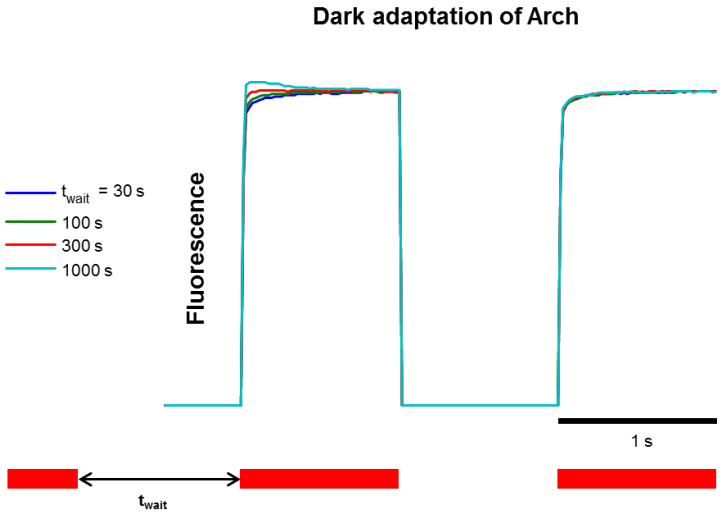

Figure 2-11. Dark adaptation of Arch. Arch was expressed in *E. coli* as described previously and illuminated with two pulses of red light (637 nm, 200 W/cm^2) as shown. The sample was then left in the dark for some duration t_{wait} and the sequence was repeated. The initial fluorescence during the first pulse depended on the time (t_{wait}) since the previous pulse, demonstrating that Arch underwent a very slow (~ 5 minutes) change in the dark.

The ambiguities in inferring a kinetic model from transient absorption alone have been well documented [41, 43]. Based on the strong sequence and spectroscopic homology between Arch and BR we assumed a BR-like photocycle and used the transient absorption data to infer rate constants. Fig. 2-10b shows the fit of this model to some of the transient absorption data. This model indicates that a blue-absorbing *M* state formed within 50 μs and decayed with a time constant of 390 μs. A red-absorbing *O* state arose with two time constants of 390 μs and 4.1 ms, and decayed with a time constant of 14 ms. The *N* state is not directly visible in the transient absorption due to its strong spectral overlap with the ground state.

To determine which intermediate state (or states) produced fluorescence we performed transient fluorescence experiments on fractionated *E. coli* membranes containing Arch. An intense green pump pulse (50 W/cm^2, 100 μs, 532 nm) initiated the photocycle. A weak red probe pulse (15 W/cm^2, 100 μs, 640 nm) excited fluorescence with variable delay after the pump.

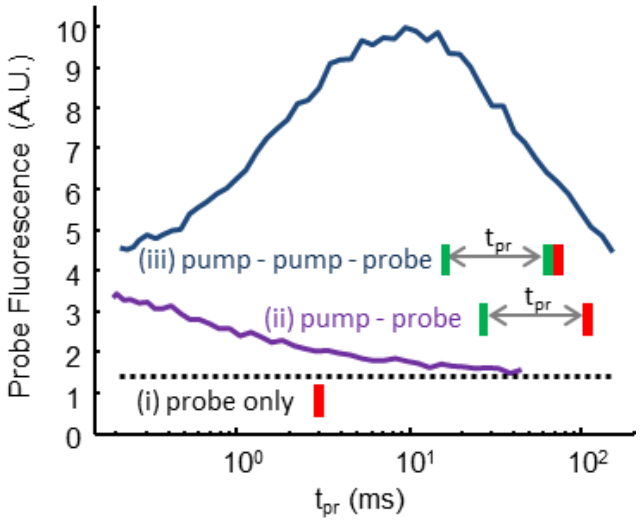

Figure 2-12. Time-resolved fluorescence spectroscopy of Arch. Transient fluorescence experiments established that fluorescence was dominated by a sequential three-photon process.

Illumination with the probe alone produced barely detectable fluorescence (Fig. 2-12c(i)), consistent with the expected low fluorescence quantum yield of the Arch ground state. Application of a single pump pulse before the probe produced a species more than twice as fluorescent as the ground state. This species appeared in < 20 μs and decayed with a time constant of 1.0 ms (Fig. 2-12c(ii)). Remarkably, application of two pump pulses before the probe (timing shown in Fig. 2-12c(iii)) produced up to 6-fold more fluorescence than the ground state. Fluorescence peaked with an interval of 10 ms between the pump pulses (Fig. 2-12c(iii)). These experiments established that the fluorescence of Arch arises from a sequential three-photon process: one photon to initiate the photocycle, a second to generate the fluorescent species from a photointermediate, and a third photon to induce fluorescence.

We characterized the action spectra and saturation properties of each of the three photons (Figs. 2-13, 2-14, and 2-15).

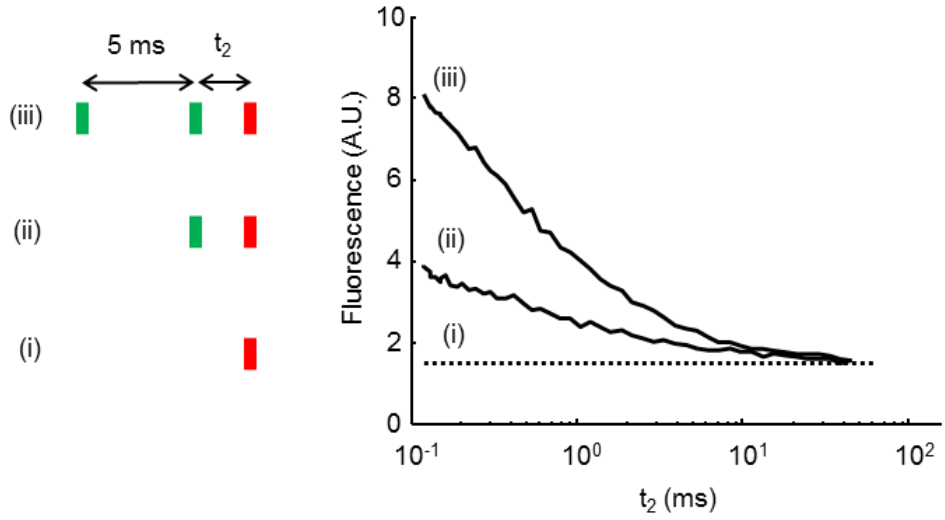

Figure 2-13. Nonlinear fluorescence properties of Arch. Decay of the fluorescent *Q* state. Fluorescence was recorded as a function of the delay between the last pump pulse and the probe. Illumination and recording conditions were as in Fig. 2-12. Curve (i) shows the low fluorescence of the ground state. Curve (ii) shows that a single pump pulse created a small fluorescent population which decayed in 1.0 ms. Curve (iii) shows the decay of the fluorescent *Q* state created by two sequential pump pulses 5 ms apart. The *Q* state decayed in 0.84 ms. The similar decay rates in curves (ii) and (iii) led us to conjecture that they reflect the same state, i.e. that there exists a small population in the pre-fluorescent *N* state in Arch in the dark.

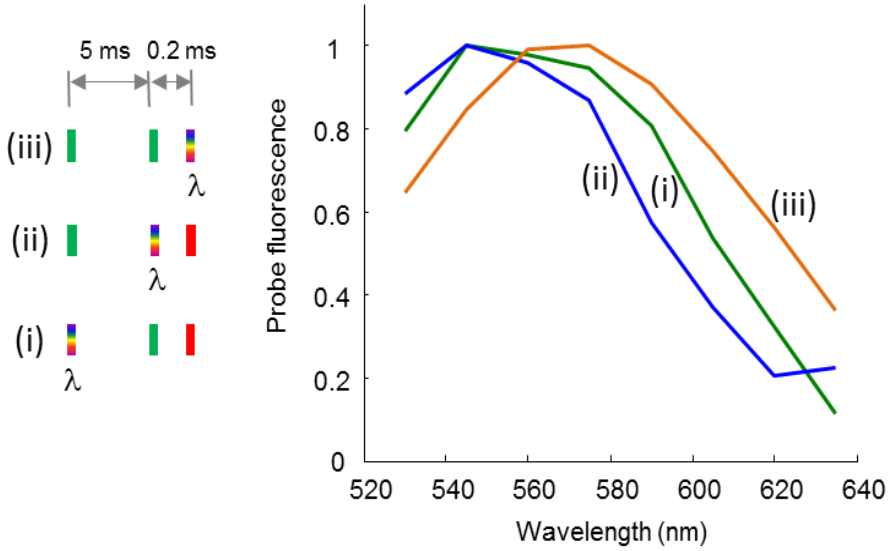

Figure 2-14. Action spectra of each photon-mediated transition. We determined the spectrum of each photon-mediated transition by varying the wavelengths of each illumination pulse while keeping the other pulses fixed. The initial fluorescence elicited by the final pulse is plotted as a function of the wavelength of either the first (i), second (ii), or third (iii) photon.
Illumination and recording conditions were as in Fig. 2-12. The variable-wavelength pulses were at an intensity of 0.7 W/cm2 and were obtained from the supercontinuum laser. The fixed-wavelength pulses were at 532 nm, 50 W/cm2 for pumps 1 and 2, and 640 nm, 15 W/cm2 for the probe pulse. All pulses were 100 μs long. Fluorescence was determined from the first 20 μs of the probe pulse to ensure that the probe did not perturb the state of the protein. We verified that fluorescence was linear in the probe intensity.

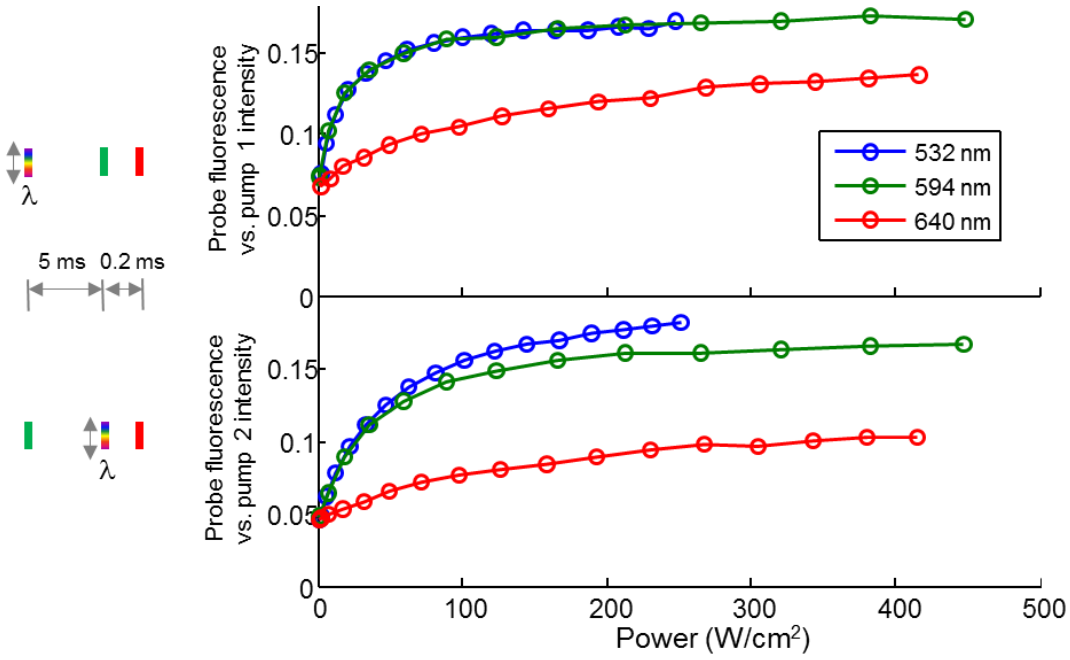

Figure 2-15. Saturation of the first two photon-mediated transitions. We varied the intensity of pumps 1 and 2 to measure the saturation of these optically driven transitions. In all cases the pumps were 100 μs long and the fixed-intensity pump was at 532 nm, 50 W/cm^2. When the pump wavelength was 640 nm, the saturation value of the fluorescence was lower than when the pump wavelength was 594 nm or 532 nm. This was true for both the first and second pumps. These results suggest a possible back-reaction or non-pumping shortcut in the photocycle with a red-shifted action spectrum. We did not detect saturation of the third pulse (the pulse responsible for exciting fluorescence). Due to the extremely short excited state lifetime of Q (~62 ps in BR), this state is expected to saturate at experimentally inaccessible intensities.

Photon 1 matched the ground state absorption spectrum of Arch. Photon 2 was blue-shifted by 10 nm relative to photon 1. In BR, the *N* state has a 10 nm blue-shift relative to the ground state, so we provisionally assign photon 2 to excitation of an *N*-like intermediate. Photon 3 peaked at 570 nm. At low intensities of pumps 1 and 2, the fluorescence from pump 3 was linear in all three pump intensities, confirming that each contributed a single photon. We also measured the spontaneous decay (presumably back to *N*) of the fluorescent state, and found a time constant of 0.84 ms. We combined

the transient absorption and fluorescence data to propose a photocycle shown in Figure 2-16.

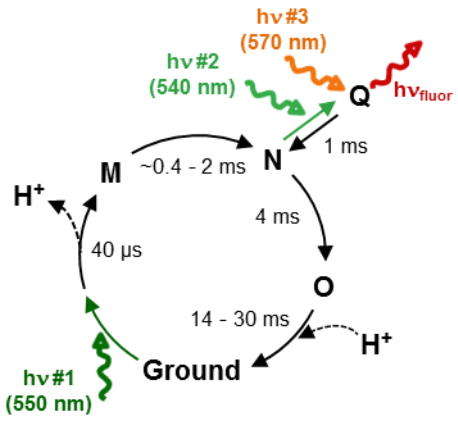

Figure 2-16. Proposed photocycle. Rates are derived from transient absorption and transient fluorescence data in Figs. 2-10 and 2-12

Ohtani and coworkers found that in BR sequential absorption of two photons generated a state, termed *Q*, which could be excited by a third photon to yield fluorescence[1] [28, 39, 44]. This state had an excited state lifetime of 62 ps, vs. ~500 fs for the ground state, and was thus ~100-fold more fluorescent than the ground state [44]. The *Q* state was excited by red light, and emitted in the near infrared with a peak at ~720 nm. The timing in the photocycle, excitation and emission spectra, and thermal relaxation rate of our fluorescent state match the Ohtani *Q* state, so we designate the dominant fluorescent state *Q*.

[1] The term *"Q"* state has been used to represent other intermediates in the BR photocycle [26]. Here we refer exclusively to the Ohtani *Q*.

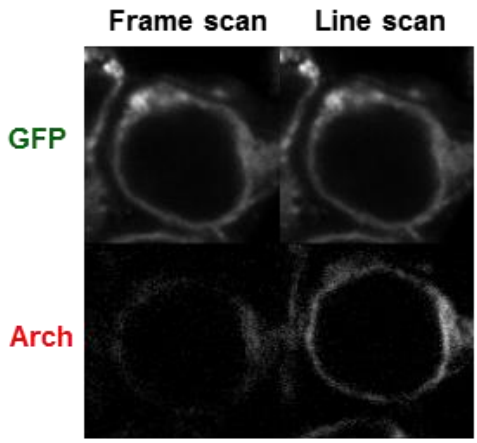

Figure 2-17. Confocal scans showing the effects of scan speed on brightness. Arch fluorescence was sensitive to the timing of the illumination, while eGFP fluorescence was not.

The complex photophysics of Arch fluorescence have important implications for its use as a fluorescent label in confocal microscopy. During a frame-scanning confocal measurement, each molecule experiences microsecond bursts of intense illumination, spaced by hundreds of milliseconds of darkness. These bursts are shorter than the time required for Arch to enter the fluorescent *Q* state, and the inter-burst interval is longer than the photocycle. Thus under frame-scanning conditions, Arch appeared very dim (Fig. 2-17). In line-scanning mode, each line of the image was scanned multiple times before the laser advanced to the next line. The interval between line scans (~0.5 ms) was shorter than the photocycle, so the illumination in each scan sensitized fluorescence in subsequent scans. Arch then appeared brighter. In an Arch-eGFP fusion, the brightness of eGFP was independent of the scan mode.

2.2.3 Optoelectronic properties of Arch

To identify states whose population depended on voltage, we transiently expressed Arch in HEK293T cells, and recorded membrane current $i(t)$ and fluorescence $F(t)$ as functions of the membrane voltage $V_m(t)$ and illumination $I(\lambda,t)$. Three attributes of voltage-sensitive fluorescence were immediately striking:

(1) A step in illumination (from darkness) under constant voltage induced fluorescence that was initially *not* sensitive to membrane voltage (Fig. 2-18a). Fluorescence became sensitive to voltage with a time constant of 2 ms.

(2) A step in voltage under constant illumination induced a fluorescence response with a time constant of 0.6 ms (Fig. 2-4a).

(3) An initial flash of light sensitized the protein so that fluorescence from a second flash was a) brighter than fluorescence from an isolated flash, and b) sensitive to voltage (Fig. 2-18b). Both forms of sensitization arose with a time constant of 2 ms, and fell with a time constant of 30 ms.

Observation (1) rules out a voltage-dependent change in the ground state as the origin of voltage-dependent fluorescence, in contrast to our previously proposed model [7]. Observation (2) requires that the voltage-sensitive step be fast, and either involve the fluorescent state directly, or be coupled to the fluorescent state by fast rate constants. Observation (3) establishes that the voltage-sensitive manifold is long

lasting. Thus the fast voltage-sensitive rate is preceded by a somewhat slower step and is followed by a much slower step in the photocycle.

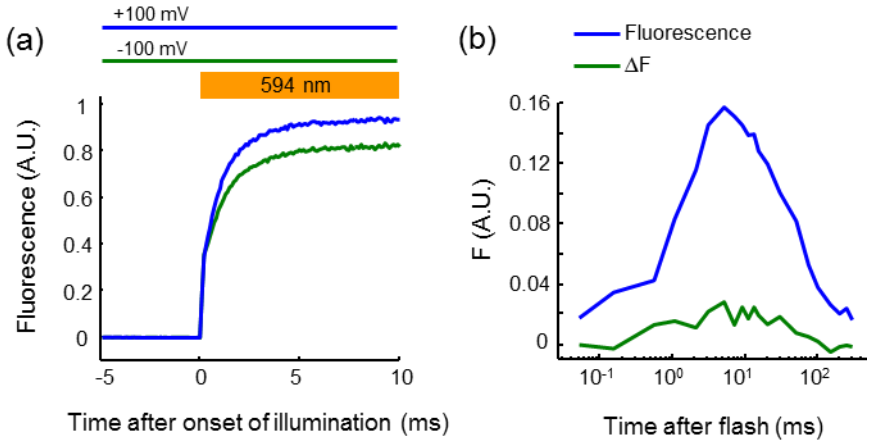

Figure 2-18. Exploring voltage-dependent fluorescence in Arch. (a) Fluorescence response of Arch to a step in illumination at V_m = +100 mV and -100 mV. (b) Transient responses of Arch in a double-flash experiment. Fluorescence from the second flash rose and fell following initiation of the photocycle. The difference in fluorescence between +30 mV and -70 mV, ΔF, rose and fell with the fluorescence.

One other measurement pointed to a long-lived voltage-sensitive intermediate. In a double-flash experiment, the photocurrent from the second flash was smaller than from the first, recovering with a time constant of 32 ms (a two-exponential fit yielded time constants of 3.8 and 54 ms; Fig. 2-19). The photocurrent recovery reflects ground state repopulation, and thus indicates a long-lived intermediate.

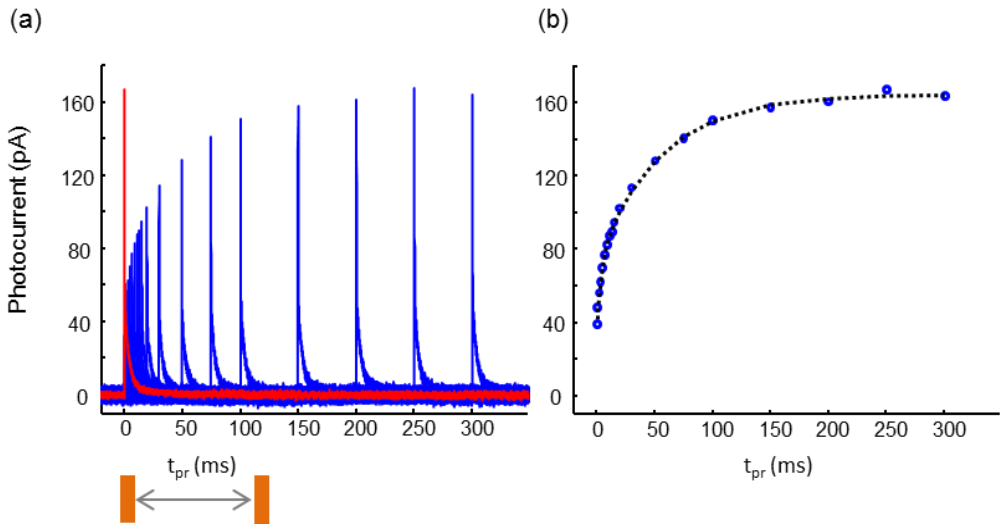

Figure 2-19. Ground state recovery measured by photocurrent in HEK cells. We measured the time-course of ground state recovery in HEK cells by monitoring the photocurrent recovery in a two-pulse experiment. (a) Current due to the first illumination pulse (red). Additional current due to each probe pulse (blue). (b) Peak photocurrents from the second pulse (blue circles). Fit to a double exponential (black dotted line) with time constants of 3.8 ms (weighting coefficient = 1) and 54 ms (weighting coefficient = 3). When photocurrent recovery was fit to a single exponential, the time constant was 32 ms.

The local access model of the BR photocycle proposes that all 13-*cis* photointermediates — *L*, M_1, M_2, and *N* —are in rapid equilibrium [24]. Fluorescence arises from a branch off *N*, so we hypothesized that voltage acted within the 13-*cis* manifold. We further hypothesized that voltage acted by modulating the protonation of a fluorescence-determining functional group within the 13-*cis* manifold. Thus a state whose population showed pH sensitivity near neutral pH would be a plausible voltage-sensitive state. We performed transient absorption spectroscopy on detergent-solubilized Arch as a function of pH. At pH 8, a long-lived *M* state appeared (Fig. 2-20).

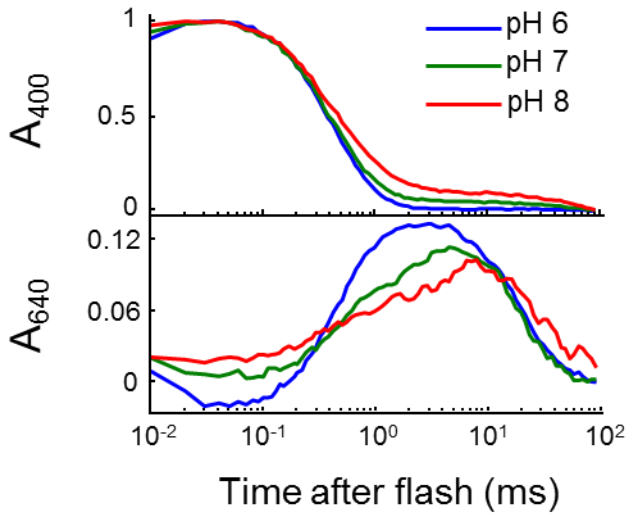

Figure 2-20. pH-dependent transient absorption. Transient absorption in solubilized Arch as a function of pH, normalized to the maximum signal at 400 nm.

Based on the pH-dependent transient absorption (Fig. 2-20), and the extensive literature suggesting a voltage-dependent *M* decay in BR, we tested whether membrane voltage tuned an *M* ⇌ *N* equilibrium in Arch. This hypothesis was attractive because a) an *M* state would not be excited by the red or orange laser, and thus could be a dark equilibrium partner with the pre-fluorescent *N* state; and b) in the *M* → *N* transition, the Schiff base is reprotonated from the proton donor (D106), which resides between the Schiff base and the cytoplasm. The long range (10.5 Å in BR) and orientation of this proton-transfer would favor the non-fluorescent *M* state at negative voltage and the pre-fluorescent *N* state at positive voltage, consistent with the observed dependence of fluorescence on voltage.

To test this hypothesis we used flashes of violet light (407 nm) to depopulate the *M* state under photostationary red light illumination. Violet light is known to induce 13-*cis* to *all-trans* isomerization in the *M* state, short-circuiting the photocycle from *M* to

ground. Similar illumination protocols have been used in BR [33, 34] and in *Acetablularia* rhodopsin [36]. We recorded the photocurrent and fluorescence under red and (red + violet) illumination, as a function of membrane voltage.

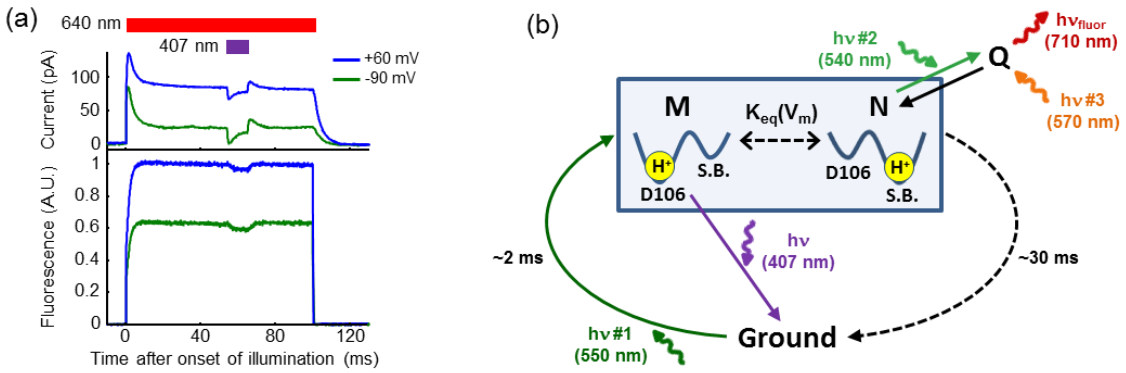

Figure 2-21. Probing a voltage-dependent *M* ⇌ *N* equilibrium. (a) Photocurrent and fluorescence in response to illumination with a pulse of red light, with a superimposed pulse of violet light. (b) A simplified model of voltage sensitivity and fluorescence in Arch. Photon #1 initiates the photocycle. Voltage modulates a proton-transfer equilibrium between two photocycle intermediates: an *M* state with a protonated donor (D106) and an *N* state with a protonated Schiff base (S.B.). Fluorescence arises through conversion of *N* to *Q* (photon #2) followed by electronic excitation of *Q* (photon #3).

Under photostationary red illumination, addition of violet light decreased the photocurrent and the fluorescence, indicating the presence of an *M*-state population (Fig. 2-21a). To test whether this data was consistent with a voltage-dependent *M* ⇌ *N* equilibrium, we constructed a highly simplified model of the photocycle shown in Fig. 2-21b. The *M* ⇌ *N* interconversion was assumed to be fast compared to the other rates, and thus always at equilibrium. Red illumination delivered population into the 13-*cis* manifold, while molecules relaxed back to ground at a rate proportional to the N population. Violet illumination introduced an additional relaxation pathway, with a rate proportional to the M population.

This model quantitatively reproduced a) the shapes of the photocurrent and fluorescence transients upon onset of red illumination; b) the dependence of steady-state fluorescence and photocurrent on membrane voltage under red illumination only; and c) the effect of violet illumination on fluorescence and photocurrent (Fig. 2-22). We thus conclude that a voltage-dependent $M \rightleftharpoons N$ equilibrium is a likely explanation for voltage-dependent fluorescence in Arch.

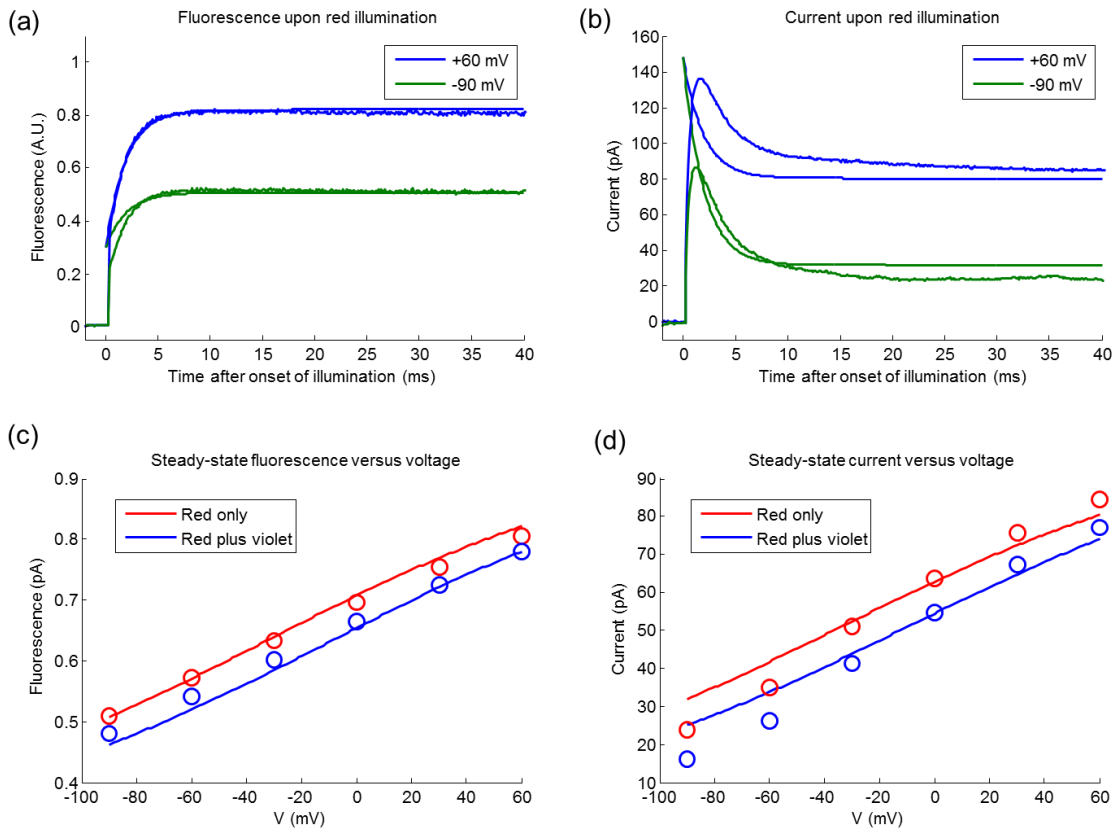

Figure 2-22. Fits to the photocycle in Figure 2-21b. We modeled the photocycle of Figure 2-21b quantitatively (see section 2.4.16, "Model of voltage-dependent fluorescence in Arch"). We reproduced the main features of the data shown in Figure 2-21a. Panels (a) and (b) show the response of fluorescence and current to the onset of red illumination at -90 mV and +60 mV (see "Time- and voltage-dependent fluorescence in HEK cells" in Methods for experimental details). Fits are shown. The model reproduced the shapes of the transients in both fluorescence and current upon illumination onset. Panels (c) and (d) show steady-state fluorescence and current as a function of membrane voltage under constant 640 nm illumination and under 640 nm + 407 nm illumination. The voltage-dependence of both fluorescence and photocurrent, as well as the decreases in fluorescence and current caused by 407 nm illumination, were recapitulated by our model.

Due to the small number of states, the model could not reproduce the complex kinetics of ground-state recovery. This model does not rule out more complex mechanisms of voltage sensitivity, such as voltage-dependent equilibria among L, M_1, and M_2, or multiple voltage-dependent rates. Our data do not distinguish between these scenarios.

2.3 Discussion

The ground state of Arch is only weakly fluorescent, but a photogenerated intermediate is roughly 10-fold brighter than previously thought. Fluorescence arises through sequential action of three photons. Voltage sensitivity is a property of a 13-*cis* photocycle intermediate, not the ground state, and likely arises through protonation of the Schiff base from the cytoplasmic side (i.e. a voltage-dependent M ⇌ N equilibrium).

A possible strategy for increasing the voltage sensitivity and brightness of Arch is to generate a protein with a 13-*cis* ground state or a metastable 13-*cis* intermediate. For instance, the D96N and D96N/D115N mutations of BR are known to prolong the lifetime in the 13-*cis* manifold [45], so homologous mutations in Arch (D106N, D125N) may enable voltage imaging under lower illumination intensities.

We further propose that mutations on the extracellular side designed to block current (such as D95N in Arch) are more likely to preserve voltage sensitivity than are mutations on the cytoplasmic side. The fluorescent *Q* state is reached by photoexcitation of the 13-*cis N* state. Thus *Q* is unlikely to be exclusively 13-*cis*, but its isomerization state is not known. A structural model of *Q* would facilitate efforts to engineer proteins with improved brightness.

The differing spectra of F and ΔF (Fig. 2-7), and the presence of fluorescence immediately upon illumination (Fig. 2-12, 2-18a) indicate that the photocycle may contain two (or more) fluorescent species, not all of which are voltage sensitive. Our study has focused on the dominant voltage-sensitive species. The other fluorescent

state(s) await characterization. Furthermore, under simultaneous illumination at two wavelengths within the visible (530 – 640 nm) the fluorescence and photocurrent depended in a complex way on the wavelengths and relative intensities of the illumination (Fig. 2-23). These effects likely arise from additional light-driven pathways not included in our simple models.

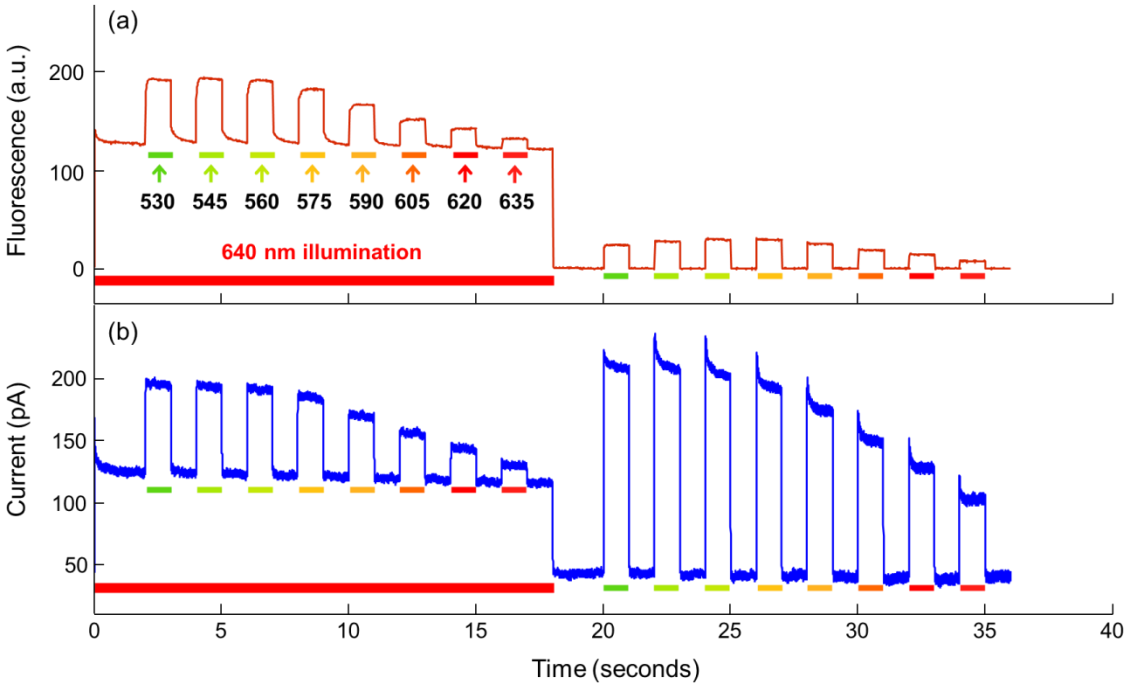

Figure 2-23. Effect of intense red illumination on fluorescence and photocurrent action spectra. A HEK cell expressing WT Arch was held at 0 mV under voltage clamp. (a) Fluorescence excitation spectrum and (b) photocurrent action spectrum of Arch under dim illumination (10 W/cm^2) in the presence (t = 0 to 18 s) or absence (t = 18 to 36 s) of intense red illumination (~1000 W/cm^2, 640 nm). Addition of intense red light caused slow (~200 ms) transients in fluorescence to appear, while causing the disappearance of slow (~300 ms) transients in photocurrent. Additionally, at wavelengths between 530 and 575 nm, addition of intense red light decreased the total photocurrent. This observation suggests a red light-dependent back-reaction or shortcut in the photocycle. The traces shown are an average of 3 cycles repeated on the same cell. The presence of slow dynamics in the fluorescence (640 nm on) in the absence of slow dynamics in the photocurrent; and slow dynamics in the photocurrent (640 nm off) in the absence of slow dynamics in the fluorescence, suggest that Arch contains transitions that are either spectrally or electrically silent. The presence of such transitions presents a severe challenge for efforts to elucidate the photocycle, and highlights the importance of multimodal spectroscopic and electrical measurements.

The rich spectroscopic and optoelectronic properties of microbial rhodopsins have previously been considered for application in optical information processing and data storage [46]. While such applications have not yet been widely adopted, the ability of rhodopsins to transduce light into changes in membrane voltage have enabled many new optogenetic tools. We propose that optoelectronic coupling in the opposite direction—changes in membrane voltage affecting optical properties—will enable a similarly broad set of applications in bio-imaging.

2.4 Materials and Methods

2.4.1 Microscope system

All single-cell data were acquired on a homebuilt microscope, illustrated in Figure 2-24.

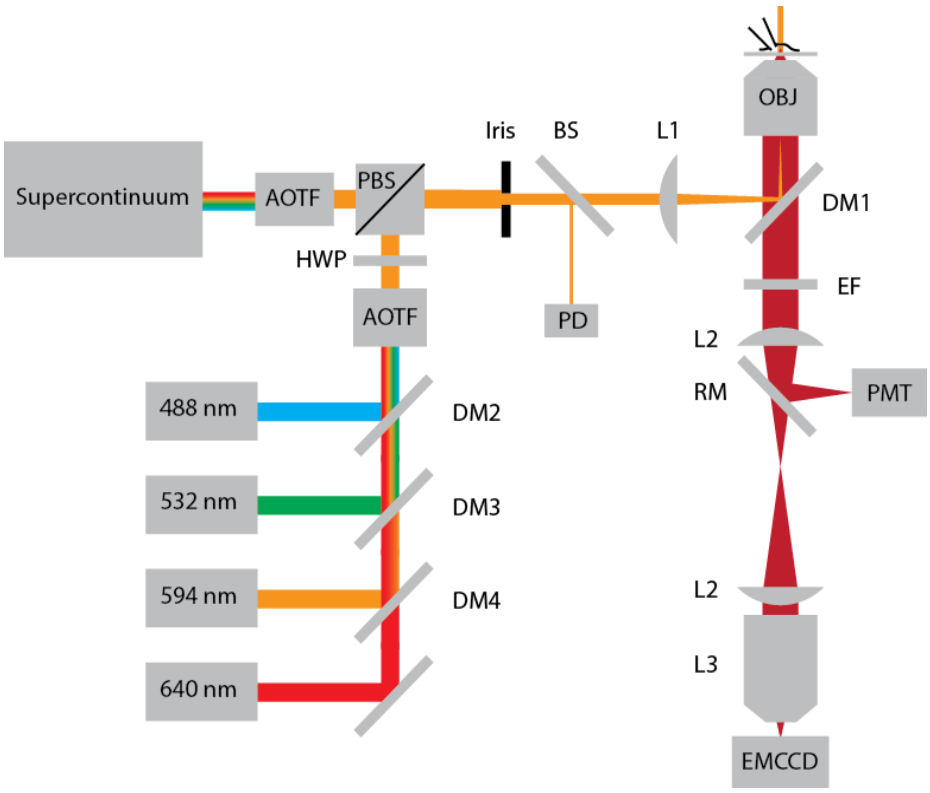

Figure 2-24. Schematic diagram of home-built microscope. AOTF: acousto-optic tunable filter. EMCCD: elctron-multiplying charged-coupled device camera. PMT: photmultiplier tube. OBJ: Objective lens. EF: emission filter. DM(1-4): dichroic mirror. PBS: polarizing beam splitter. HWP: half-wave plate. PD: photodiode. BD: beam splitter. L1, L2 achromatic lenses. L3: photographic lens. RM: removeable mirror.

Beams from four CW lasers (637 nm 100 mW Coherent OBIS; 594 nm 100 mW Cobolt Mambo; 532 nm 50 mW Coherent Compass 215M; 488 nm 50 mW Omicron PhoxX) were combined using dichroic mirrors and then spectrally selected using an acousto-optic tunable filter (AOTF; Gooch and Housego 48058). White light emission from a supercontinuum laser (Fianium SC-450-6) was spectrally selected using a second AOTF (Crystal Technologies). The polarization of the CW laser outputs was rotated 90º using an achromatic half wave plate (Thorlabs AQWP05M-600), and then combined with

the CW laser outputs using a polarizing beam splitter. The intensity at each wavelength was controlled with 10 μs time resolution.

Illumination was focused onto the back focal plane of the objective (Olympus, 1-U2B616 60× oil, NA 1.45) via a 650 nm long-pass dichroic mirror. The sample was illuminated in epifluorescence mode and emission was collected by the same objective and passed through the dichroic mirror. Fluorescence was filtered with a 660 – 760 nm bandpass filter (Semrock) and collected on either a photomultiplier tube (PMT; Thorlabs PMM02 with multialkali (S20) photocathode) or a cooled EMCCD camera (Andor iXon X3 860, 128 x 128 pixels). The output of the photomultiplier tube was filtered at 50 kHz using an 8-pole Bessel filter (Alligator Technologies USBPGF-S1) and recorded at 100 kS/s on a National Instruments DAQ (PCIe-6323). The DAQ also produced control waveforms for the AOTF and patch-clamp amplifier, and recorded the patch-clamp current signals.

We measured laser intensities during experiments by splitting off a small fraction of the lasers onto a photodiode (Thorlabs DET36A) using a glass slide. We accounted for the spectral response of the photodiode by calibrating against a well-calibrated power meter (Coherent FieldMax II). Due to the nonlinear intensity dependence of Arch photophysics, it was essential to ensure uniform illumination across the sample. To achieve this we expanded the Gaussian laser beams and selected a small region in the middle using an iris in an image plane to make a sharp disk of even illumination on our sample. We confirmed using a uniform sample of fluorescent beads (Invitrogen) that the intensity did not vary by more than 10% from its mean value within this disk.

Data acquisition was controlled using custom software written in LabView (National Instruments).

2.4.2 Electrophysiology

Patch clamp experiments were performed at room temperature (25 °C) using an Axopatch 200B amplifier (Molecular Devices). Micropipettes were pulled from borosilicate glass capillary tubes (World Precision Instruments, 1.5 mm OD, 0.84 mm ID) using a dual-stage glass micropipette puller (Narishige, PC-10) to a tip resistance of 5-10 MΩ and filled with intracellular buffer (125 mM potassium gluconate, 8 mM NaCl, 0.6 mM $MgCl_2$, 0.1 mM $CaCl_2$, 1 mM EGTA, 10 mM HEPES, 4 mM Mg-ATP, and 0.4 mM Na-GTP at pH 7.3; adjusted to 295 mOsm with sucrose). These micropipettes were positioned using a micromanipulator (Sutter Instrument, MP-285). The extracellular solution for all recordings was Tyrode's buffer (125 mM NaCl, 2 mM KCl, 3 mM $CaCl_2$, 1 mM $MgCl_2$, 10 mM HEPES, and 30 mM glucose at pH 7.3; adjusted to 305–310 mOsm with sucrose). All patch-clamp data were acquired in voltage-clamp mode. Voltage waveforms were generated using a National Instruments DAQ (PCIe-6323) and sent to the Axopatch 200B. Currents were low-pass filtered at 10 kHz by an internal Bessel filter in the Axopatch 200B, and digitized at 50 kHz by the DAQ. Data were analyzed in MATLAB.

2.4.3 Preparation of Arch samples from *E. coli*

E. coli (strain BL21) were transfected with Archaerhodopsin-3 in the pET-28b vector under the T7 promoter and grown in LB containing 100 μg/mL kanamycin in a shaking incubator at 37 °C. At an OD_{600} of 0.5, protein expression was induced with 0.5

mM IPTG, and 5 μM all-*trans* retinal was added from a concentrated stock in DMSO. Cells were then returned to the incubator and grown for another four hours. Cells were harvested by centrifugation and sonicated on ice for 5 minutes in sonication buffer (150 mM TRIS, 20 mM NaCl, 5 mM $MgCl_2$, pH 7.0) using a tip sonicator. The lysate was centrifuged to collect the membranes and the supernatant was discarded. These crudely fractionated membranes were used for most experiments in the microscope. To obtain solubilized protein for transient absorption experiments, sonicated cell membranes were homogenized in a solubilization buffer (30 mM K_2HPO_4, 20 mM KH_2PO_4, 300 mM NaCl, pH 7.0, 1.5% N-Octyl-β-D-Glucopyranoside) using a glass/Teflon tissue homogenizer, and the mixture was rotated in a Falcon tube (~20 rpm) at 4 °C overnight. The detergent solubilized protein was centrifuged at 13,000 rpm for one hour; the supernatant was stored at 4°C and used for experiments within one week. [Although we used N-Octyl-β-D-Glucopyranoside (OG) for these experiments, I later discovered that 1.5% dodecyl-β-D-maltoside (DM) is a better detergent to use for the solubilization of Arch; while 1.5% OG is fine for the WT protein, Arch mutants (e.g. D95N) are much more stable in 1.5% DM.]

2.4.4 HEK cell culture

HEK293T cells were grown in DMEM supplemented with 10% FBS and penicillin/streptomycin in a 37 °C incubator under 5% CO_2. Cells were grown to 50-70% confluency in 3 cm dishes. 48 hours prior to experimentation, cells were transfected using Transit-293 (Mirus) with a WT Arch-GFP fusion construct under either the CAMKII (Addgene plasmid 22217) or ubiquitin promoter. These cells were trypsinized and re-

plated at a density of ~5,000-10,000 cells/cm^2 on matrigel-coated coverglass bottom dishes (P35G-1.5-14-C, MatTek) 12 – 24 hours before experimentation. Although there is some retinal present in FBS, we added all-*trans* retinal (5 µM, from a stock at 50 mM in DMSO) to each dish 1 - 2 hours prior to imaging.

2.4.5 Measuring fluorescence vs. voltage

We measured Arch fluorescence as a function of membrane voltage (Fig. 2-4) on HEK cells under whole-cell voltage clamp. The control voltage was a triangle wave between -150 mV and +150 mV, for 10 cycles at a sweep rate of 200 mV/s. The sweep rate was sufficiently slow that no electrical compensation was needed. We recorded fluorescence on a camera and took the average signal from a patch of membrane selected to avoid fluorescence from Arch molecules that had not trafficked to the membrane. We also subtracted background fluorescence from the coverglass and the medium by recording the same signal from a cell-free area of the dish.

The fit to a Hill curve in Figure 2-4a is based on a model of thermal equilibrium between two states whose energies are separated by $\alpha(V - V_0)$. The fluorescence is:

$$F = F_1 + \frac{F_2 - F_1}{1 + e^{\frac{\alpha(V-V_0)}{kT}}} \qquad \text{[Eq. 2.1]}$$

Where F_1 and F_2 represent the fluorescence produced by each state and αV_0 is the difference in the states' energies in the absence of applied voltage. We fitted Eq. 2.1 to our data on F vs. V, subject to the constraint that F_1 and F_2 must be positive, yielding α = 0.15 and V_0 = -280 mV. Allowing a 1% rms error gives bounds 0.09 < α < 0.35 and -330 < V_0 < -50 mV.

2.4.6 Measuring fluorescence response to a step in voltage

The response of Arch fluorescence to a step in voltage (Fig. 2-4b) was measured on HEK cells under whole-cell voltage clamp. We applied a square wave between -70 mV and +30 mV at 50 Hz, and collected the fluorescence on a PMT. The output of the PMT passed through an 8-pole Bessel filter with a cutoff of 25 kHz and was digitized at 50 kHz. The graph shows the response averaged for 1 min. Illumination was at 594 nm, 1000 W/cm^2.

A challenge in measuring fast step responses is that the membrane voltage, V_m lagged the voltage applied to the patch pipette, V_p. The capacitance of the cell membrane, C, and the series resistance of the pipette, R_p, combined to act as a low-pass filter ($R_pC \approx 0.5$ ms) on V_p. This filtering masked the true response speed of Arch. A common resolution to this problem is to use the 'compensation' circuitry in the patch clamp amplifier. The values of C and R_p are determined by observing the current produced in response to a step in V_p. The amplifier then generates a voltage waveform that exaggerates high frequency components of the desired signal to counteract the low-pass filtering of the cell.

Electrical compensation introduces some artifacts, however, because it neglects additional capacitances and resistances that lead to a more complex impulse response than can be accommodated by a simple *RC* filter. Additionally, to avoid instabilities in the amplifier, the compensation must be kept below 100%. We thus measured the step response without compensation, as shown in Figure 2-4b.

We modeled the response of membrane voltage V_m to a step in V_p as an exponential with time constant τ_V. This time constant was found from the relaxation time of the current in response to a step in V_p. In the experiment of Fig. 2-4b, τ_V = 0.4 ms. We modeled the fluorescence response of Arch to a step in V_m as an exponential with time constant τ_F. The response of Arch fluorescence, F, expressed as a fraction of its maximum response, to a step in V_p is:

$$F(t) = \frac{1}{\tau_F}\int_0^t \left(1 - e^{\frac{-t'}{\tau_V}}\right) e^{\frac{-(t-t')}{\tau_F}} dt'$$

$$= 1 + e^{\frac{-t}{\tau_F}}\left(\frac{\tau_V}{\tau_V - \tau_F} - 1\right) - e^{\frac{-t}{\tau_V}}\frac{\tau_V}{\tau_V - \tau_F} \qquad \text{[Eq. 2.2]}$$

Fitting the fluorescence to Eq. 2.2 with the single fitting parameter τ_F, we find τ_F = 0.4 ms for a step up in voltage and τ_F = 0.6 ms for a step down.

2.4.7 Measuring fluorescence vs. intensity

The dependence of Arch fluorescence on illumination intensity (Fig. 2-4c), was measured in a sample of crudely fractionated *E. coli* membranes containing Arch-eGFP. We varied the illumination intensity continuously using an AOTF. We monitored the laser power on a photodiode and the fluorescence on a PMT. Each measurement was repeated twice on the same sample region to check for sample degradation. To check for nonlinearities in the response of the photodiode or the PMT we performed the same experiment on a sample of fluorescent beads (Invitrogen). We placed neutral density filters on the excitation and emission paths to ensure that the PMT and photodiode were operating in the same range as they were during the Arch experiment. We found no nonlinearities in the electronics or detectors.

We determined the relative brightness of Arch and eGFP in a 1:1 Arch-eGFP fusion. eGFP was excited at 488 nm and emission was passed through a 531/40 bandpass filter. Arch emission was passed through a 710/100 bandpass filter. In both cases the fluorescence was collected on a PMT. The data was corrected for the wavelength dependence of the PMT quantum efficiency, which was nearly twice as high at 531 nm as at 710 nm.

2.4.8 Imaging sequential multiphoton excitation of Arch fluorescence in a cuvette

Figure 2-6 demonstrates the sequential multiphoton character of Arch fluorescence. The data was taken in a cuvette containing detergent-solubilized Arch-eGFP. Illumination was provided by two lasers: 473 nm to excite eGFP, 594 nm to excite Arch. To ensure that the beam shape parameters were identical for both channels, the beams were expanded and then cropped by an iris at the back of the objective (Olympus, 20× NA 0.4). The image was taken using a photographic lens (Nikon, 60 mm f/2.8) and an Andor EMCCD camera (iXon3 897). The image is a composite of a white light image of the cuvette (no emission filter) mapped to the white channel, an image of Arch fluorescence (710/100 emission filter, 594 excitation, 500 1 second exposures averaged) mapped to a red channel, and an image of eGFP fluorescence (531/40 emission filter, 473 nm excitation, 60 1 s exposures averaged) mapped to a green channel.

2.4.9 Action spectra

The action spectra of Arch (Fig. 2-7) were collected as follows:

1. Fluorescence and voltage sensitivity spectra were obtained from HEK cells (n = 4) expressing Arch. Membrane voltage was controlled by whole-cell patch clamp. Cells were illuminated with light from a supercontinuum laser at eight evenly-spaced wavelengths between 530 nm and 635 nm (set by an AOTF), at I = 10 W/cm^2. The AOTF was calibrated with a power meter to ensure that intensity did not change across wavelengths. Each cell was illuminated for 5 s at each wavelength while the voltage cycled through the values, in mV: 0, -100, 0, +100, 0, spending 1 s at each voltage. Fluorescence was recorded on an EMCCD, and the 150 most voltage-responsive pixels (corresponding to membrane-localized Arch) were selected for analysis using the weighting algorithm described previously [7].

The fluorescence excitation spectrum was determined from the mean fluorescence at each wavelength. The voltage sensitivity spectrum was determined from the difference between the fluorescence excitation spectrum at +100 mV and the spectrum at -100 mV.

2. The absorption spectrum was acquired on detergent-solubilized Arch (in solubilization buffer at pH 7.0) using a Nanodrop 2000c (Thermo Scientific) (Fig. 2-25). The path length was 1 cm. To determine the absolute extinction coefficient of Arch we extracted the retinal using a method based on that of El Sayed et al. [47]. Briefly, an aliquot of detergent-solubilized Arch was diluted 4x in a 2:1 chloroform:methanol solution. Retinal was cleaved from the protein by adding 20 μL of 1 M hydroxylamine. The resulting retinal oxime was collected in the chloroform fraction by shaking the

sample for ~5 minutes. An absorption spectrum of the chloroform showed a peak at 362 nm, corresponding to free retinal oxime (Fig. 2-25). Using the extinction coefficient of retinal oxime (60,000 $M^{-1}cm^{-1}$), we calculated the concentration of extracted retinal oxime.

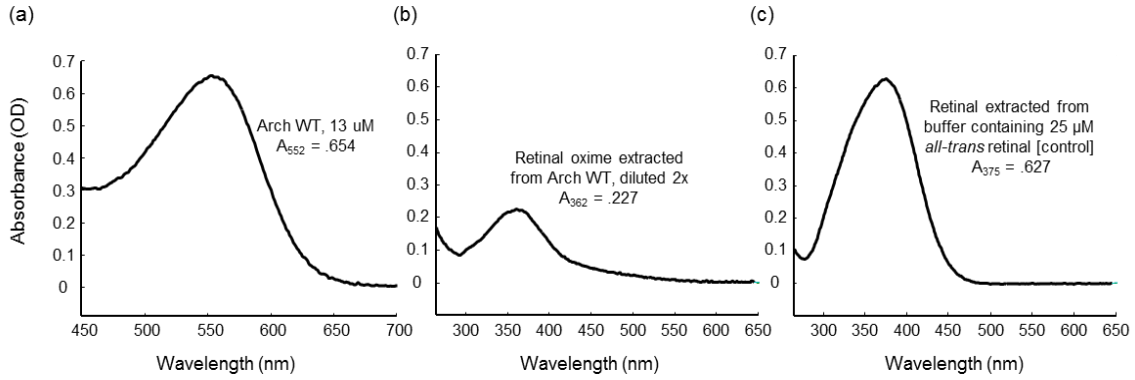

Figure 2-25. Determination of the extinction coefficient of Arch. (a) Absorption spectrum of detergent-solubilized Arch, pH 7. (b) Absorption spectra of retinal oxime extracted from the sample in (a). (c) Absorption spectrum of retinal extracted from a reference sample of known concentration.

We then repeated the chloroform extraction on a sample of free retinal of known concentration (25 μM) in solubilization buffer, and measured the absorption spectrum of the extracted retinal (Fig. 2-25). Using the extinction coefficient of *all-trans* retinal (43,000 $M^{-1}cm^{-1}$), we calculated that our extraction efficiency was ~58%. Assuming a 1:1 stoichiometry of retinal binding by Arch and an extraction efficiency of 58% for retinal oxime, we determined the concentration of the original Arch sample and used this to calculate the extinction coefficient of Arch at 552 nm (ε = 50,300 $M^{-1}cm^{-1}$).

3. The photocurrent action spectrum was obtained from a HEK cell expressing Arch. The membrane voltage was clamped at 0 V via whole-cell patch clamp. The cell was illuminated with light from a supercontinuum laser at eight evenly-spaced wavelengths between 530 nm and 635 nm (set by an AOTF), at I = 10 W/cm^2. Exposures (1 s) alternated with darkness (1 s). The difference in membrane current between these conditions yielded the photocurrent action spectrum.

2.4.10 Transient absorption

Transient absorption experiments (Fig. 2-10; Fig. 2-20) were performed on a home-built apparatus. Detergent-solubilized Arch at pH 6, 7, or 8 was held in a quartz cuvette. Excitation was provided by a frequency-doubled Nd:YAG laser (Spectraphysics INDI-40) producing 5 ns pulses at 532 nm, with a 20 Hz repetition rate. We used an optical chopper to block every second pulse, so the sample experienced flashes every 100 ms. White light from a 100 W mercury arc lamp (Olympus) passed through a motorized monochromator (Horiba Scientific, iHR320) then through the cuvette. The transmitted light was recorded on a photodiode (Thorlabs, DET36A) and digitized at 100 kHz on a National Instruments DAQ (PCIe-6259). We recorded for 5 s (50 pump cycles) at each wavelength, and cycled through the wavelengths 20 times.

We recorded absorption for every pump pulse, only averaging in post-processing, so that we could check for degradation of the sample. We saw some bleaching of the sample but the shape of the spectra did not change with time. We also recorded the photodiode signal with each of the beams (pump and probe)

independently shuttered to check for electrical artifacts. We varied the pump intensity to ensure that the signal was linear in pump intensity.

2.4.11 Fitting transient absorption data

We fit the transient absorption data in Fig. 2b to exponential curves of the form

$$I(\lambda, t) = \sum_{i=1}^{n} B_i(\lambda) e^{\frac{-t}{\tau_i}} \qquad \text{[Eq. 2.3]}$$

At 400 nm and 560 nm, the absorption vs. time traces were fit to this equation with n = 3 to determine the rates ("τ") and weights ("B") shown in Table 2-1. The first two time constants from this fit were held as fixed parameters when fitting the absorption vs. time at 640 nm to an equation of the same form (with n = 4, τ_1 = .04 ms, and τ_2 = .39 ms). The rates and weights from this fit are shown in Table 2-1. The fits to the data at all three wavelengths are plotted as black lines in Figure 2-10b.

	τ_1 = .04 ms	τ_2 = .39 ms	τ_3 = 4.1 ms	τ_4 = 14.3 ms	τ_5 > 100 ms
400 nm	-1.7	4.8	*n/a*	*n/a*	.5
560 nm	1.7	-5.3	*n/a*	*n/a*	-3.9
640 nm	.30	-.34	-.65	.90	*n/a*

Table 2-1. Weights ($B_i \times 10^3$) of indicated components from fitting transient absorbance data in Figure 2-4b to Eq. 2.3 with n = 3 (400 nm, 560 nm) or n = 4 (640 nm).

2.4.12 Transient fluorescence

Transient fluorescence measurements (Fig. 2-12) were performed on crudely fractionated *E. coli* membranes containing Arch, in our home-built microscope. Pump pulses were 532 nm, 50 W/cm^2, and lasted 100 µs. To minimize the perturbation due to the probe, we used dim red probe pulses (640 nm, 15 W/cm^2), and only recorded fluorescence during the first 20 µs of the probe pulse. We verified that the fluorescence

signal was linear in probe intensity. We waited 150 ms between pump pulses. Waiting longer did not affect the data.

Each data point represents the average of 30 pump-probe cycles. PMT and photodiode signals were filtered at 50 kHz and digitized at 100 kHz. The raw data traces showed negligible sample degradation during these experiments.

The triple pulse (pump-pump-probe) scheme provides rich information on light-driven transitions of photocycle intermediates, and the lifetimes of the resulting states. In addition to the data shown in Fig. 2-12 we varied the intervals between pulses (Figure 2-13), the wavelength of each pump (Figure 2-14) and the intensity of each pump (Figure 2-15).

2.4.13 Confocal scan

Figure 2-17 shows four images taken on a commercial scanning confocal microscope (Zeiss LSM 710) of a HEK293T cell expressing an Arch-eGFP fusion. Arch was excited at 594 nm and eGFP was excited at 488 nm. The scan rate was 0.47 ms per line. The 'line scan' mode scanned each line 16 times before moving on to the next line whereas the 'frame scan' mode scanned the entire field of view, line-by-line, and repeated 16 times.

2.4.14 Time- and voltage-dependent fluorescence in HEK cells

Time-dependent fluorescence and photocurrent (Fig. 2-18, 2-21a) were measured in single HEK cells expressing Arch under whole-cell voltage clamp.

To investigate the fluorescence response to onset of illumination at different voltages (Fig. 2-18a), the membrane potential was set to -100 mV or +100 mV via whole

cell patch clamp. The cell was exposed to a pulse of light (50 ms, 594 nm, 1000 W/cm^2) followed by 250 ms of darkness and the fluorescence was recorded (Fig. 4a). The cycle was repeated 10 times. Average fluorescence responses show that fluorescence and voltage sensitivity arose several milliseconds after onset of continuous illumination.

To investigate the fluorescence response to a brief flash of light (Fig 2-18b, F and ΔF), we initiated the photocycle with a flash (1000 W/cm^2, 100 μs, 594 nm), and then probed the fluorescence with a second flash (1000 W/cm^2, 100 μs, 594 nm) with variable delay, *t*. Each data point is the average of 80 pump-probe measurements. To measure F, the membrane voltage was clamped at V_m = 0. To measure ΔF, the membrane voltage was held fixed at +30 mV and then at -70 mV.

The probe flashes were sufficiently intense to drive *N* → *Q* and to excite fluorescence of *Q*, i.e. to provide photons 2 and 3 in the scheme of Fig. 2-16. Intense probe beams were necessary for the single-cell measurements due to the much smaller sample volume compared to the experiments on fractionated *E. coli* membranes. The fluorescence measured at the single-cell level peaked at *t* = 5 ms, similar to that measured in bulk (Fig. 2-12(iii)). Considering the different protein environments (crudely fractionated *E. coli* membranes vs. intact HEK cells), we do not consider the difference in timing to be significant.

To investigate the effect of violet flashes on steady-state fluorescence and photocurrent at different voltages (Fig. 2-21a, 2-22), the membrane potential was varied in steps of 30 mV from -90 mV to +60 mV. At each voltage, pulses of red light were applied to elicit steady-state fluorescence and photocurrent (100 ms, 640 nm, 4000

W/cm^2). 54 ms after turning on the red light, a short pulse of violet light (11 ms, 407 nm, 40 W/cm^2) was applied to the cell to perturb steady-state fluorescence and photocurrent. The red light was turned off for 100 ms between red pulses. This procedure was repeated four times at each voltage. Background fluorescence due to the 407 nm light alone was subtracted from fluorescence measurements.

2.4.15 Ground-state recovery probed by two-pulse photocurrent

The integrated photocurrent following a brief pulse of light provides a measure of the ground state population of Arch. By measuring this photocurrent under a two-pump protocol with variable delay, we probed the duration of the photocycle.

HEK cells expressing Arch were held at a membrane voltage of 0 mV via whole cell patch clamp. Cells were exposed to two flashes of light (100 μs, 594 nm, 1000 W/cm^2) with variable delay, t_{probe}. Membrane current was recorded continuously. The protocol was repeated at 600 ms intervals.

2.4.16 Model of voltage-dependent fluorescence in Arch

We modeled the photocycle of Figure 2-21b quantitatively. We assigned rates to each transition in this model: k_{GM} = ground to *M* under red illumination (with no red light, k_{GM} = 0); k_{NG} = *N* to ground; k_{MG} = *M* to ground under violet illumination (with no violet light, k_{MG} = 0). We assigned fractional charge movements to each forward transition in the model (Q_{GM} and Q_{NG}) such that the total charge moved in the photocycle is 1 (Q_{GM} + Q_{NG} = 1), and we assumed that the charge movement from ground to M is equal and opposite to the charge movement from *M* to ground (Q_{GM} +

Q_{MG} = 0). We assumed that *M* and *N* equilibrate quickly to an equilibrium given by *K*(*V*) satisfying a two-state Boltzmann distribution:

$$K(V) = e^{\frac{\alpha(V-V_0)}{k_B T}}$$

We further assumed that fluorescence was proportional to the population of *N*, with proportionality constant F_1 allowing for a small constant background fluorescence, F_0. The populations evolve according to:

$$M = N/K$$

$$\frac{d}{dt}\begin{bmatrix} G \\ N \end{bmatrix} = \begin{bmatrix} -k_{GM} & k_{NG} + k_{MG}/K \\ k_{GM}K/(K+1) & -k_{NG}K/(K+1) - k_{MG}/(K+1) \end{bmatrix}\begin{bmatrix} G \\ N \end{bmatrix}$$

while the fluorescence *F* and current *I* are given in terms of the states' populations:

$$F = F_0 + F_1 N$$

$$I = I_1(Q_{GM}k_{GM}G - Q_{GM}k_{MG}M + Q_{NG}k_{NG}N)$$

where I_1 is the constant of proportionality equal to the number of molecules in the membrane.

We solved for the N population after the onset of illumination:

$$N(t) = \frac{\left(1 - e^{-\frac{(\mathrm{k_{MG}} + \mathrm{k_{GM}} + K(\mathrm{k_{NG}} + \mathrm{k_{GM}}))t}{1+K}}\right) K\mathrm{k_{GM}}}{\mathrm{k_{MG}} + \mathrm{k_{GM}} + K(\mathrm{k_{NG}} + \mathrm{k_{GM}})}$$

which reduces to the following under steady-state illumination (t = ∞):

$$N = \frac{K\mathrm{k_{GM}}}{\mathrm{k_{MG}} + \mathrm{k_{GM}} + K(\mathrm{k_{NG}} + \mathrm{k_{GM}})}$$

Fluorescence and current were calculated using the equations given above under both steady-state illumination and as a function of time after the onset of red illumination (k_{MG} = 0). This model was able to reproduce the main features of the data shown in Figure 4(d) using the following parameters: k_{GM} = .5 ms^{-1}, k_{NG} = .033 ms^{-1}, k_{MG} = .2 ms^{-1}, Q_{GM} = 0.09, α = 0.35, and V_0 = -30 mV. The fits resulting from using these parameters are shown in Fig. 2-22.

3
Flash Memory

We developed a technique, “Flash Memory”, to record a photochemical imprint of the activity state – firing or not firing – of a neuron at a user-selected moment in time. The key element is an engineered microbial rhodopsin protein with three states. Two non-fluorescent states, D_1 and D_2, exist in a voltage-dependent equilibrium. A stable fluorescent state, F, is reached by a photochemical conversion from D_2. When exposed to light of a wavelength λ_{write}, population transfers from D_2 to F, at a rate determined by the $D_1 \rightleftharpoons D_2$ equilibrium. The population of F maintains a record of membrane voltage which persists in the dark. Illumination at a later time at a wavelength λ_{read} excites fluorescence of F, probing this record. An optional third flash at a wavelength λ_{reset} converts F back to D_2, for a subsequent write-read cycle. The Flash Memory method offers the promise to decouple the recording of neural activity from its readout. In principle, the technique may enable one to generate snapshots of neural activity in a large volume of neural tissue, e.g. a complete mouse brain, by circumventing the challenge of imaging a large volume with simultaneous high spatial and high temporal resolution. The proof-of-principle Flash Memory sensors presented here will need improvements in sensitivity, speed, brightness and membrane trafficking before this goal can be realized.

3.1 Introduction

To create detailed maps of brain function, one would like to observe the simultaneous activity of thousands or millions of neurons in the intact brain of a behaving animal. Large-scale maps of activity at single-neuron and single-spike resolution could give insights into fundamental mechanisms of neural processing. One could map the patterns of activation associated with simple sensory processing tasks, or with complex activities such as feeding, locomotion, or social interactions. By correlating the activity of large numbers of single cells, one might deduce rules of neuronal information processing.

Recent efforts in "connectomics" have focused on mapping large-scale neural structure using optical [48] [49] and electron [50, 51] microscopies. Clever GFP labeling schemes facilitate tracing of neuronal connections in genetically specified cell types [52]. However, connectomic mapping is typically implemented in fixed tissues, and thus is incompatible with functional recording.

Genetically encoded voltage and calcium reporters are now widely used for optical recording of neural activity in vitro and in vivo [7, 53, 54]. These tools are typically used to record from a relatively modest number of cells (< 1,000) in a single field of view. A recent technical tour-de-force demonstrated whole-brain calcium imaging in a live zebrafish [55], but the imaging bandwidth of 0.8 Hz was ~1,000-fold slower than the duration of a single action potential.

One might like to combine large-scale 3D imaging with functional reporters to achieve "functional connectomics," i.e. brain activity mapping. Two challenges have

stood in the way. First, optical scattering limits imaging in live brain tissue to a depth of ~1 mm. To image at greater depth, the brain must be fixed and either chemically clarified [49], or sliced into thin sections [48]. Second, existing microscopes cannot image large volumes fast enough to resolve simultaneous action potentials (~1 ms) or calcium transients (~200 ms) in large numbers of cells. For a fast voltage indicator, the signal from a neuronal spike lasts only as long as the spike itself. To image a cubic millimeter of brain with millisecond temporal resolution and micron spatial resolution would require a data rate > 10^{13} bits/s, well beyond the bandwidth of existing or conceived microscopes.

An alternate strategy is to convert neural activity in a user-defined epoch into a long-lasting (bio)chemical signal to be read at a later time. In the technique of Targeted Recombination in Active Populations (TRAP), the simultaneous presence of neural activity and a drug (tamoxifen) leads to activation of a Cre recombinase and subsequent expression of mCherry [56]. This technique captured average levels of neural activity over a ~12 hr. window. Several proposals have been offered for activity integrators with higher time-resolution [57, 58], but to our knowledge none has been implemented.

Optical gating of an activity recorder is particularly attractive because (a) the optical control signal can be gated with nearly arbitrary temporal precision, and (b) photons used to regulate a photochemical process need not follow a straight-line path from the source to the molecular target. While optical scattering lengths in brain are typically ~60 mm [59], diffusive transport of photons can easily fill an entire rodent brain with light. Thus delivery of an optical control signal is relatively straightforward and

does not require sophisticated optics. Naturally occurring and engineered rhodopsin proteins have previously been demonstrated to show optical bistability [46, 60, 61], and also to show voltage-dependent switching [7, 10, 33, 62, 63]; but the combination of these two attributes has not, to our knowledge, been demonstrated.

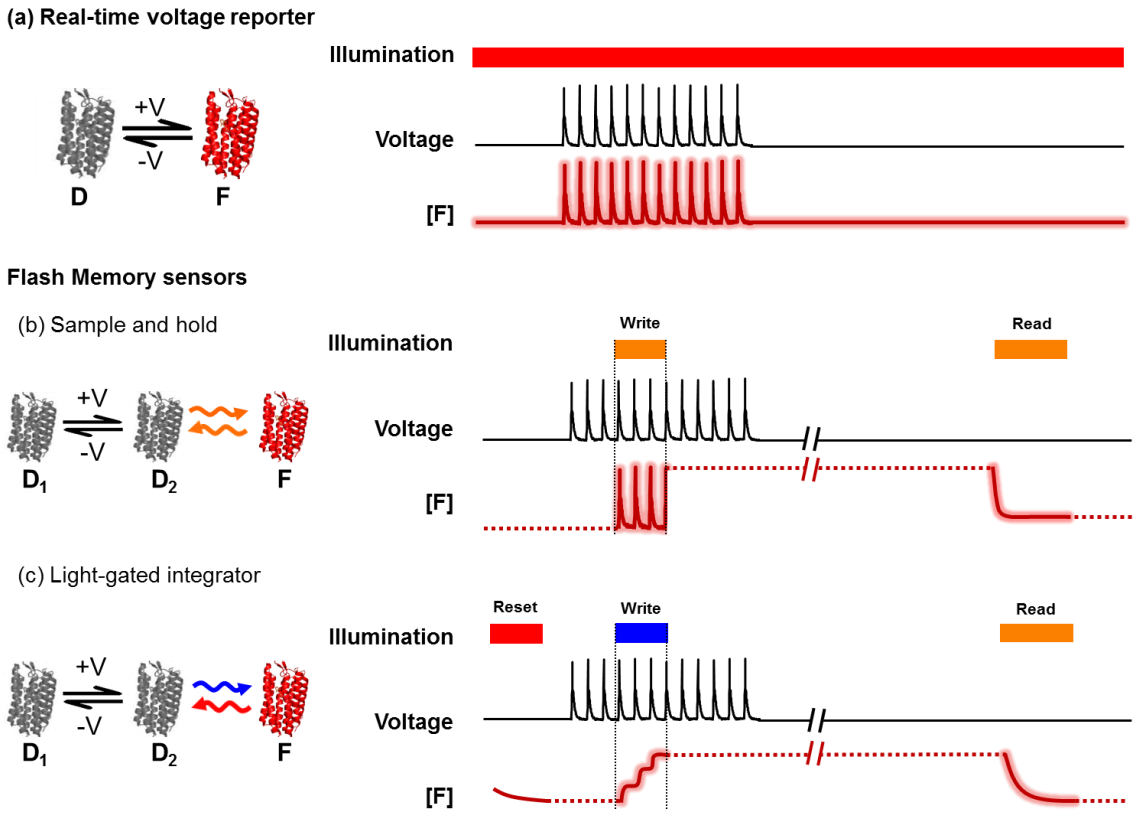

Figure 3-1. Classes of voltage indicators. (a) In a real-time voltage reporter, the population in a fluorescent state, F, is a function of membrane voltage, regardless of illumination. (b) In a sample and hold voltage sensor, voltage establishes a D1 ⇌ D2 equilibrium and a write pulse establishes a rapid D2 ⇌ F equilibrium. Thus the population of F tracks the membrane voltage. The population of F is frozen at the end of the write pulse. (c) In a light-gated voltage integrator, voltage establishes a D1 ⇌ D2 equilibrium and a write pulse drives the unidirectional D2 → F transition. Thus the population of F accumulates in a voltage-dependent manner. The population of F is frozen at the end of the write pulse. In both types of Flash Memory sensor, the population of F persists in the dark and is later probed via a read pulse that elicits fluorescence.

Here we demonstrate two proof-of-principle approaches to light-gated photochemical recording of membrane voltage. Both are based on transmembrane proteins which undergo both voltage- and light-induced conformational changes. Figure 3-1 compares the operation of a standard real-time voltage indicator (Fig. 3-1a) to the light-gated reporters (Figs. 3-1b and 3-1c). Conventional real-time voltage reporters interconvert between non-fluorescent and fluorescent states in a voltage-dependent manner; illumination probes the population in the fluorescent state but does not affect the conformation. Light-gated voltage reporters have separate voltage- and light-driven transitions. Formation of a fluorescent product requires simultaneous presence of a depolarizing voltage and illumination. The three-state models shown in Figs. 3-1b and 3-1c illustrate plausible reaction topologies which could lead to this behavior.

In a sample and hold sensor (Fig. 3-1b), the population in the fluorescent state tracks the membrane voltage during illumination at a wavelength l_{write}; interconversion ceases the moment the write pulse ends. Illumination at a wavelength l_{read} at a later time probes the quantity of fluorescent product that existed at the end of the write pulse. These sensors could be used to record snapshots of neural activity at a moment in time.

In a light-gated voltage integrator (Fig. 3-1c), the population in the fluorescent state accumulates in a voltage-dependent manner during a write pulse. Production of the fluorescent state ceases at the end of the write pulse. A read pulse probes the fluorescence at a later time. Integrators could be used to determine the cumulative level of neuronal activity during a period of illumination. The “sample and hold” and

“light-gated-integrator” mechanisms are limiting cases of a continuous distribution of light-gated voltage reporters, distinguished by light-dependent kinetics into and out of the fluorescent state during the write pulse. We call the techniques of Figs. 3-1b and 3-1c Flash Memory for their ability to store a record of neural activity upon a flash of light.

The three-state reaction schemes of Figs. 3-1b and 3-1c occur as a motif within the voltage- and illumination- dependent photocycle of Archaerhodopsin-based voltage indicators (Fig. 3-2) [2]. While Flash Memory behavior was not observed in the wild-type protein, we hypothesized that mutants of Arch might show kinetics favoring Flash Memory behavior. We introduce the three-state model here as a conceptual framework for interpreting the data that follows. Simulations of this model are given at the end of this section.

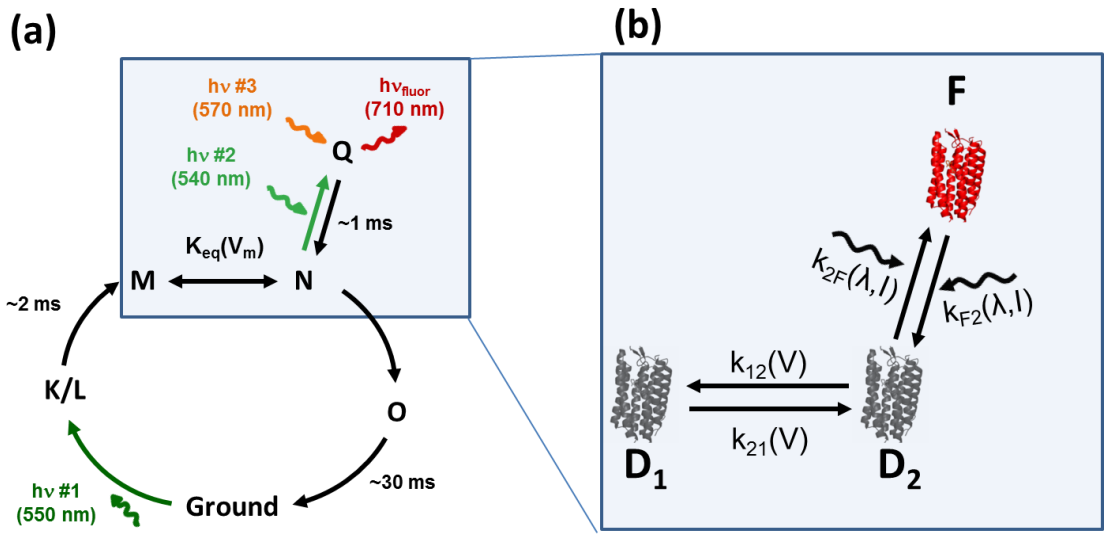

Figure 3-2. The 3-state motif of a Flash Memory sensor appears in the photocycle of WT Arch. (a) Voltage-dependent photocycle of wild-type Arch (adapted from [2]). In the wild-type protein, absorption of photon hν #1 in the ground state initiates the photocycle. A voltage-dependent equilibrium is established in the *M-N* manifold. Photon hν #2 converts population from the *N* state into the fluorescent *Q* state. A third photon (hν #3) excites fluorescence of Q. (b) Simple model of Flash Memory sensors. The transitions shown in the blue box in (a) are sufficient to describe Flash Memory behavior, comprising a voltage-dependent equilibrium in a dark manifold, and a light-driven transition to a fluorescent state. In wild-type Arch reversion from the fluorescent state to the main photocycle occurs thermally. In Flash Memory sensors this transition should only be driven by light. Additional spectroscopic characterization will be needed to make a definitive assignment of the states in (b) to states in the canonical photocycle shown in (a) and to determine the role, if any, of other states.

We give a detailed photophysical characterization of two Flash Memory sensors, engineered by mutating the real-time voltage reporter Archaerhodopsin-3 (Arch). The mutant Arch(D95H) approximates a sample and hold sensor, albeit with a slow (48 ms) response to changes in voltage. We used Arch(D95H) to make a photochemical recording of action potentials in a cultured neuron. The mutant Arch(D95Q) approximates a light-gated voltage integrator, albeit with poor sensitivity to single spikes. We used Arch(D95Q) to count exogenously delivered voltage spikes in a HEK cell (it did not traffic well enough for use in neurons).

Applications in tissue and in vivo will require further technical developments in the protein reporter and in the optical instrumentation and imaging protocols. Screens of Arch mutants and other microbial rhodopsins may yield reporters with improved sensitivity, kinetics, brightness, and membrane trafficking. Raman or 2-photon readout modalities may prevent spurious resetting of proteins by scattered imaging light. For applications where the tissue is fixed and sliced prior to imaging, the robustness of the signal to these procedures must be tested. While whole-brain activity mapping is the ultimate goal, imaging of increasingly large brain sub-regions will provide useful waypoints.

3.2 Results

We hypothesized that mutants of Archaerhodopsin-3 could function as Flash Memory sensors. Aspartic acid 95 (analogous to D85 in bacteriorhodopsin) is the proton acceptor from the Schiff base. Our lab [2] and others [64] have shown that mutation of this residue can eliminate proton pumping and can modulate photophysical properties of the protein. We generated a library of 20 Arch(D95X) mutants and screened for the three attributes of a Flash Memory sensor: bistability, voltage-sensitivity in the light, and absence of voltage sensitivity in the dark. Figure 3-3 shows the rich colors observed in pellets of E. coli expressing some of these mutants.

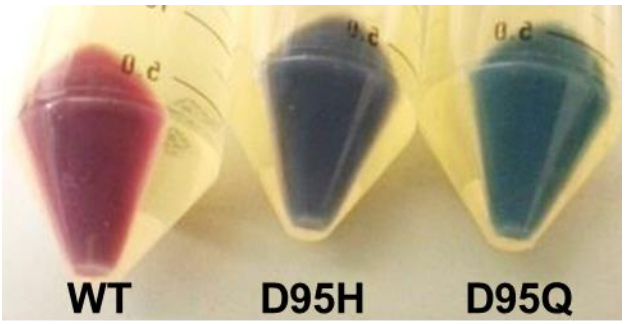

Figure 3-3. Arch(D95X) mutants expressed in E. coli are colorful. Mutation of residue D95 in Arch shifts its absorption spectrum; this is apparent upon visual inspection of bacteria expressing these proteins.

3.2.1 Arch(D95H) and Arch(D95Q) are bistable

We tested all Arch(D95X) mutants for bistability, using fluorescence of the retinal chromophore as a readout. We expressed each mutant in E. coli (Methods), added carbonyl cyanide m-chlorophenyl hydrazine (CCCP) to neutralize the membrane potential, and formed a small bacterial pellet for initial spectroscopic characterization. We illuminated each mutant with sixteen illumination sequences of the form: (I_{write}, t_{dark}, I_{read}), with I_{write} and I_{read} (1 s each, 10 W/cm^2) selected from all pairwise combinations of: 500 nm, 545 nm, 590 nm, and 635 nm (see section 3.4.3 for experimental details). We fixed t_{dark} = 5 s. We asked whether the initial fluorescence elicited by I_{read} depended on I_{write}. Such a dependence indicates the presence of at least two states that were stable for at least 5 s in the dark. In all cases emission was collected from 660 – 760 nm.

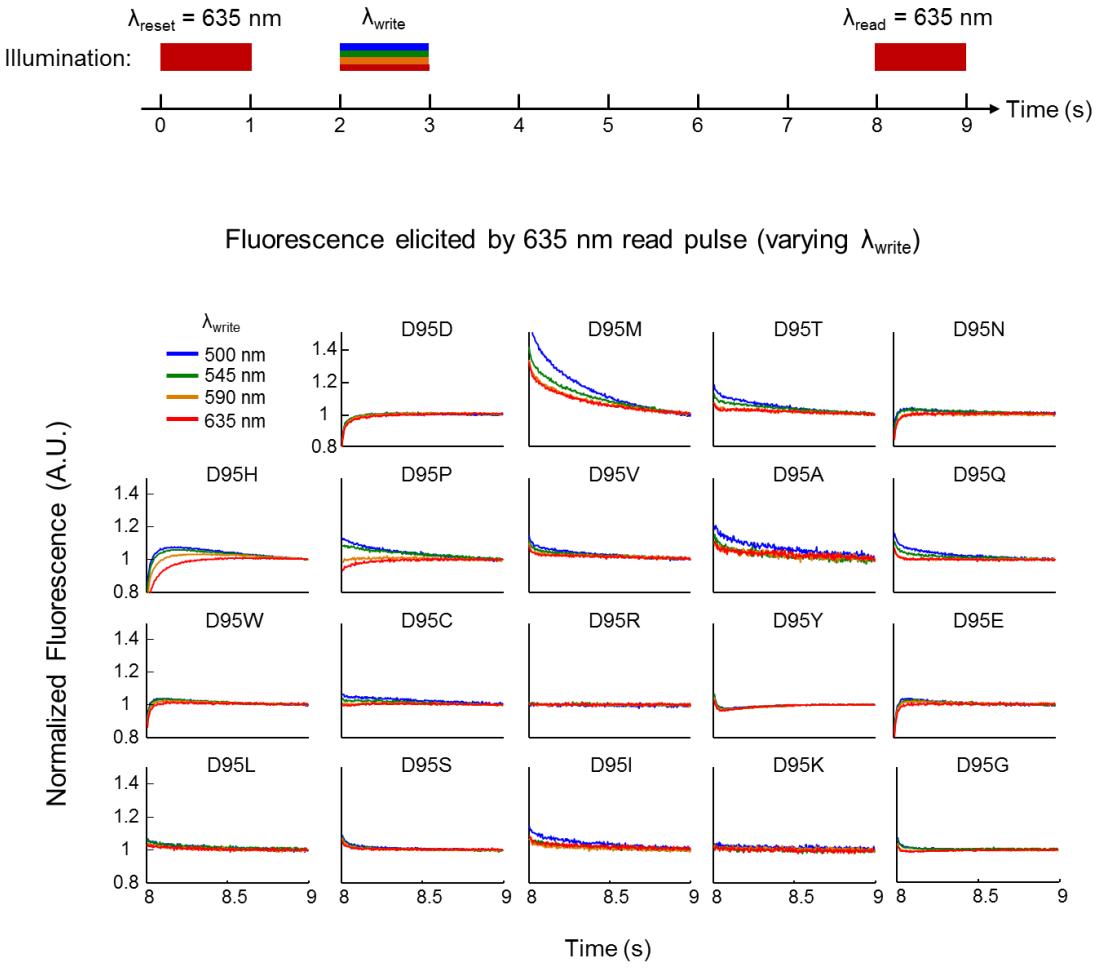

Figure 3-4. Bistability of Arch(D95X) mutants. Each Arch(D95X) mutant was expressed in E. coli and illuminated with the pulse sequence shown. λ_{write} was selected from: 500 nm, 545 nm, 590 nm, and 635 nm. Fluorescence elicited by a 1-second read pulse between t = 8 s and t = 9 s is shown for each mutant, normalized to the fluorescence at the end of the read pulse. The mutants in which the initial fluorescence elicited by the read pulse varied the most with λ_{write} were: D95H (24%), D95P (21%), D95M (19%), D95T (11%), D95A (9%), and D95Q (8%). Discrepancies between the temporal dynamics of transients observed in Figure 3-4 and those observed in our other data are attributed to differences in the experimental setup and illumination protocol used to acquire this data (see Materials and Methods in section 3.4).

All mutants showed some degree of bistability (Fig. 3-4). The mutant D95H showed the largest effect. Its brightness and fluorescence excitation and emission spectra are characterized in Fig. 3-5.

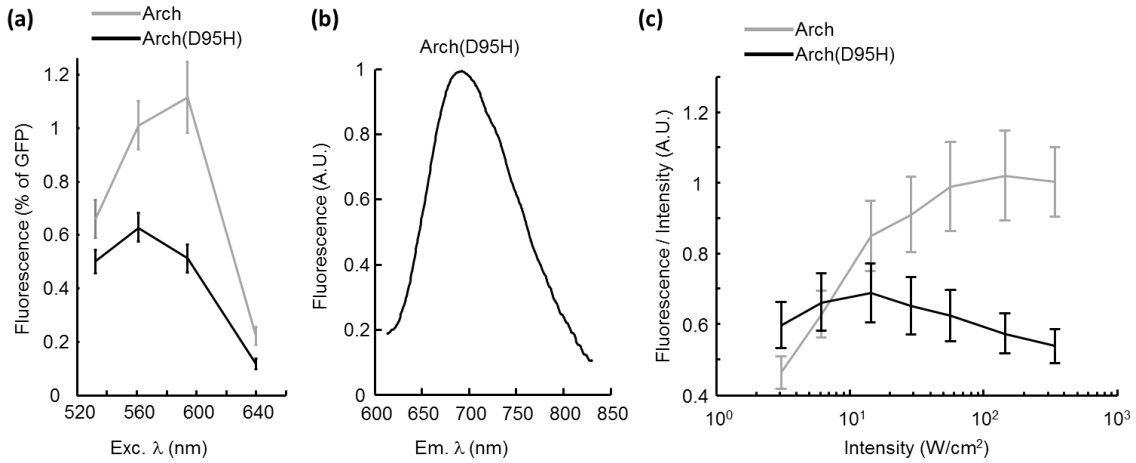

Figure 3-5. Photophysical properties of Arch(D95H) (a) Fluorescence excitation spectra of Arch(D95H) and wild-type Arch. Illumination intensity was 143 W/cm^2, emission was collected from 671 – 746 nm. Fluorescence intensities were normalized to fluorescence of eGFP expressed in an Arch-eGFP fusion. Error bars represent mean ± s.d. (n = 5 cells). (b) Fluorescence emission spectrum of Arch(D95H). Excitation was at 532 nm. (c) Fluorescence as a function of illumination intensity for Arch(D95H) and wild-type Arch. The plot shows fluorescence divided by illumination intensity. An ideal linear fluorophore would appear as a horizontal line. Wild-type Arch shows a well documented increase in brightness with increasing illumination intensity. Fluorescence of Arch(D95H) is approximately linear in illumination intensity.

Fluorescence of Arch(D95H) excited at l_{read} = 635 nm was 24% brighter with l_{write} = 500 nm than with l_{write} = 635 nm (Fig. 3-4). To test whether Arch(D95H) was bistable in mammalian cells, we expressed the protein in HEK cells and illuminated the sample with l_{write} = 488 nm or 640 nm, t_{dark} = 1 s, and l_{read} = 640 nm (I = 200 W/cm2), while using whole-cell voltage clamp to maintain a membrane voltage of 0 mV. Illumination at l_{write} = 488 nm caused greater initial fluorescence during the read interval than did illumination at l_{write} = 640 nm (Fig. 3-6).

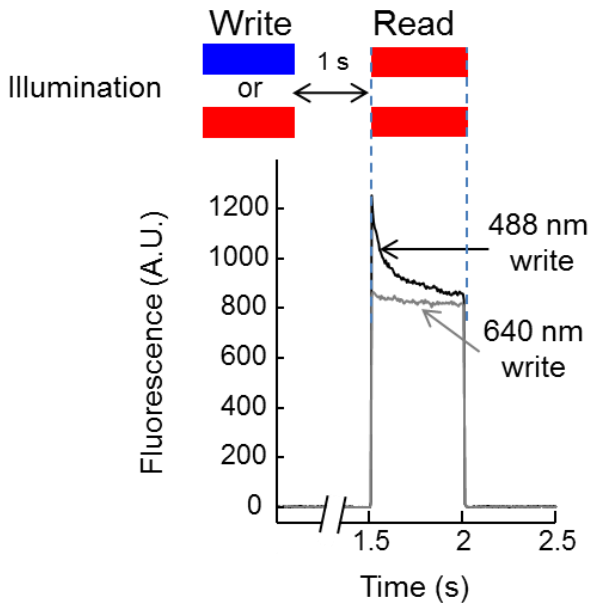

Figure 3-6. Bistability of Arch(D95H) expressed in HEK cells. Initial fluorescence under red excitation (lread = 640 nm) was different for l_{write} = 640 nm than for l_{write} = 488 nm. The write pulse was 500 ms, 200 W/cm2 and the dark interval was t_{dark} = 1 s.

To illustrate the bistability of Arch(D95H), we imprinted a photochemical image into a lawn of E. coli expressing Arch(D95H). A digital micromirror array was used to project an image at l_{write} = 488 nm (0.7 W/cm^2) into the microscope and onto the cells. After t_{dark} = 5 s, the cells were illuminated with homogeneous full-field illumination at lread = 640 nm (40 W/cm^2), revealing the latent image in the near infrared fluorescence (Fig. 3-7a). After several seconds of illumination at 640 nm the image faded. This process could be repeated in the same field of view with subsequent patterns written by blue light and read by red light.

We varied t_{dark} to measure the lifetime of bistability in Arch(D95H) (Fig. 3-7b). A grid pattern of blue light was projected onto the lawn of E. coli. After variable delay, the pattern was probed via wide-field red illumination and near infrared fluorescence. The

contrast remained stable at ~10% out to the longest time measured, tdark = 53 minutes (Fig. 3-7b, inset). There was also a slow (tens of minutes) increase in the overall brightness of the image, occurring equally in the regions that had and had not been exposed to blue light. The source of this gradual increase in fluorescence is not known, though we speculate that it may have been caused by stray light inducing a gradual buildup of the fluorescent state.

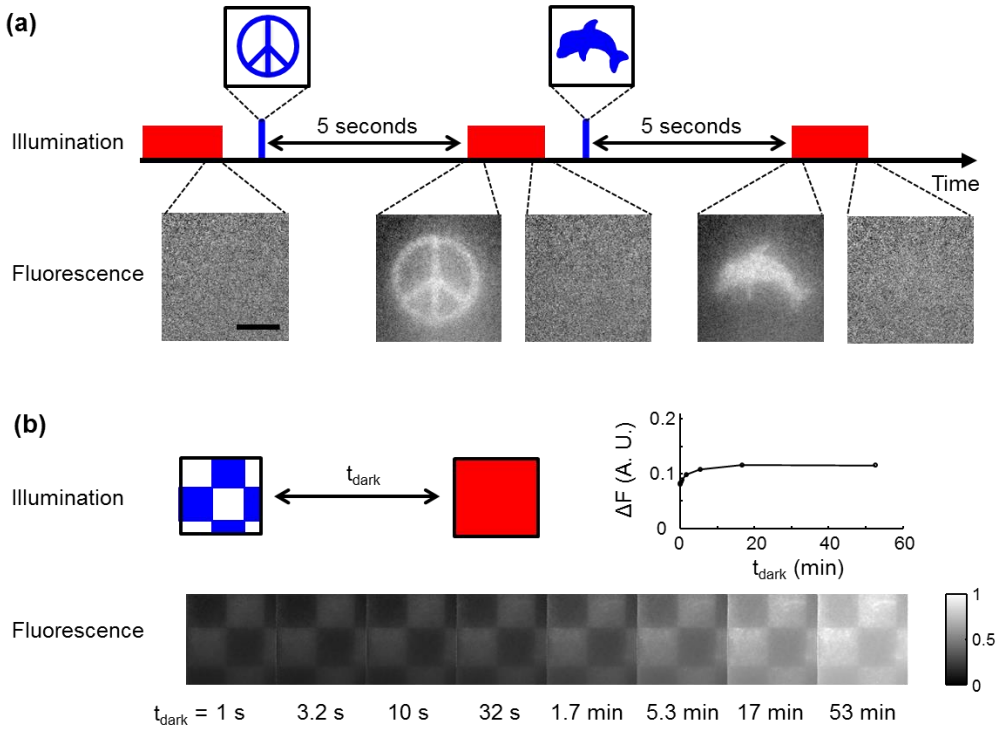

Figure 3-7. Visualizing bistability of Arch(D95H) in E. coli (a) Imprinting of photochemical images in a lawn of E. coli expressing Arch(D95H). Illumination with a pattern of blue light converted Arch(D95H) into a long-lived fluorescent state. After a 5 s delay, the pattern was probed with red excitation and near infrared fluorescence. The red illumination eventually erased the pattern. The process was repeated on the same cells with a different pattern. Scale bar 50 mm. (b) Monitoring lifetime of bistability. A checkerboard pattern was imprinted via blue light, and probed via red-induced fluorescence after a variable delay t_{dark}. Inset graph shows the difference in fluorescence of the bright and dark squares as a function of tdark.

Several other mutants, including Arch(D95Q), showed significant bistability in our screen of the Arch(D95X) library. For D95Q, fluorescence excited at l_{read} = 635 nm was 8% brighter with l_{write} = 500 nm than with lwrite = 635 nm (Fig. 3-4). Arch(D95Q) also showed bistability in HEK cells (Fig. 3-8).

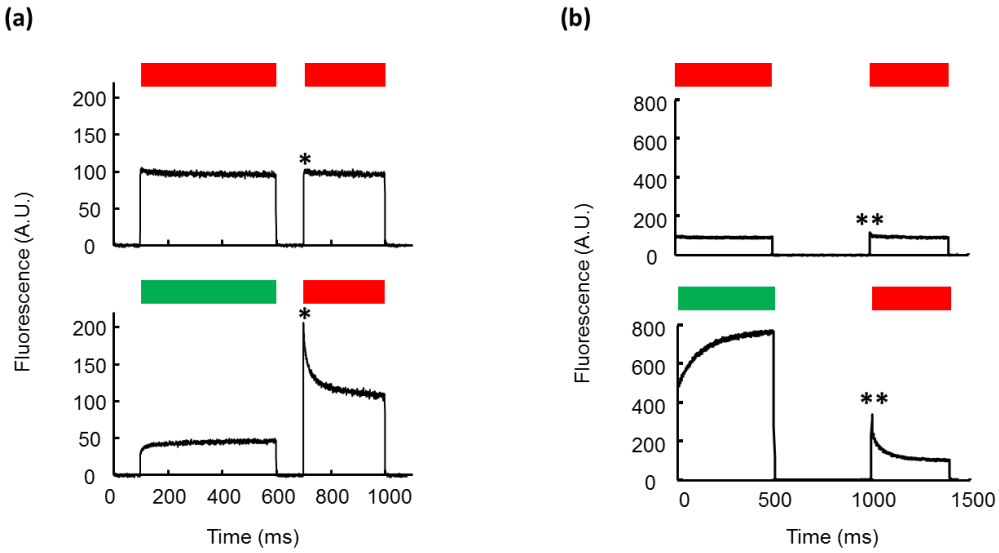

Figure 3-8. Bistability of Arch(D95H) and Arch(D95Q) in HEK cells held at constant voltage (V_m = -100 mV). (a) Initial fluorescence of Arch(D95H) with λ_{read} = 640 nm (indicated with a *) was greater with λ_{write} = 532 nm (bottom) than with λ_{write} = 640 nm (top). (b) Initial fluorescence of Arch(D95Q) with λ_{read} = 640 nm (indicated with a **) was greater with λ_{write} = 532 nm (bottom) than with λ_{write} = 640 nm (top).

3.2.2 Arch(D95H) and Arch(D95Q) are voltage sensitive under illumination

We expressed all 20 Arch(D95X) mutants in HEK cells and characterized their fluorescence (l_{exc} = 640 nm, l_{em} = 660 – 760 nm) as a function of membrane potential (V_m = -150 mV to +150 mV). Figure 3-9a shows the experimental setup. All mutants whose fluorescence could be detected showed some degree of voltage sensitivity. At V_m = +150 mV Arch(D95H) was 2-fold brighter than at V_m = -150 mV (Fig. 3-9b). Arch(D95Q) showed the greatest voltage sensitivity, with fluorescence > 7-fold higher at

+150 mV than at -150 mV (Fig. 3-9c), a consequence of having almost no fluorescence at V_m = -150 mV. Arch(D95H) generated a small hyperpolarizing photocurrent (5 pA) under intense illumination at 640 nm (500 W/cm^2). Arch(D95Q) generated no detectable photocurrent. Wild-type Arch typically generated photocurrents > 100 pA, so we deem the small photocurrent of Arch(D95H) to be insignificant. Due to the simultaneous presence of optical bistability and voltage-sensitive fluorescence in Arch(D95H) and Arch(D95Q), we further characterized these mutants as prospective Flash Memory sensors.

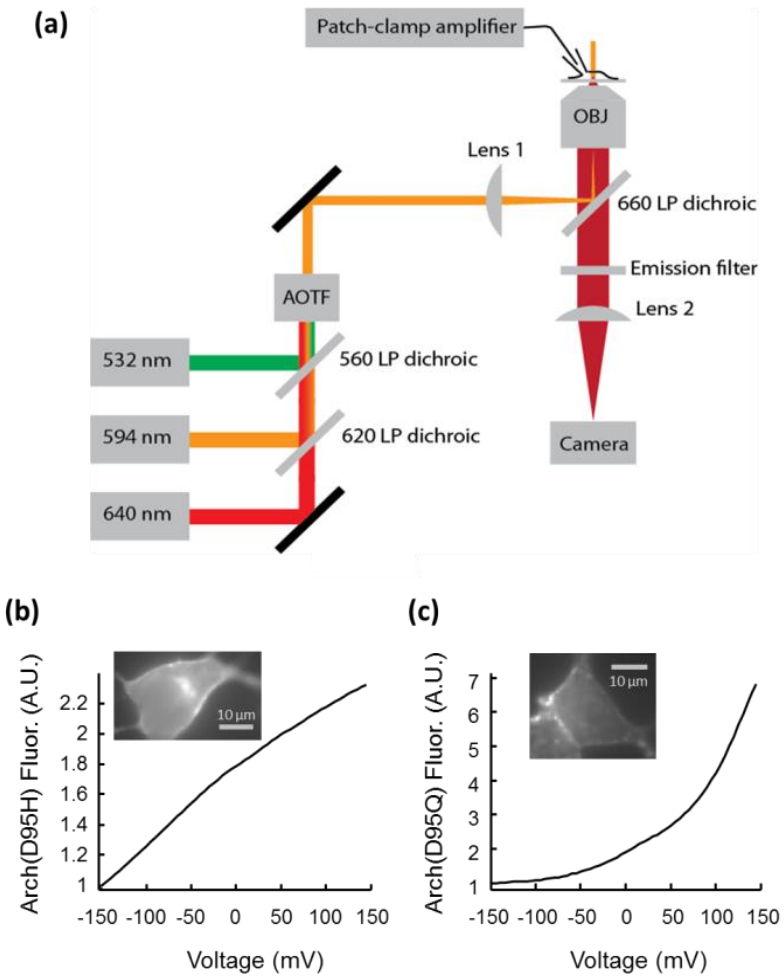

Figure 3-9. Testing Arch(D95X) mutants for voltage sensitivity. (a) Experimental setup. An acousto-optic tunable filter (AOTF) on the excitation path dynamically controlled the wavelength and intensity of illumination. A patch clamp amplifier provided control over the membrane potential. A camera recorded fluorescence. A shutter (not shown) after the AOTF blocked all light from reaching the sample during dark intervals. The AOTF, patch clamp apparatus, and camera were synchronized via custom software. (b) Voltage-sensitive fluorescence of Arch(D95H) expressed in a HEK cell under constant illumination at 640 nm. The fluorescence more than doubled between Vm = -150 mV and Vm = +150 mV. (c) Fluorescence of Arch(D95Q) increased 7-fold between -150 mV an d +150 mV, though most of the sensitivity was at positive voltages, above the physiological range.

3.2.3 Arch(D95H) and Arch(D95Q) store a photochemical record of membrane voltage

To test for Flash Memory behavior, we illuminated HEK cells expressing Arch(D95H) or Arch(D95Q) with the sequence (I_{write}, t_{dark}, I_{read}) while simultaneously

varying the membrane voltage under patch clamp control (Fig. 4). Each sequence (I_{write}, t_{dark}, I_{read}) was repeated twice, once with V_m fixed at -100 mV throughout, and once with V_m stepped from -100 mV to +100 mV during the write interval, and then returned to -100 mV for the dark and read intervals. Remarkably, the initial fluorescence during the read interval, F_i, depended on the voltage during the write interval, as required for a Flash Memory sensor. During the read pulse, the fluorescence gradually relaxed to a steady-state value, F_f, determined only by the voltage and illumination during the read pulse.

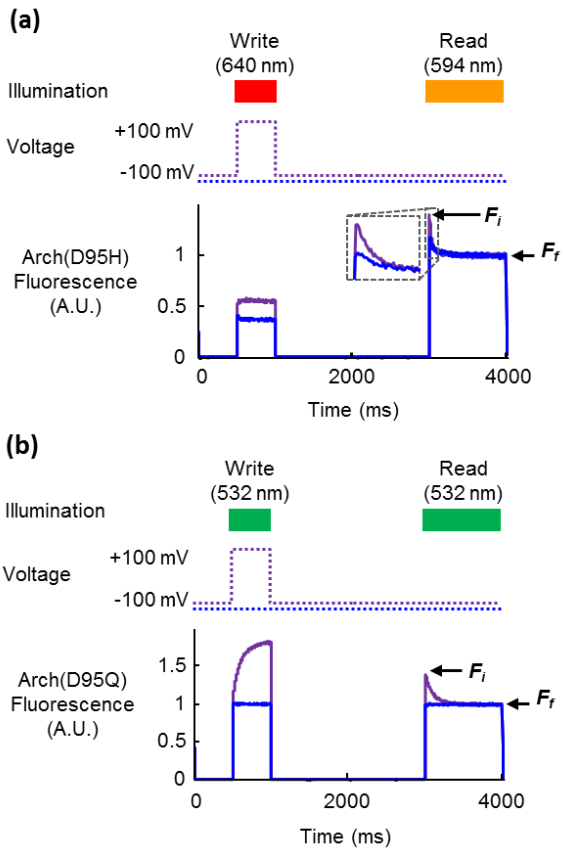

Figure 3-10. Observation of Flash Memory in Arch mutants Arch(D95H) and Arch(D95Q). (a) Fluorescence of Arch(D95H) at the start of the read pulse was greater for V_m = +100 mV during the write pulse (purple line) than for V_m = -100 mV during the write pulse (blue line). l_{write} = 640 nm, l_{read} = 594 nm. (b) Fluorescence of Arch(D95Q) at the start of the read pulse was greater for V_m = +100 mV during the write pulse (purple line) than for V_m = -100 mV during the write pulse (blue line). l_{write} = 532 nm, l_{read} = 532 nm.

We measured the extent of fluorescence relaxation during the read pulse by the dimensionless quantity

$$M = \frac{F_i - F_f}{F_f} \quad .$$

In a Flash Memory sensor, M should be high when V^{write} = +100 mV, and low when V^{write} = -100 mV. We quantified the Flash Memory effect by

$$\Delta M \equiv M\left(V^{write} = +100mV\right) - M\left(V^{write} = -100mV\right),$$

with V^{read} = -100 mV in both instances.

We tested Arch(D95H) and Arch(D95Q) with all combinations of λ_{write} and λ_{read} selected from 532 nm, 594 nm, and 640 nm, keeping t_{dark} fixed (Figs. 3-11, 3-12).

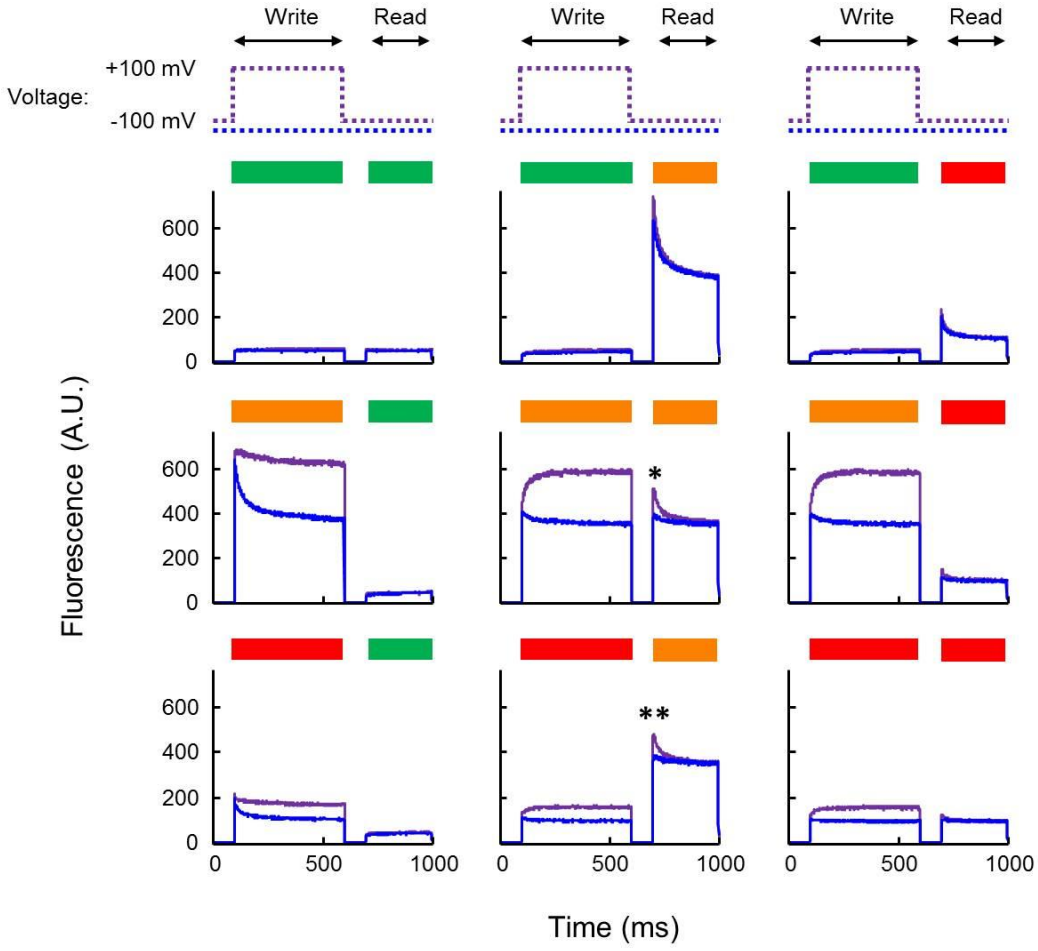

Figure 3-11. Flash Memory effect as a function of write and read wavelengths for Arch(D95H). The membrane potential of a HEK cell expressing Arch(D95H) was controlled via whole-cell patch clamp while the cell was illuminated with paired pulses with wavelength (λ_{write}, λ_{read}), where λ_{write} and λ_{read} were chosen from 532 nm, 594 nm, and 640 nm. During the write interval (t = 100 ms – 600 ms), the membrane voltage was V_{write} = +100 mV or -100 mV; voltage was held at -100 mV during the dark and read intervals. Initial fluorescence during the read interval was greater for V_{write} = +100 mV (purple trace) than for V_{write} = -100 mV (blue trace). The Flash Memory effect was largest when λ_{write} = 594 nm and λ_{read} = 594 nm (*), and when λ_{write} = 640 nm and λ_{read} = 594 nm (**).

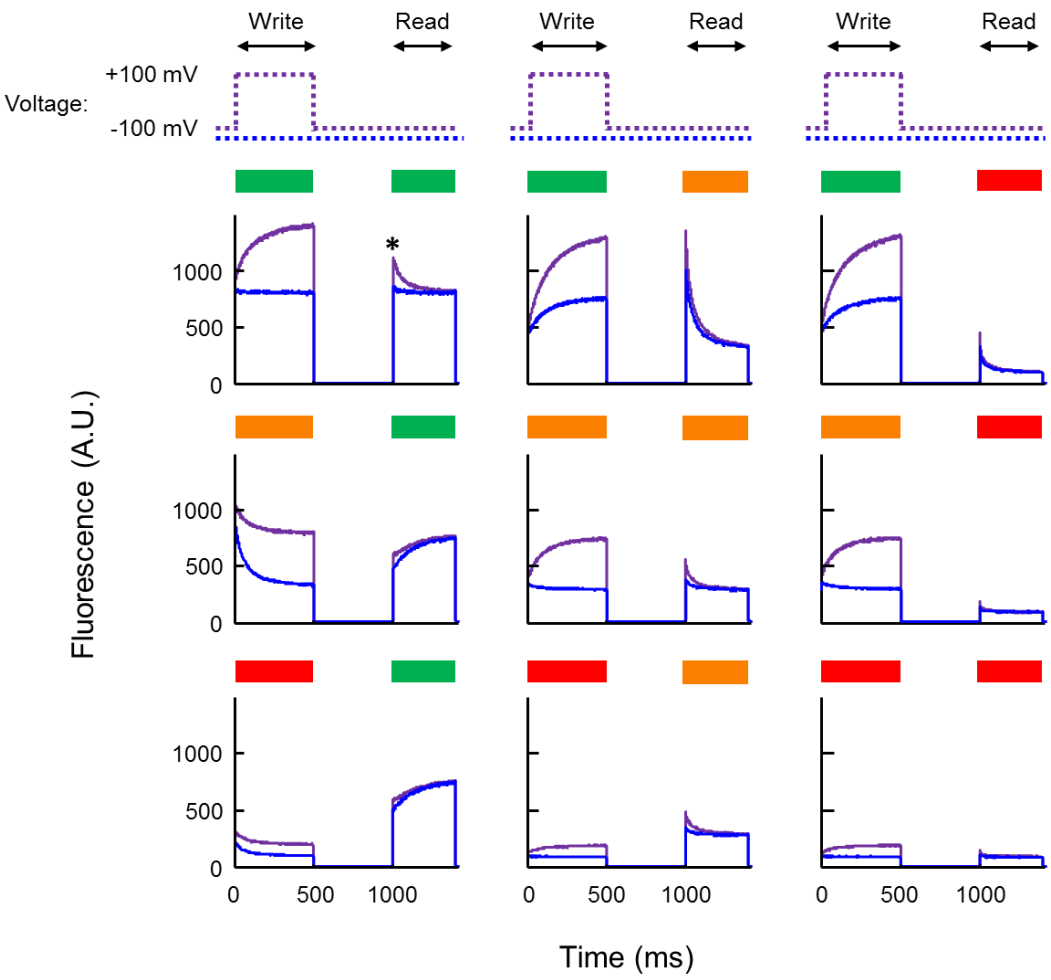

Figure 3-12. Flash Memory effect as a function of write and read wavelengths for Arch(D95Q). The membrane potential of a HEK cell expressing Arch(D95Q) was controlled via whole-cell patch clamp while the cell was illuminated with paired pulses with wavelength (λ_{write}, λ_{read}), where λ_{write} and λ_{read} were chosen from 532 nm, 594 nm, and 640 nm. During the write step (t = 0 ms – 500 ms), voltage was held at V_{write} = +100 mV or -100 mV; voltage was held at -100 mV during the dark and read intervals. Initial fluorescence during the read interval was greater for V_{write} = +100 mV (purple trace) than for V_{write} = -100 mV (blue trace). The Flash Memory effect was largest when λ_{write} = 532 nm and λ_{read} = 532 nm (*).

In Arch(D95H), the memory effect was maximized with λ_{write} = 640 nm and λ_{read} = 594 nm (Fig. 3-11). In Arch(D95Q), the memory effect was maximized with λ_{write} = 532 nm and λ_{read} = 532 nm (Fig. 3-12). We next asked whether a depolarizing voltage pulse during t_{dark} could overwrite a memory recorded during the write pulse. A 500 ms

voltage pulse to +100 mV in the middle of a 2 s dark interval had no effect on ΔM in either mutant (Fig. 3-13a,c). We then varied t_{dark} to measure the persistence of the memory (Fig. 3-13b,d). In both mutants the magnitude of ΔM remained constant up to t_{dark} = 2 minutes. Instabilities in the patch clamp connection prevented measurements at larger values of t_{dark}. In Arch(D95H) the memory effect was ΔM = 10%, while in Arch(D95Q) the memory effect was ΔM = 20%.

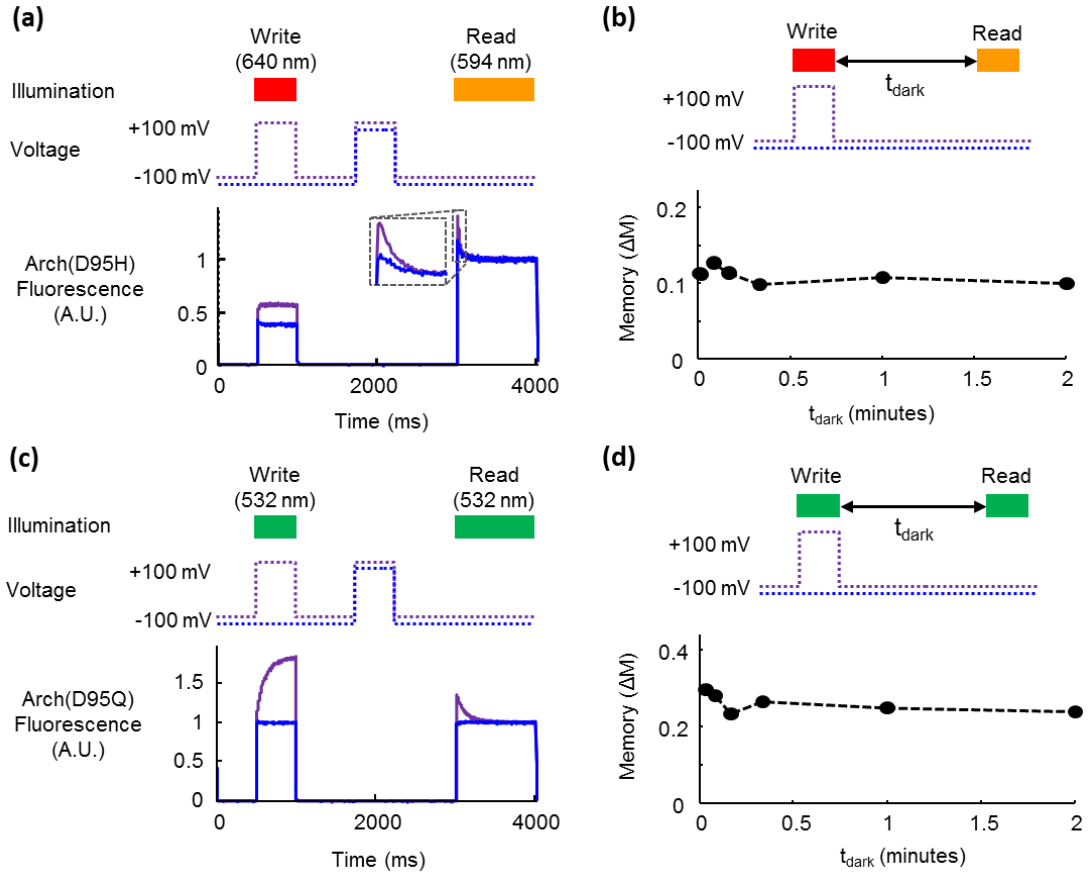

Figure 3-13. Characterization of Flash Memory in Arch mutants (a-b) Arch(D95H) and (c-d) Arch(D95Q). (a) Robustness of Flash Memory to voltage dynamics in the dark. A voltage pulse in the dark did not influence the fluorescence dynamics during the read interval. (b) Persistence of memory as a function of dark interval. The Flash Memory effect remained unchanged for up to t_{dark} = 2 min. In (a-b) l_{write} = 640 nm, l_{read} = 594 nm. (c-d) Same as (a-b) for Arch(D95Q). In (c-d) l_{write} = 532 nm, l_{read} = 532 nm.

We varied the timing of the voltage pulse in the dark and found no effect on ΔM, except for a small increase in ΔM for Arch(D95H) when the depolarizing voltage pulse ended < 20 ms prior to the read pulse (Fig. 3-14).

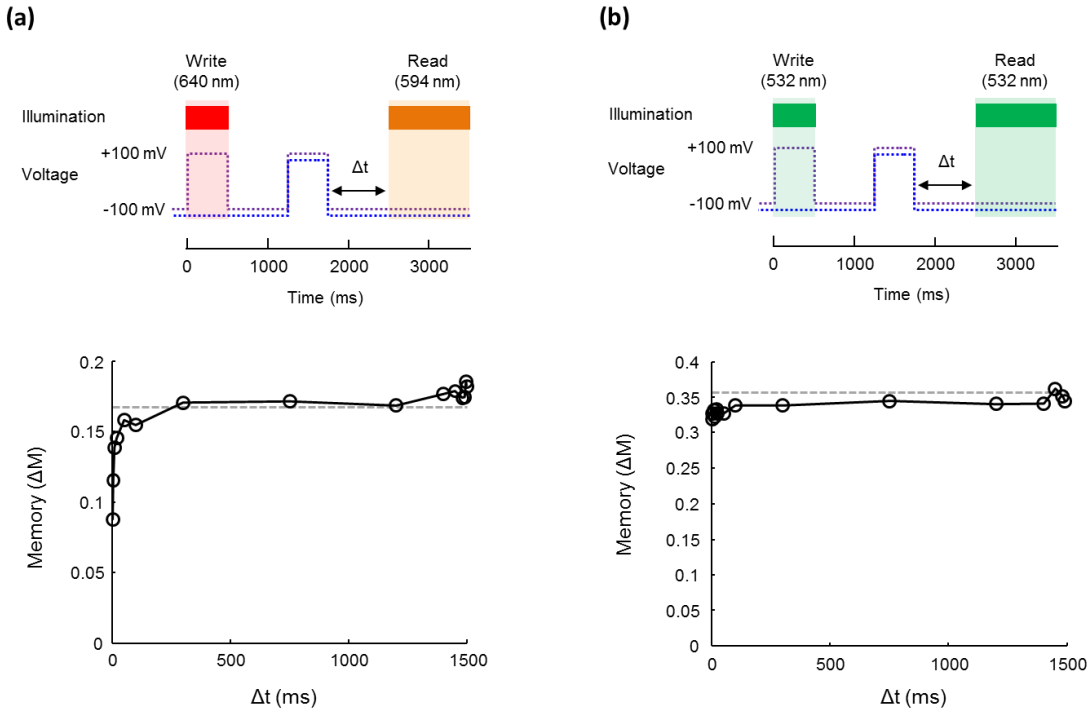

Figure 3-14. Effect of timing of a voltage pulse in the dark on the Flash Memory signal in (a) Arch(D95H) and (b) Arch(D95Q). The timing between the end of a voltage pulse in the dark and the read pulse, Δt, was varied as shown. The duration of the voltage pulse was fixed at 500 ms. The effect of the timing on the memory, ΔM, is plotted; in both cases, the gray dashed line shows ΔM when there was no voltage pulse in the dark.

3.2.4 Arch(D95H) responds faster than Arch(D95Q) to pulses of light or voltage

We varied the duration of the light pulse during the write interval to measure how fast a photochemical imprint of the voltage could be written. The voltage was held at +100 mV throughout the write interval (300 ms for Arch(D95H), and 800 ms for Arch(D95Q)), while the duration of the write illumination (t_{write}) was varied between 0 ms and 200 ms (Fig. 3-15). For Arch(D95H), the value of the memory, ΔM, increased

with t_{write}, following a double-exponential curve with write time constants of τ_{fast} = 0.14 ms and τ_{slow} = 12 ms; the majority of this response (57%) was determined by τ_{fast} (Fig. 3-15b). In contrast, for Arch(D95Q) writing took much longer: ΔM also increased with t_{write} and followed double-exponential kinetics, with time constants τ_{fast} = 5 ms and τ_{slow} = 180 ms; the majority of this response (92%) was determined by τ_{slow} (Fig. 3-15d).

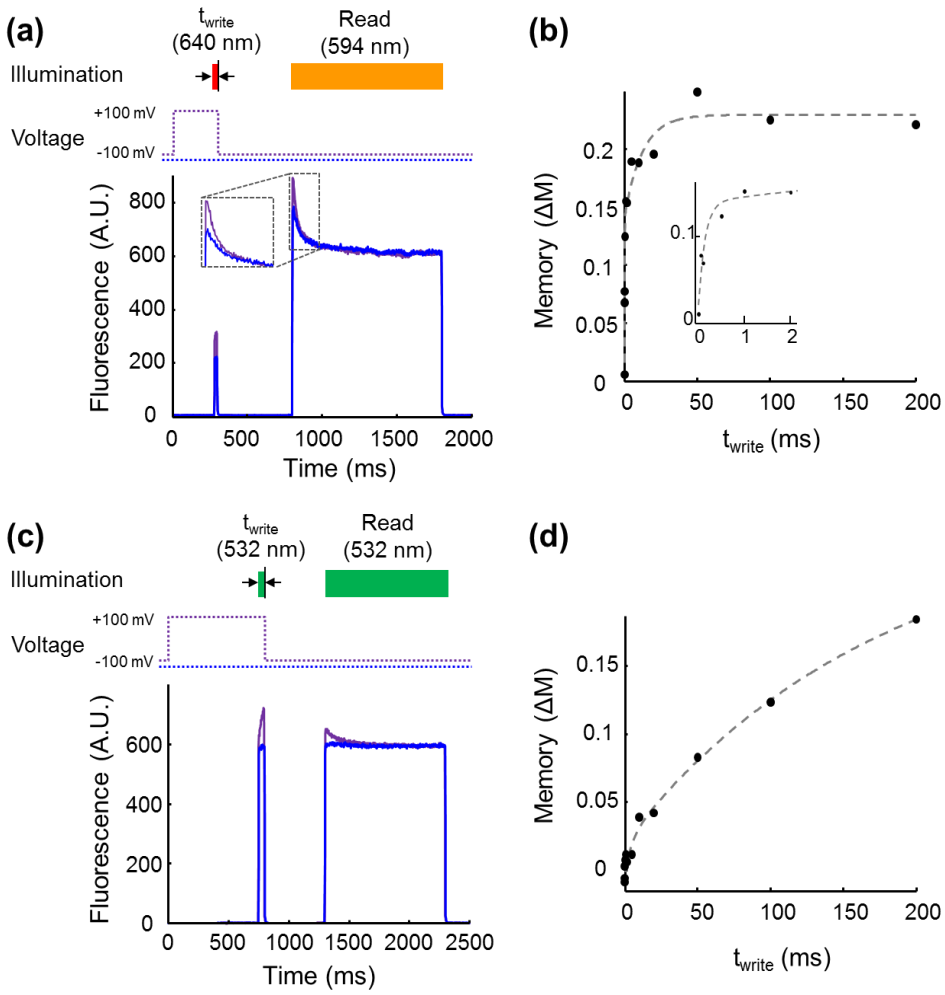

Figure 3-15. Kinetics of bright-state formation during the write pulse for (a,b) Arch(D95H) and (c,d) Arch(D95Q). Voltage was held at either +100 mV or -100 mV during the write interval, and at -100 mV during the dark and read intervals. The length of the write flash, t_{write}, was varied, keeping its end coincident with the step in voltage from +100 mV to -100 mV. Representative fluorescence traces are shown for (a) Arch(D95H) and (c) Arch(D95Q). (b,d) Plot of memory effect, ΔM, as a function of t_{write}. In Arch(D95H) the rise in memory was fit by a double exponential with τ_{fast} = 0.14 ms (57%) and τ_{slow} = 12 ms (43%); a write flash with t_{write} = 1 ms was sufficient to elicit more than half of the maximal response. (d) The dependence of ΔM on t_{write} in Arch(D95Q) was dominated by a slow component. A fit to a double exponential yielded τ_{fast} = 5 ms (8%) and τ_{slow} = 180 ms (92%).

We also performed the complementary experiment of changing the duration of the voltage pulse during the write interval while keeping the duration of the light pulse fixed at 1000 ms. The memory effect in Arch(D95H) saturated with a time constant for

the voltage pulse of 48 ms. For Arch(D95Q) the corresponding time constant was 146 ms (Figure 3-16).

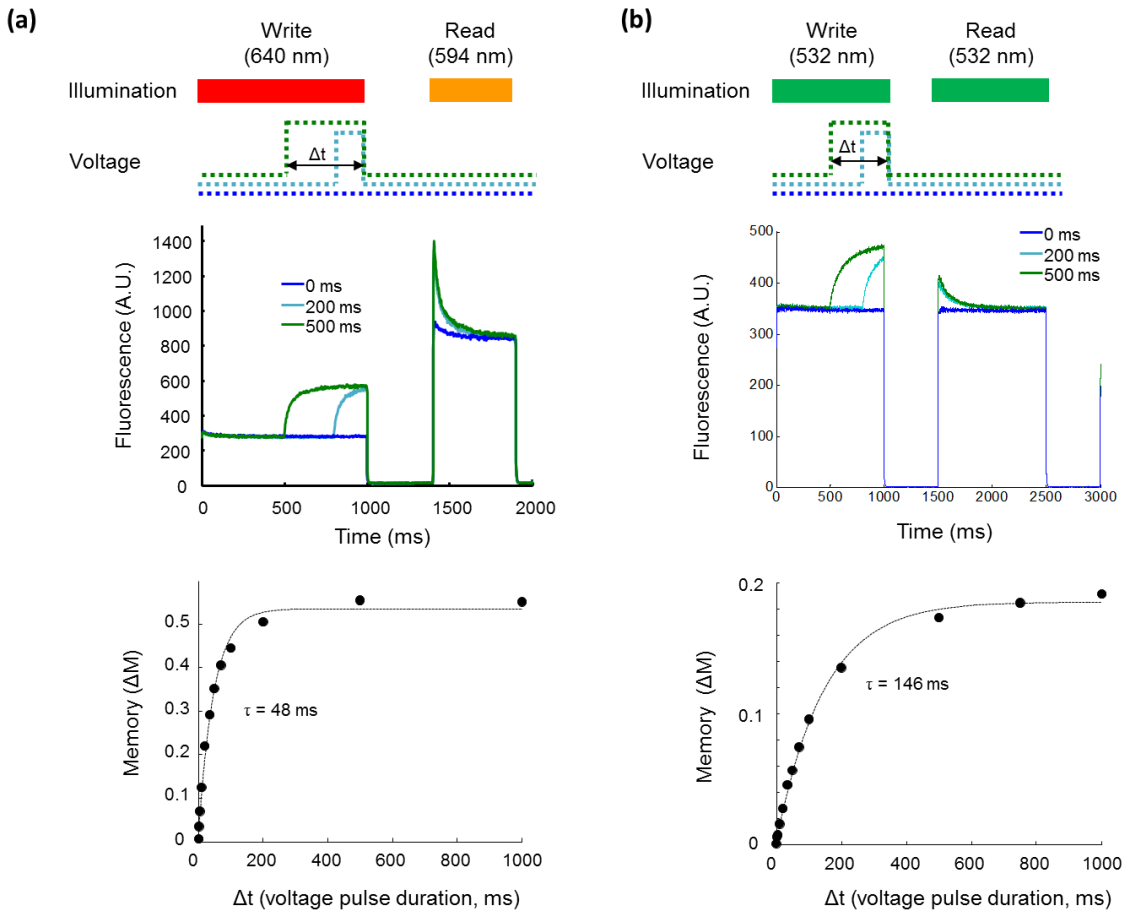

Figure 3-16. Varying duration of voltage pulse during write interval for (a) Arch(D95H) and (b) Arch(D95Q). Voltage was held at V_m = -100 mV except for a step to +100 mV of duration Δt and with an end coincident with the end of the write interval. The voltage pulse and the write flash ended at the same time (t = 1000 ms). In all cases, the write flash was 1 second long. The memory, ΔM, is plotted as a function of Δt; fits to a single-exponential are shown (τ = 48 ms for Arch(D95H); τ = 146 ms for Arch(D95Q)).

3.2.5 Arch(D95H) records a photochemical imprint of action potentials in a neuron

We tested whether Arch(D95H) could function as a Flash Memory sensor for recording neuronal action potentials. The sub-millisecond response of the protein to a flash of light at constant voltage (Fig. 3-15) indicated that the light-driven transition into the fluorescent state was fast compared to the duration of an action potential. However, the 48 ms response to a step in voltage under constant illumination (Fig. 3-16) implied that the voltage-dependent transition was slow: the rate of conformational change would low-pass filter the underlying voltage dynamics of the neuron. Despite this limitation, we tested whether Arch(D95H) could record an imprint of a single neuronal action potential.

We fused the C-terminus of Arch(D95H) to an endoplasmic reticulum export motif, followed by an eYFP expression marker and a trafficking sequence, as described in Ref. [65]. We cloned this construct into a lentiviral mammalian expression vector under the CaMKII promoter. Hippocampal neurons and glia were dissociated from postnatal day 0 (P0) rats and cultured on poly-D-lysine coated glass-bottomed dishes. At 4 days in vitro (div) 2 mM AraC was added to suppress further glial growth. We transfected the cells with Arch(D95H)-eYFP at 7 div using calcium phosphate, and we measured activity at 12 – 15 div. At the time of measurement, our construct had trafficked to the plasma membranes of the soma and processes, although considerable protein remained internalized in intracellular membranes.

Injection of current pulses (500 pA for 4 ms) via whole-cell patch clamp reliably induced single action potentials. We paired single action potentials with a 2 ms flash at

l_{write} = 594 nm (I = 200 W/cm^2). The flash was delivered either before (Δt < 0 ms), during (0 ms < Δt < 10 ms), or after (Δt > 10 ms) the action potential. After a dark interval of t_{dark} = 1 s, fluorescence was imaged with l_{read} = 594 nm. We used l_{write} = l_{read} = 594 nm, on the logic that in a neuroscience application it might be most convenient to use light of a single wavelength. Our signal-to-noise ratio in these measurements was not adequate to detect a signature of the action potential in the read fluorescence. We attributed this negative result to the slow response of Arch(D95H) to a step in voltage (t = 48 ms, Fig. 3-16).

We performed numerical simulations of the three-state model of Fig. 3-1b with different approaches to pairing flashes of light with action potentials (Fig. 3-17). These simulations showed that repeated trains of action potentials paired with brief flashes of light could build up population in the fluorescent state. In the simulations, the fluorescence during the read pulse reflected the temporal overlap of the voltage and light in the write pulses.

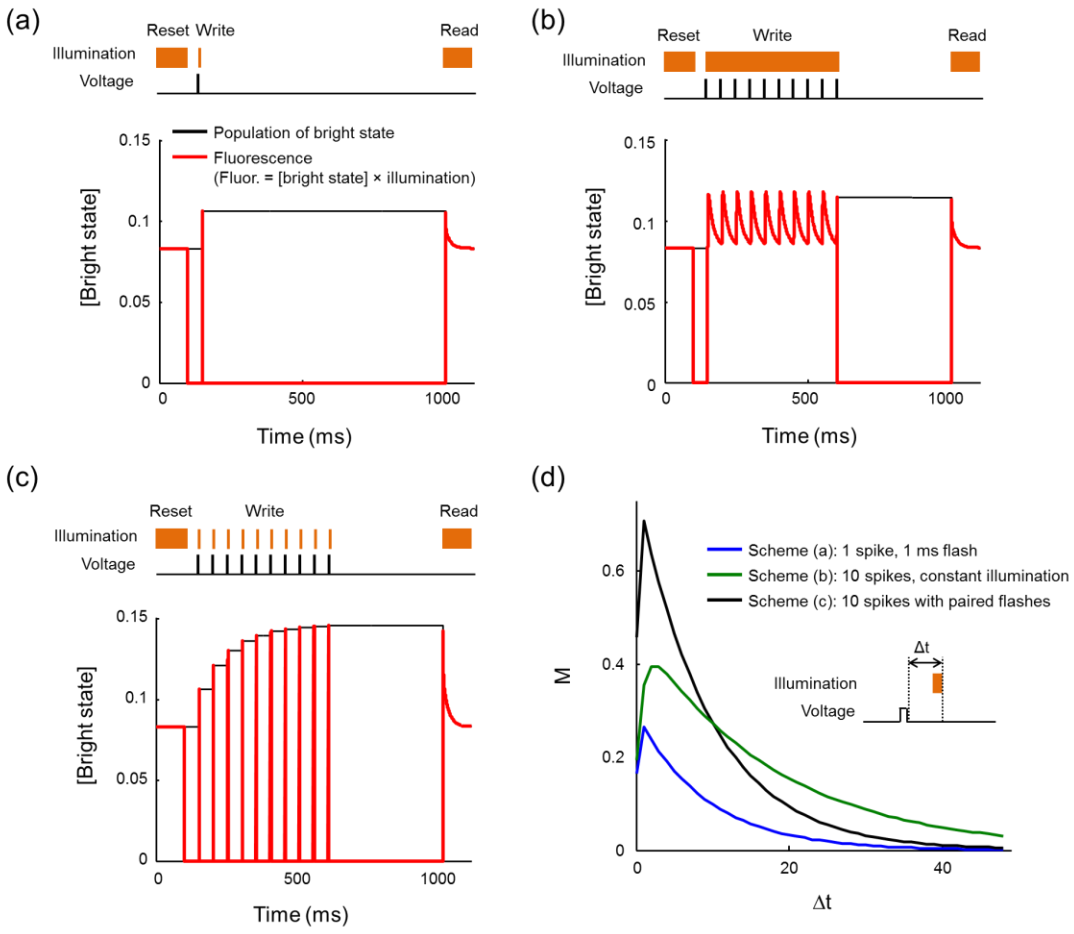

Figure 3-17. Simulation of illumination schemes to detect 1 ms electrical pulses (e.g. action potentials). Kinetic scheme shown in Fig. 3-2. Rate constants were chosen to simulate a slow response to a step in voltage and a fast response to a step in illumination, as observed for Arch(D95H). Parameter values given in section 3.4.7. (a-c) Each plot shows the population of the fluorescent state, *F*, (black) and the anticipated fluorescence (red). (a) Pairing a single 1 ms flash of light with a single 1 ms voltage pulse yields a small Flash Memory signal during the read interval. (b) Continuous illumination during ten 1 ms voltage pulses only modestly improves the signal. The influence of early voltage pulses is overwritten by later illumination during the write pulse. (c) Pairing ten voltage pulses with ten light flashes produced the largest Flash Memory signal. (d) Flash Memory effect as a function of the relative timing of the voltage and light pulses for the illumination protocols of (a-c).

We thus modified our illumination protocol to pair a train of 10 action potentials with a train of 10 light flashes. Action potentials were induced at 50 ms intervals, and each was paired with a 2 ms write flash at l_{write} = 594 nm (I = 200 W/cm^2). For each set of

10 action potentials, the write flashes were delivered either before ($\Delta t < 0$ ms), during (0 ms < Δt < 10 ms), or after (Δt > 10 ms) the corresponding action potentials. Fig. 3-18a shows the revised protocol. A plot of the memory effect, ΔM, during the read interval as a function of Δt during the write interval reproduced the underlying waveform of the action potential (Fig. 3-18b). This measurement demonstrates that Arch(D95H) can record a photochemical imprint of action potentials in a neuron, though an improved signal-to-noise ratio will be needed for application in neuroscience.

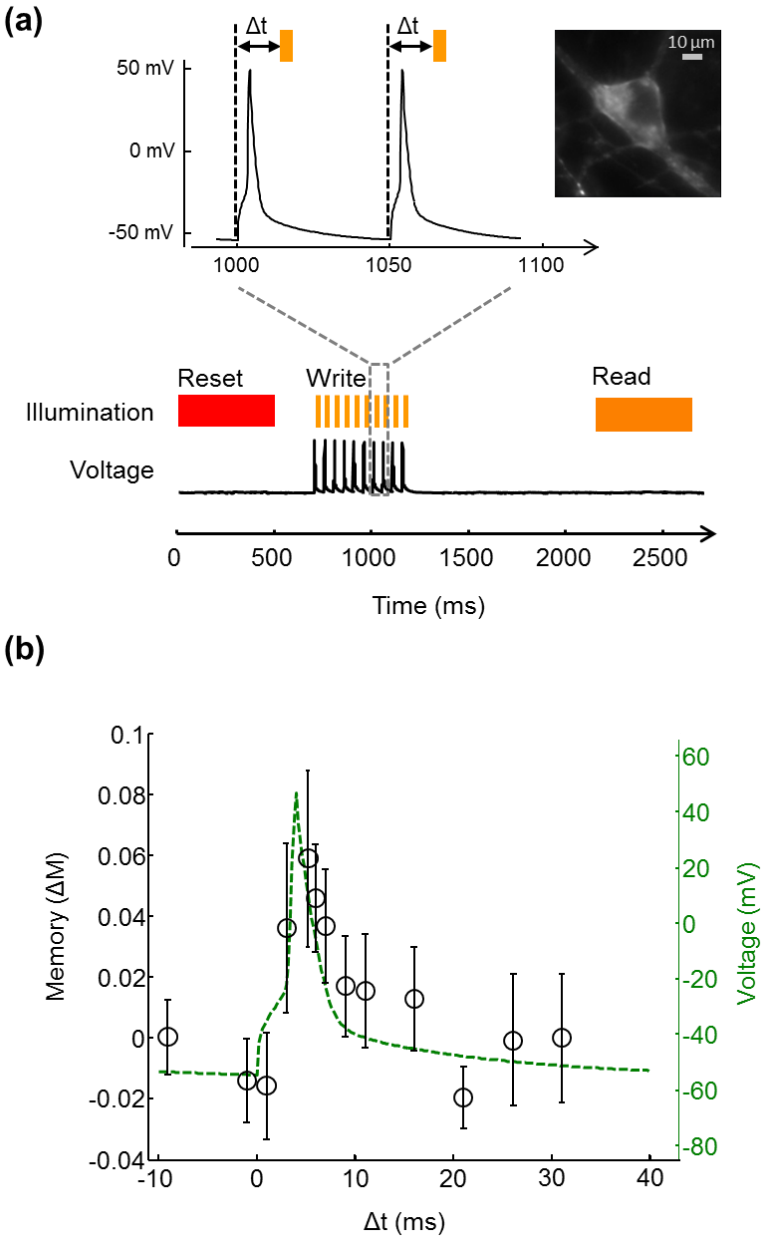

Figure 3-18. Photochemical imprinting of action potentials in a mammalian neuron expressing Arch(D95H). Paired action potentials and flashes of orange light led to increased formation of a fluorescent product only when the action potentials and orange flashes coincided in time. The fluorescent product was probed at t_{dark} = 1 s after the last action potential. (a) Illumination and voltage traces used in the experiment. (b) Memory effect, ΔM, recorded during the read interval (circles) overlaid on the electrical recording of the action potential acquired during the write interval (green). Each data point is the average of 5 trials of 10 action potentials. Error bars are the sample standard deviation.

3.2.6 Arch(D95Q) functions as a light-gated voltage integrator

Finally, we explored whether Arch(D95Q) could function as a light-gated voltage integrator. For a true integrator, the memory signal due to a voltage pulse should not depend on when in the write interval the pulse occurs. That is, population transferred to the bright state during an action potential must not revert to the dark state during a subsequent hyperpolarization. Thus there must be a negligible rate from bright state to the dark state during the write pulse (Figure 3-1c). After a search of wavelengths and intensities for the write pulse, we found that I_{write} = 1 W/cm^2 and l_{write} = 532 nm caused Arch(D95Q) to function as a light-gated voltage integrator (Figure 3-19).

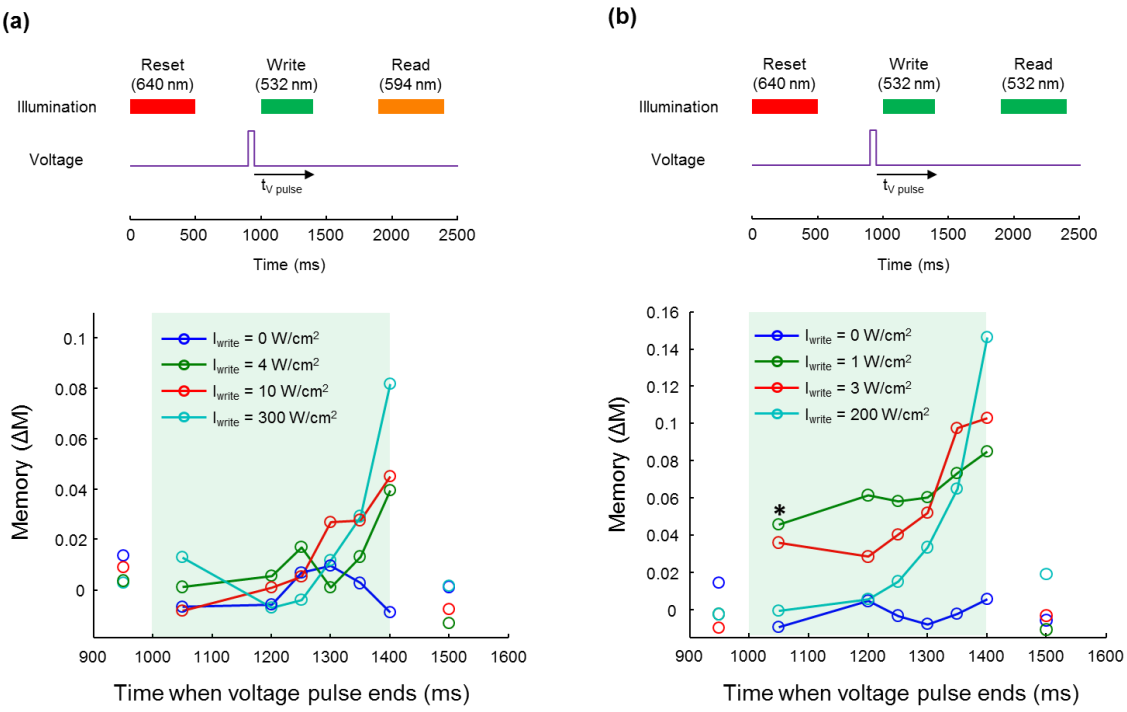

Figure 3-19. Erasure of an early voltage pulse during an extended write interval: effects of write pulse intensity. We studied the memory effect for a voltage pulse that ended before the end of the write pulse. Similar protocols were tested in (a) Arch(D95H) and (b) Arch(D95Q). The green bars denote the timing of the write pulse. The memory effect is plotted as a function of the timing of the end of the voltage pulse. In (a), the voltage pulse consisted of 25 spikes, 1 ms duration, spaced by 1 ms, from -100 mV to +100 mV; in (b), the voltage pulse was a 50 ms step from -100 mV to +100 mV. In an ideal sample and hold reporter, a voltage pulse that ends before the end of the write pulse should have no effect on the fluorescence during the read pulse. In an ideal light-gated integrator, a voltage pulse should have the same effect on the fluorescence during the read pulse regardless of when in the write pulse the voltage pulse occurs. The Flash Memory sensors Arch(D95H) and Arch(D95Q) showed intermediate behavior, with Arch(D95H) closer to a sample and hold sensor (a), and Arch(D95Q) closer to a light-gated integrator (b). In Arch(D95Q) the persistence of memories written early in the write interval depended on the illumination intensity during the write interval; the light-gated integrator effect was most pronounced when the write intensity is 1 W/cm^2 (*).

Arch(D95Q) did not traffic efficiently to the plasma membrane of neurons, so we tested its ability to count imposed voltage spikes in HEK cells instead, using the protocol shown in Figure 3-20a. A cell expressing Arch(D95Q) was held under voltage clamp conditions via a patch pipette, initially at a resting voltage of -100 mV. A reset pulse (I_{reset} = 635 nm, t_{reset} = 0.5 s, I_{reset} = 300 W/cm^2) drove the population into the non-

fluorescent state. During the write period, a dim green pulse (l_{write} = 532 nm, t_{write} = 0.4 s, I_{write} = 1 W/cm^2) was paired with a variable number of voltage spikes (-100 mV to +100 mV, 1 ms in duration). After a dark interval t_{dark} = 0.5 s, the fluorescence was probed by a green pulse (l_{read} = 532 nm, t_{read} = 0.5 s, I_{read} = 200 W/cm^2). We compared the value of the memory effect, *M*, in the presence of *n* voltage spikes to its value in the absence of voltage spikes.

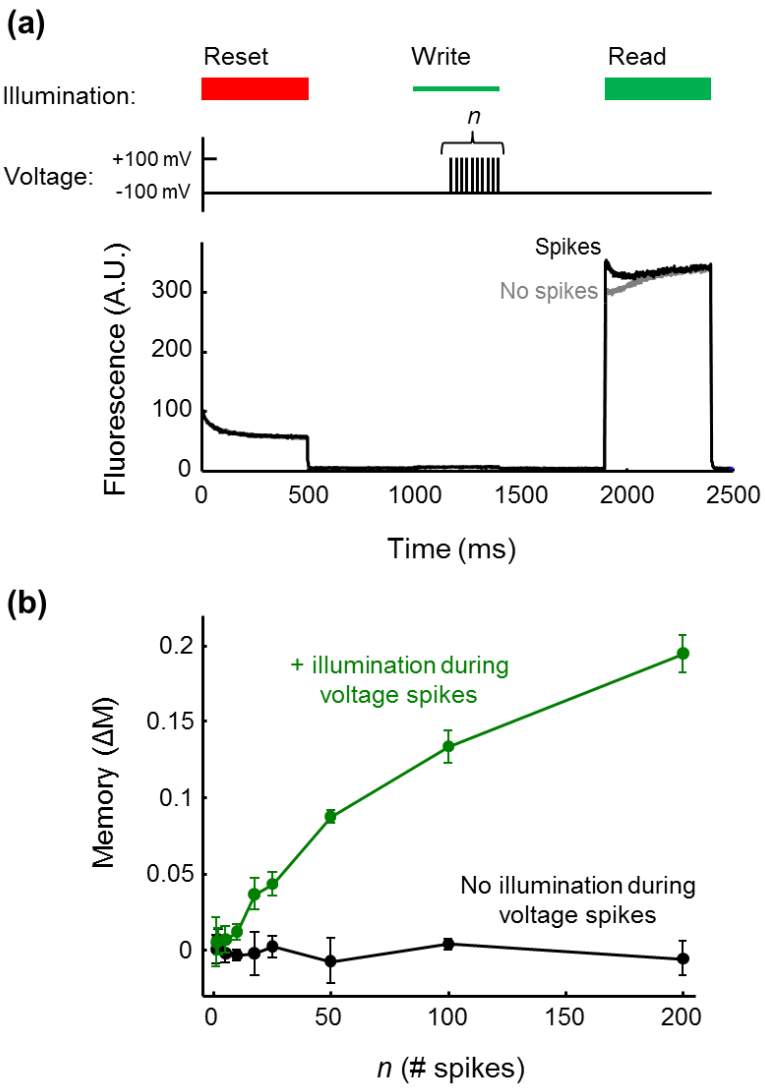

Figure 3-20. Photochemical counting of electrical spikes in a HEK cell expressing Arch(D95Q). (a) Top: sequence of illumination and voltage pulses to test the function of Arch(D95Q) as a light-gated voltage integrator. A red reset pulse initialized the protein in the non-fluorescent state. A series of *n* voltage pulses (-100 mV to +100 mV, 1 ms) was paired with dim green illumination (1 W/cm^2) to produce fluorescent product at a voltage- and light-dependent rate. After a delay of t_{dark} = 0.5 s, the fluorescence was probed by a green read pulse (200 W/cm^2). Bottom: representative fluorescence traces for *n* = 100 spikes. (b) Memory effect, ΔM, probed in the read interval as a function of number of spikes in the write interval. In the presence of the write pulse, the memory reported the number of spikes (green). When the write pulse was omitted, spikes did not induce a memory effect (black). Error bars are the sample standard deviation calculated from six repetitions of the experimental pulse sequence.

Figure 3-20a shows representative raw fluorescence traces with and without n = 100 voltage spikes. Figure 3-20b shows that the memory effect (ΔM) increased with the number of voltage spikes during the write interval. Although the voltage spikes in this experiment were not action potentials, this preliminary result shows the feasibility of using an Arch-based sensor to count voltage spikes in a light-gated manner.

3.2.7 Mechanistic analysis of Flash Memory sensors

What is the molecular basis of Flash Memory in Archaerhodopsin mutants? While a complete characterization of the photocycles of Arch(D95H) and D95Q is beyond the scope of this paper, here we show that a simple three-state model reproduces the main qualitative features of the data. Varying the illumination parameters can tune the behavior of the model continuously between sample and hold and light-gated integrator behavior.

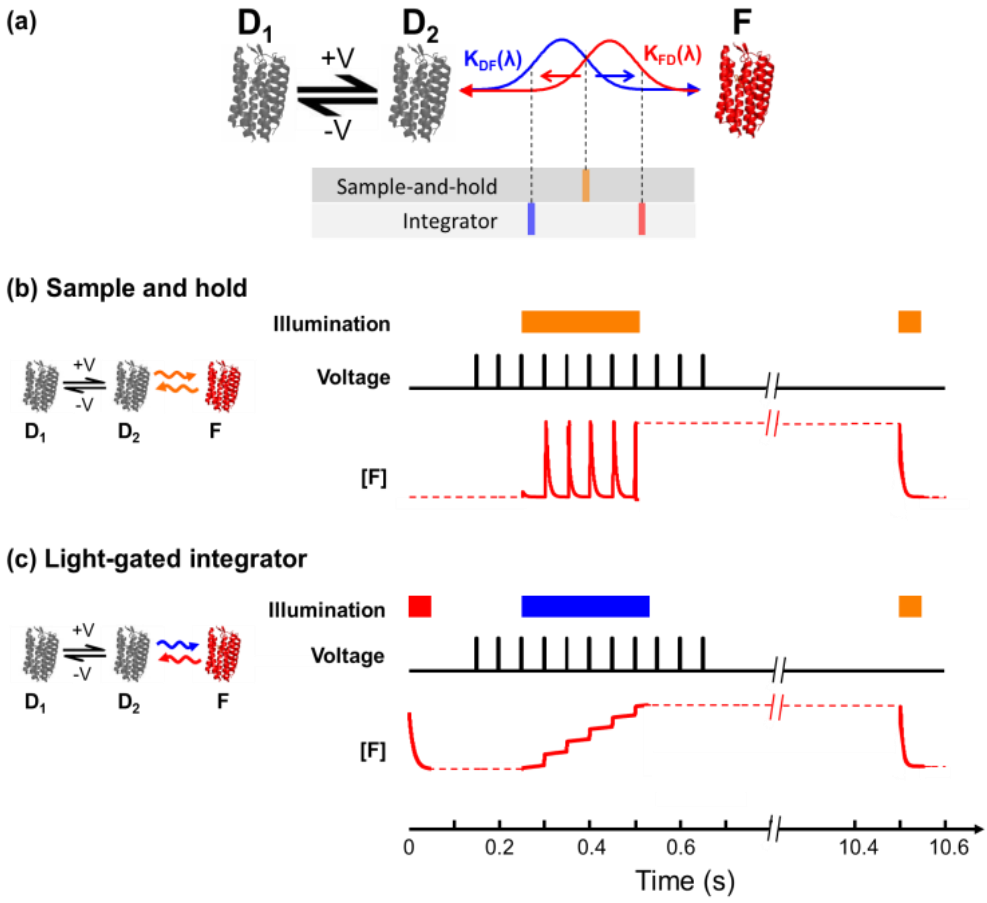

Figure 3-21. Numerical simulation of three-state kinetic model of Flash Memory effect in Arch mutants. (a) Reaction scheme in which illumination wavelength tunes the $D_2 \rightleftharpoons F$ equilibrium. (b) In a sample-and-hold sensor, the population of F follows the voltage-dependent $D_1 \rightleftharpoons D_2$ equilibrium until the end of the write pulse. The solid red trace on the right is a numerical simulation of the population in F. (c) In a light-gated integrator, blue light converts population from D_2 to F, but does not allow the reverse process. Population in F accumulates in a voltage-dependent manner during the write pulse.

Figure 3-21 shows the model and Figs. 3-21b,c show numerical simulation results. A voltage-dependent equilibrium exists between two non-fluorescent states, D_1 and D_2. The fluorescent state, F, is connected to D_2 by a light-driven process (presumably retinal isomerization). The action spectra of the transitions into and out of state F are different; blue light drives the transition into the fluorescent state ($D_2 \rightarrow F$),

red light drives the reverse reaction ($F \rightarrow D_2$) and orange light drives both reactions. Red light also excites fluorescence of F.

To use the protein as a sample and hold sensor (Fig. 3-21b), one illuminates with a wavelength l_{write} that simultaneously drives both the $D_2 \rightarrow F$ and $F \rightarrow D_2$ transitions. During the write interval the ratio of [F] to [D_2] is determined by l_{write} and the forward and reverse action spectra. Voltage sets the ratio of [D_1] to [D_2], and thereby sets the population of F. The moment the light turns off, the population in F is trapped, decoupled from voltage-dependent dynamics in the D manifold. During the read pulse, light at l_{read} excites fluorescence from F, but at the same time re-establishes equilibrium between F and the D manifold.

The same model can function as a light-gated integrator. The reset pulse is given at a wavelength l_{reset} sufficiently far red that it drives $F \rightarrow D_2$, but not $D_2 \rightarrow F$, thereby initializing the population in the dark D manifold. The write pulse is chosen with l_{write} sufficiently blue that it can drive $D_2 \rightarrow F$, but not $F \rightarrow D_2$. Thus, when the voltage is high enough to populate D_2 and the write pulse is on, molecules take a one-way trip from D_2 to F. This model predicts that by tuning the intensity and wavelength of the write pulse, one can adjust the dynamic range of the integrator. A large k_{DF} increases sensitivity to single spikes but causes the integrator to saturate at a smaller number of spikes, while a small k_{DF} has the opposite effect. Our simple analysis suggests that additional control over the state of the system could be obtained by illuminating with two wavelengths simultaneously during the write interval. By choosing a blue and a red wavelength, one could independently control the rates into and out of the fluorescent state.

While this model is sufficient to explain the main features we observed in Flash Memory proteins, these molecules likely have more than three significant states. If one were to map the simple model of Fig. 3-21a onto a canonical proton pump photocycle, the dark manifold would likely correspond to the set of states that interconvert in a voltage-dependent way in the main photocycle (M and N intermediates), and the state F would correspond to the off-pathway photogenerated fluorescent state called Q in Ref. [2].

3.3 Discussion

We have introduced the concept of Flash Memory as a technique to record light-gated photochemical imprints of membrane voltage. Two mutants of the fluorescent voltage indicator Archaerhodopsin-3 (Arch) can be used as Flash Memory sensors, albeit with small signal amplitudes that limit immediate practical utility. Arch(D95H) functioned as a light-gated sample and hold. This protein could store a photochemical record of action potentials in a rat neuron. Arch(D95Q) functioned as a light-gated voltage integrator. This protein could report the number of electrical spikes that had occurred in a HEK cell during a user-selected recording epoch.

Many aspects of Flash Memory sensors need further improvement. These include: plasma membrane trafficking in neurons, overall brightness, and contrast between the “high-voltage” and “low-voltage” states. Ideally, the protein would switch fully within the physiological range of -70 to +30 mV. For readouts that involve fixing

and slicing the tissue, one must also test whether the memory effect is robust to fixation procedures, and whether it lasts for days, not just minutes.

In view of the very limited search for Flash Memory proteins undertaken here, we are optimistic that superior performance may be found among other rhodopsin-like proteins. One should not restrict the search to mutants of Arch. Among the vast number of natively bistable rhodopsin-like proteins [60], there may be some that are fluorescent and voltage sensitive. A more detailed structural analysis of Arch(D95H) and D95Q would help guide this search. In particular, it may be helpful to identify the isomerization state of the retinal in the fluorescent state, as well as the voltage-induced shifts in structure and protonation.

Improved Flash Memory proteins could be used *in vivo* in two modalities. If one is content to image the optically accessible region of the brain, then the readout could be performed in the live animal. This approach has the advantage that the protein can be reset and the measurement repeated multiple times, thereby averaging out uncorrelated baseline activity. If one wishes to image a larger or deeper region of the brain than is optically accessible, then one could fix the brain and either clarify or slice the tissue. This procedure is obviously terminal.

While we have focused on fluorescence as a readout, other modalities may also be feasible. Particularly attractive are multiphoton techniques such as two-photon fluorescence and stimulated Raman scattering, as these techniques have greater depth penetration than the visible light used in one-photon imaging. 2-photon fluorescence provides a very localized excitation volume, avoiding the problem of unintentional

resetting of proteins from scattered imaging illumination. Non-resonant Raman or infrared absorption techniques may be able to determine the isomerization state of the retinal without inducing changes in this state. These techniques could integrate signal for longer times than fluorescent readouts, thereby increasing sensitivity.

There are several ways in which one might use Flash Memory proteins in neuroscience experiments. Sample and hold proteins are probably most useful when the neural activity is linked to a repeatable stimulus, e.g. in a sensory processing experiment. One could then repeat the stimulus multiple times, interleaved with trials without the stimulus. By varying the interval between stimulus and "write" flash, one may determine the precise sequence in which the stimulus activates neurons. Light-gated integrators may be more useful in identifying brain regions that show enhanced activity during spontaneously generated behaviors. One could deliver a flash of light to the brain upon observing the desired behavior, and then fix and image the brain region of interest.

3.4 Materials and Methods

3.4.1 Combined high-speed fluorescence and patch clamp apparatus

Fluorescence imaging of Arch mutants in HEK-293T cells and neuronal cells was performed on a homebuilt, inverted epifluorescence microscope. Beams from four continuous wave (CW) lasers (637 nm 100 mW Coherent OBIS; 594 nm 100 mW Cobolt Mambo; 532 nm 50 mW Coherent Compass 215M; 488 nm 50 mW Omicron PhoxX) were combined using dichroic mirrors and then spectrally selected using an acousto-

optic tunable filter (AOTF; Gooch and Housego 48058). A shutter was placed downstream of the AOTF to block all light from reaching the sample during dark intervals. Illumination was focused onto the back focal plane of the objective (Olympus, 1-U2B616 60× oil, NA 1.45) via a 650 nm long-pass dichroic mirror. The sample was illuminated in epifluorescence mode and emission was collected by the same objective and passed through the dichroic mirror. Fluorescence was filtered with a 660 – 760 nm bandpass filter (Semrock) and collected at a frame rate between 1000 and 1500 Hz on a cooled EMCCD camera (Andor iXon X3 DU-860, 128 x 128 pixels).

Patch clamp experiments were performed at room temperature (25 °C) using an Axopatch 200B amplifier (Molecular Devices). Micropipettes were pulled from borosilicate glass capillary tubes (World Precision Instruments, 1.5 mm OD, 0.84 mm ID) using a glass micropipette puller (Sutter Instrument, P-1000) to a tip resistance of 5-10 MΩ and filled with intracellular buffer (125 mM potassium gluconate, 8 mM NaCl, 0.6 mM $MgCl_2$, 0.1 mM $CaCl_2$, 1 mM EGTA, 10 mM HEPES, 4 mM Mg-ATP, and 0.4 mM Na-GTP at pH 7.3; adjusted to 295 mOsm with sucrose). These micropipettes were positioned using a micromanipulator (Sutter Instrument, MP-285). The extracellular solution for all recordings was Tyrode's buffer (125 mM NaCl, 2 mM KCl, 3 mM $CaCl_2$, 1 mM $MgCl_2$, 10 mM HEPES, and 30 mM glucose at pH 7.3; adjusted to 305–310 mOsm with sucrose). All patch-clamp data in HEK cells were acquired in voltage-clamp mode; all patch-clamp data in neurons were acquired in current-clamp mode. Voltage and current waveforms were generated using custom software written in LabView and sent via a National Instruments DAQ (PCIe-6323) to the Axopatch 200B.

In each combined fluorescence and patch clamp experiment, we illuminated the sample with a series of laser pulses while varying the voltage or current across the cell membrane. The experimental sequence was repeated multiple times to test whether the observed effects were due to photobleaching. The data consisted of time-series of fluorescence images. Fluorescence images were analyzed in MATLAB (Mathworks). For cells in which membrane trafficking of the protein was incomplete, a region of interest comprising the cell membrane was selected prior to data analysis.

3.4.2 Molecular biology

A library of Arch(D95X) mutants was generated by performing saturation mutagenesis of residue Asp95 in Archaerhodopsin-3 in the pET-28b vector as described in Part I (Section 1.1.2).

To express mutants in HEK-293T cells, the Arch(D95X) library was cloned (using Gibson Assembly, New England Biolabs) into a lentiviral mammalian expression vector containing a ubiquitin promoter (Addgene plasmid 22051 cut with the restriction enzymes BamHI and AgeI [9]). The library consisted of Arch(D95X) fused to C-terminal eGFP. These constructs were used for all experiments in HEK-293T cells.

For neuronal expression, the (D95H) point mutation was made on Addgene plasmid 35514 (pLenti-CaMKIIa-eArch 3.0-eYFP). In this vector, Arch is fused to eYFP with the trafficking motifs TS (Golgi trafficking sequence) and ER2 (endoplasmic reticulum export motif) from Kir2.1 flanking the eYFP; this vector was previously found to enhance membrane trafficking of Arch in neurons [66]. The primers used for mutagenesis were:

D95H_FWD:

5’-CAGGTACGCCCACTGGCTGTTTACCACCCCACTTCTG

and D95H_REV:

5’-GTAAACAGCCAGTGGGCGTACCTGGCATAATAGATATCCAACATTTCG.

The final construct, Arch(D95H) 3.0, consisted of Arch(D95H)-TS-eYFP-ER2 under the CamKII promoter.

3.4.3 Testing for photoswitching in E. coli

E. coli (strain BL21) were transfected with Arch(D95X) in the pET-28b vector under the T7 promoter and grown in LB containing 100 μg/mL kanamycin in a shaking incubator at 37 °C. At an OD600 of 0.5, protein expression was induced with 0.5 mM IPTG, and 5 μM all-trans retinal was added from a concentrated stock in DMSO. Cells were then returned to the incubator and grown for another four hours. Carbonyl cyanide m-chlorophenyl hydrazine (CCCP, 50 μg/mL) was added to neutralize membrane potential, and the cells were spread on a glass coverslip for imaging. White light emission from a supercontinuum laser (Fianium SC-450-6) was spectrally selected using an AOTF (Crystal Technologies). AOTF powers were adjusted to maintain a wavelength-independent intensity at the sample of 10 W/cm^2. Emission was collected on a photomultiplier tube (PMT; Thorlabs PMM02 with multialkali (S20) photocathode). Minor discrepancies between the temporal dynamics of transients observed in Figure S1 and those observed in our other data are attributed to either differences in illumination intensity, or to low-intensity (< 1 mW/cm^2) white light from the super-continuum laser leaking through the AOTF during the dark intervals.

3.4.4 Imprinting photochemical images in Arch(D95H) in E. coli

E. coli expressing Arch(D95H) were prepared as described above. Light from a 488 nm laser (50 mW, Omicron PhoxX) was reflected off a digital micromirror device (DMD, Texas Instruments, Lightcrafter) in the excitation path. The DMD chip was re-imaged onto the focal plane of the microscope. Light from a 640 nm laser was expanded using a telephoto zoom lens (Sigma 18-200mm f/3.5-6.3 II DC) and then combined with the spatially patterned blue beam via a dichroic mirror. To generate the images in Figure 3-7, the initial fluorescence of each pixel upon 640 nm illumination was normalized to the steady-state fluorescence of that pixel to account for the inhomogeneous distribution of E. coli in the field of view.

3.4.5 HEK-293T cell culture

HEK293T cells were grown in DMEM supplemented with 10% FBS and penicillin/streptomycin in a 37 °C incubator under 5% CO2. Cells were grown to 50-70% confluency in 3.5 cm dishes. 48 hours prior to experimentation, cells were transfected using Transit-293 (Mirus) with either Arch(D95H)-eGFP or Arch(D95Q)-eGFP in a mammalian expression vector under the ubiquitin promoter (see “Molecular Biology” above). These cells were trypsinized and re-plated at a density of ~5,000-10,000 cells/cm^2 on matrigel-coated coverglass bottom dishes (P35G-1.5-14-C, MatTek) 12 – 24 hours before experimentation. Although there is some retinal present in FBS, we added all-trans retinal (5 µM) to each dish 1 - 2 hours prior to imaging to ensure saturation of the retinal binding sites in Arch.

3.4.6 Neuronal cell culture

Sprague Dawley rats were obtained from Taconic Labs. Postnatal day 0 (P0) pups were euthanized and hippocampi were dissected following the procedure in Ref. [67]. Briefly, isolated hippocampi were digested with papain and homogenized in Hank's Balanced Salt Solution (HBSS) containing MgCl2 and kyneurinic acid to prevent excitotoxicity. Cells were plated on glass-bottomed dishes (P35G-1.5-14-C, MatTek) coated with 20 µg/mL poly-D-lysine, and cultured in plating medium [MEM (Life Technologies) containing 10% fetal bovine serum, 0.5% glucose, 10 mM HEPES, 2 mM Glutamax (Life Technologies), 100 mg/L transferrin, insulin, and B27]. After 60 hours, the media was replaced with NbActiv4 (Brainbits, Nb4-500). At 4 days in vitro (div) 2 µM AraC was added to suppress further glial growth. At 7 div, neurons were transfected using calcium phosphate (Clontech, cat. #631312). Each 3.5 cm dish was transfected with 2000 ng of DNA; for gentler transfection, 200 ng of the Arch(D95H)-3.0 vector (see "Molecular Biology" above) was diluted with 1800 ng of "junk" DNA (pUC19).

All experimental protocols involving use of animals were approved by the Harvard Institutional Animal Care and Use Committee (IACUC).

3.4.7 Numerical simulation of three-state model

Numerical simulation of a three-state model of Flash Memory was implemented in MATLAB (Mathworks). A system of ordinary differential equations was defined with states D1, D2, and F, and rates kD1→D2, kD2→D1, kD2→F, and kF→D2 following:

$$\frac{d[D1]}{dt} = k_{D2\rightarrow D1}[D2] - k_{D1\rightarrow D2}[D1]$$

$$\frac{d[D2]}{dt} = k_{D1\to D2}[D1] - k_{D2\to D1}[D2] + k_{F\to D2}[F] - k_{D2\to F}[D2]$$

$$\frac{d[F]}{dt} = k_{D2\to F}[D2] - k_{F\to D2}[F]$$

Rate constants kD1→D2 and kD2→D1 were made to depend on voltage but not illumination, while rate constants kD2→F and kF→D2 were made to depend on illumination wavelength and intensity, but not voltage.

Rate constants were chosen to illustrate the qualitative behaviors of this three-state model. Table 3-1 gives reaction time constants (inverse of the rate constants) for the conditions found in the illumination scheme of Figure 3-17. Table 3-2 gives reaction time constants for the conditions found in the illumination scheme of Figure 3-21.

$D_1 \rightleftharpoons D_2$

	High voltage	Low voltage
$k_{D1\to D2}$	10 ms	100 ms
$k_{D2\to D1}$	100 ms	10 ms

$D_2 \rightleftharpoons F$

	λ = 594 nm (orange)	No illumination
$k_{D2\to F}$	1 ms	1000 s
$k_{F\to D2}$	1 ms	1000 s

Table 3-1. Parameters for Fig. 3-17

$D_1 \rightleftharpoons D_2$

	High voltage	Low voltage
$k_{D1\to D2}$	0.1 ms	10 ms
$k_{D2\to D1}$	10 ms	0.1 ms

$D_2 \rightleftharpoons F$

	λ = 488 nm (blue)	λ = 594 nm (orange)	λ = 640 nm (red)	No illumination
$k_{D2\to F}$	50 ms	5 ms	1000 s	1000 s
$k_{F\to D2}$	1000 s	5 ms	10 ms	1000 s

Table 3-2. Parameters for Fig. 3-21

3.5 Future directions

3.5.1 Screening Arch mutants for optical bistability

As we think about ways to take Flash Memory *in vivo*, one of our main goals is to engineer a sensor that is brighter and more sensitive than either Arch(D95H) or Arch(D95Q). There are numerous ways to approach this task, many of which were discussed in Section 3.3. One way to identify new candidate Flash Memory sensors is to screen Arch mutants for optical bistability. If light can be used to drive the protein into a state that is fluorescent and stable in the dark, then perhaps voltage can influence the rate of this process. We began to look at bistability in an Arch(D95X, D106X) library, and some of the preliminary results from these explorations are shown in Figure 3-22.

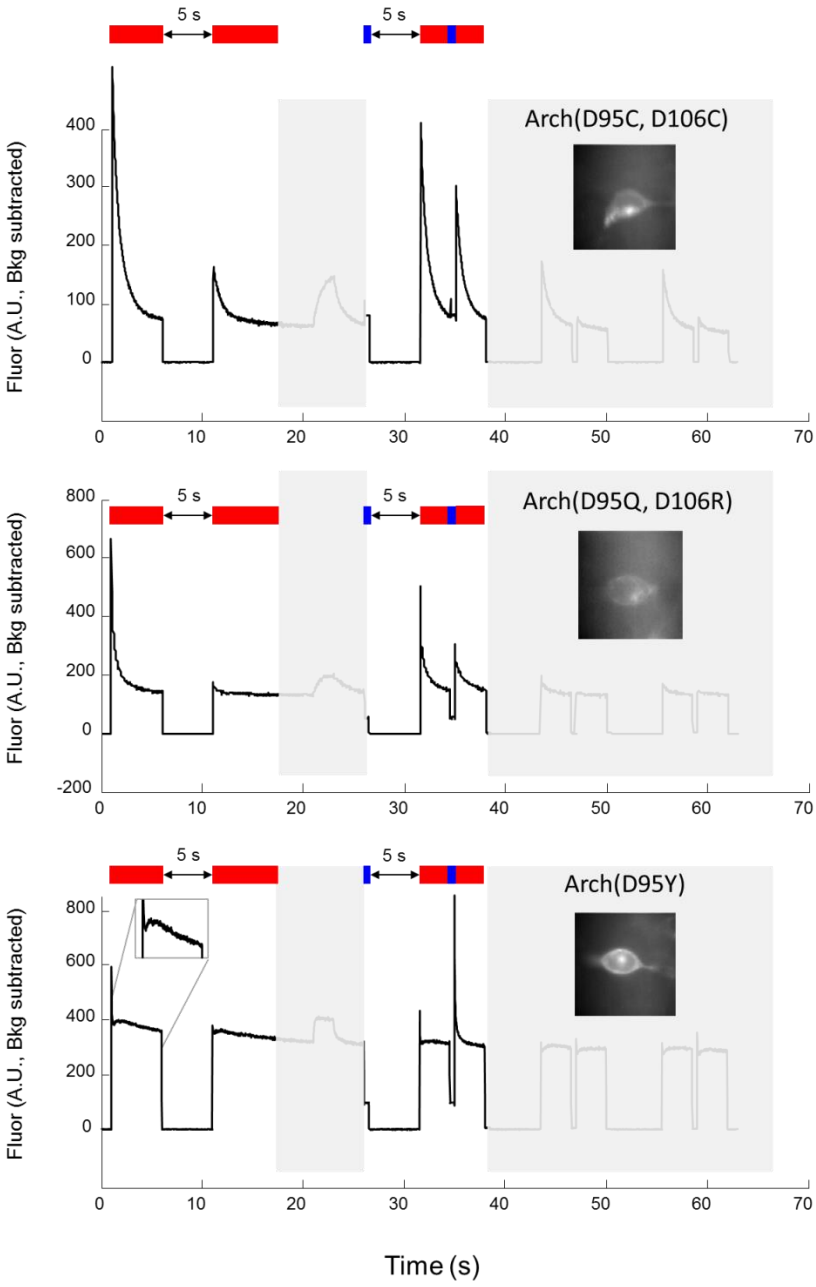

Figure 3-22. Screening Arch(D95X,D106X) mutants for optical bistability. Each of the three mutants above (Arch(D95C, D106C), Arch(D95Q,D106R), and Arch(D96Y)) was subjected to the indicated illumination sequence; note that only part of the illumination sequence is shown to draw attention to particular transitions. This dataset yielded some interesting findings. For example, 488 nm light increases the fluorescence of each mutant; but while the population of this fluorescent state appears to increase in the absence of light for Arch(D95C,D106C) and Arch(D95Q,D106R), it decreases for Arch(D95Y).

3.5.2 Developing FRET-based Flash Memory sensors

Other members of my lab have characterized the fluorescence of fluorescent proteins fused to Arch as a function of membrane voltage [68]. The fluorescence of mOrange in an Arch-mOrange fusion is inversely proportional to the membrane potential. This finding supports the hypothesis that the fluorescence of mOrange is quenched by the fluorescent state of Arch (whose absorption spectrum overlaps with the emission spectrum of mOrange), while the non-fluorescent states of Arch (which are blue-shifted relative to the fluorescent state) do not quench mOrange fluorescence as effectively. I would like to use FRET to read out the population of the fluorescent state in Arch(D95H), Arch(D95Q), and any other promising Flash Memory sensors that we find. Figure 3-23 outlines the principle behind this idea, by illustrating the proposed absorption spectra of two states in an Arch-based Flash Memory sensor and showing how these two states could have different effects on eGFP and/or mOrange fluorescence.

Using brighter fluorophores to probe the state of Arch would facilitate wide-spread use of Flash Memory sensors among neuroscientists, since Arch-based probes are dim relative to GFP-based probes (Arch(D95H) is 0.5% as bright as eGFP (Fig. 3-5a)).

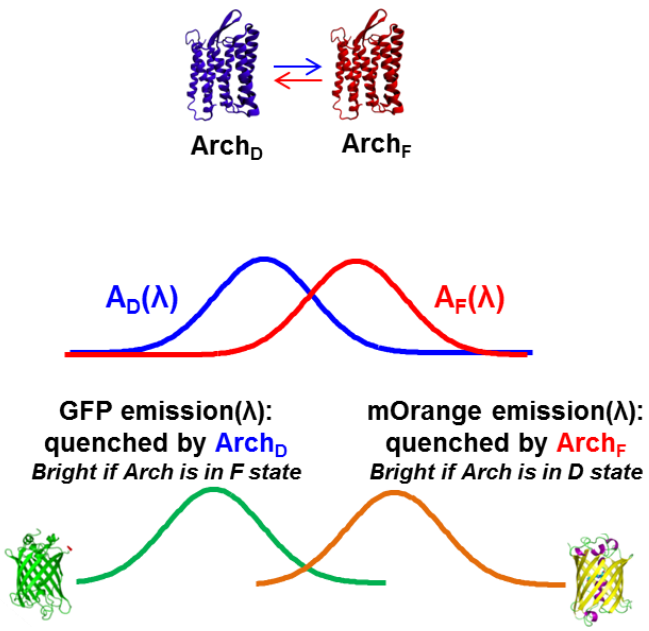

Figure 3-23. Proposed scheme of FRET-based Flash Memory. Instead of reading out Arch fluorescence directly, one can imagine using a different fluorophore to probe the state of Arch. For example, the emission of eGFP may overlap with the absorption spectrum of Arch in the dark manifold, but not the absorption spectrum of the F state. Thus, eGFP will be dim when Arch is primarily in its non-fluorescent state(s), and bright when Arch is in its fluorescent state.

4
Absolute voltage measurement

As we have established, plasma membrane voltage is a fundamentally important property of a living cell; its value is tightly coupled to membrane transport, the dynamics of transmembrane proteins, and to intercellular communication. Accurate measurement of the membrane voltage could elucidate subtle changes in cellular physiology, but existing genetically encoded fluorescent voltage reporters are better at reporting relative changes than absolute numbers. We exploit the light- and voltage-dependent properties of Arch(D95H) to engineer a new technique for quantitatively determining absolute membrane voltage. This technique uses a novel illumination protocol, consisting of a blue "pump" pulse followed by an orange "probe" pulse. The temporal response of Arch(D95H) fluorescence during the orange probe pulse encodes the absolute voltage. Measurements of voltage in HEK cells using this technique were robust to variation in imaging parameters and in gene expression levels, and reported voltage with an absolute accuracy of 10 mV. With further improvements in membrane trafficking and signal amplitude, time-domain encoding of absolute voltage could be applied to investigate many important and previously intractable bioelectric phenomena.

4.1 Introduction

Genetically encoded fluorescent reporters of membrane voltage enable non-invasive optical monitoring of electrical dynamics in live cells. With recent advances in speed and sensitivity, one can now visualize single action potentials in neurons and cardiomyocytes, *in vitro* [7, 69, 70] and *in vivo* [54, 71, 72]. These intensity-based measurements report relative changes in membrane voltage, not its precise numerical value. This approach is appropriate for detecting fast action potentials and sub-threshold events, but not for measuring slower shifts in resting voltage, such as occur during embryonic development [73], stem cell differentiation [74], wound healing [75], programmed cell death [76], and plant responses to herbivory [77, 78]. Studies of these slow voltage dynamics would benefit immensely from a technique to optically monitor the absolute membrane voltage.

The problem of quantifying intensity-based measurements of genetically encoded fluorescent sensors is not a new one. Often, the biggest hurdle to overcome is the cell-to-cell variation in sensor expression levels. This challenge can be partially addressed by tagging the sensor of interest (e.g. Arch, to measure membrane potential) with a fluorophore (such as GFP, whose fluorescence is voltage-invariant), to normalize for expression of the sensor. One could express an Arch-eGFP fusion protein in a cell, measure the fluorescence of each fluorophore, and then divide Arch fluorescence by eGFP fluorescence. To convert this number into a quantitative measurement of voltage, one would have to take into account both the illumination intensities used to excite the fluorophores and the collection efficiency of the optics. Yet even after this painstaking

calibration, this ratiometric method is likely to yield inaccurate results due to differential photobleaching rates of the two fluorophores. Figure 4-1 illustrates the problem. Since eGFP and Arch photobleach at different rates, long-term ratiometic measurements of absolute voltage with an Arch-eGFP fusion protein would be inaccurate.

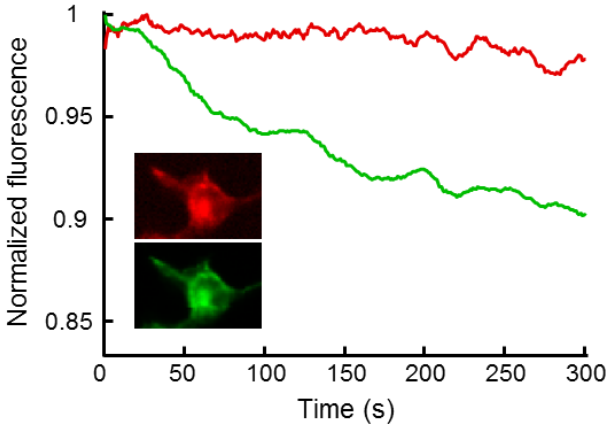

Figure 4-1. Differential rates of photobleaching confound efforts at ratiometric imaging. Under simultaneous illumination at 488 and 638 nm, eGFP (green dashed) photobleached faster than Arch(D95H) (red solid). Laser intensities were adjusted to achieve similar initial photon count rates from the two chromophores. (Inset) Dual-view spinning disk confocal images of HEK293 expressing Arch(D95H) (left) and eGFP (right).

A more robust way to adjust for variations in expression levels of a fluorescent sensor is to take a ratiometric measurement of the sensor's fluorescence at two different excitation wavelengths. This requires careful engineering and characterization of the sensor of interest. Figure 4-2 shows such a characterization of ratiometric pHluorin, a GFP-based pH sensor that can be used to quantitatively measure pH in living cells. Its fluorescence is pH-invariant when it is excited at 424 nm but pH dependent when it is excited at 475 nm, so the ratio of fluorescence at these two different excitation wavelengths yields a measurement that is independent of protein expression

levels and robust to photobleaching of the sensor. To convert this number into an absolute pH, one would need to take into account the illumination intensities of the excitation light sources.

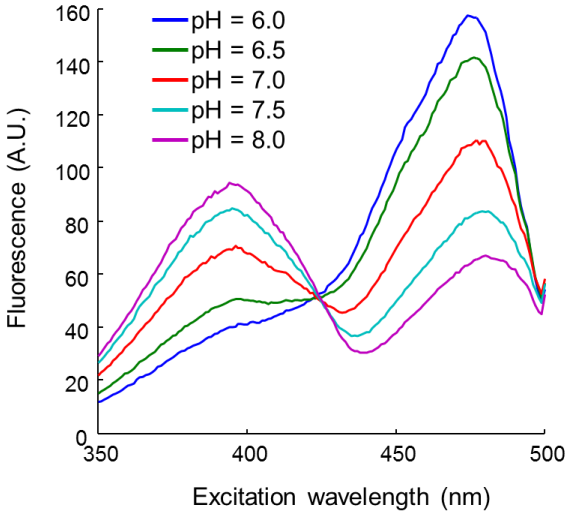

Figure 4-2. Ratiometric pHluorin excitation specta at different pH values. Spectra were obtained on ratiometric pHluorin that was expressed and purified from E. coli. An absolute readout of pH can be obtained by taking the ratio of pHluorin fluorescence at 475 nm excitation to its fluorescence at 424 nm excitation. This method is robust to variations in protein expression level and photobleaching, but is sensitive to variations in laser illumination intensity.

We realized that if we had a sensor whose fluorescence was voltage-invariant under certain illumination conditions and voltage-sensitive under a different set of conditions, we would be able to measure absolute voltage. We also realized that Flash Memory sensors – e.g. Arch(D95H) – had exactly this property [3]. These sensors, described in Chapter 3, have a unique three-state photocycle in which voltage affects the photostationary distribution of states, but only under certain illumination conditions. The proposed photocycle of Arch(D95H) is shown in Fig. 4-3a. A voltage-dependent equilibrium exists between two non-fluorescent states, D_1 and D_2. The state

D_2 can be optically interconverted into a fluorescent state, F. Blue light drives only the transition into F, while orange light drives transitions in both directions.

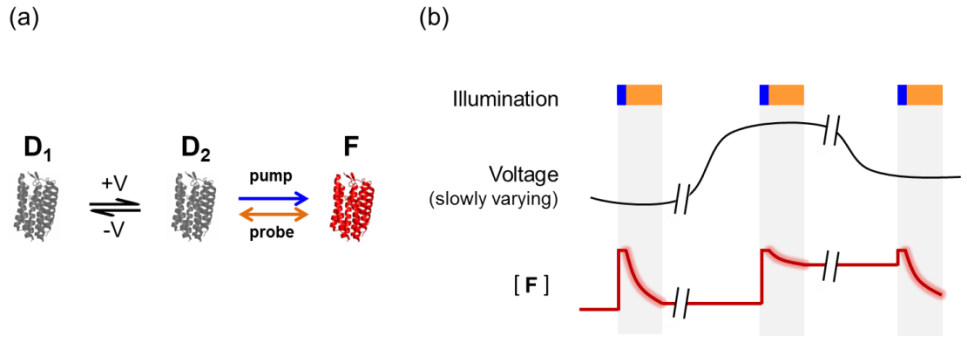

Figure 4-3. Proposed photocycle of Arch(D95H), and cartoon illustrating the desired behavior of an Arch-based absolute voltage sensor. (a) Arch(D95H) can be modeled using a three-state model where voltage tunes the rates of interconversion between two dark states (D1 and D2), and illumination tunes the rates of interconversion between D2 and a fluorescent state (F). (b) Cartoon illustration of a proposed method for measuring absolute voltage. Voltage is extracted from the fluorescence trace measured during an orange "probe" pulse that is immediately preceded by a blue "pump" pulse. The blue pulse initiates the protein in the F state. The orange probe pulse measures the population of this fluorescent state as it decays from its voltage-insensitive initial value, to its voltage-sensitive final value.

Careful examination of this photocycle led us to hypothesize that we could use a two color pump-probe illumination scheme to measure absolute voltage with Arch(D95H). We reasoned that an intense blue light (a "pump") could be used to initialize the protein into the fluorescent F state. (For those who just read Chapter 3 and are confused by this, please note that while a short period of dim blue illumination – such as that used in the light-gated voltage integrator of Chapter 3 – will drive a fraction of the protein into the F state in a voltage-dependent manner, an intense blue light of sufficient duration – such as what we propose using here – will saturate the F state in a voltage-invariant way.) Immediately after this blue pump pulse, we could illuminate the sample with an orange "probe" light that drives both the $D_2 \rightarrow F$ and $F \rightarrow D_2$ reactions

and allows the protein to redistribute into a voltage-dependent photostationary equilibrium.

To obtain a measurement of absolute voltage, we would only need to look at the extent of fluorescence relaxation during the probe interval. The initial fluorescence elicited by this probe would be voltage-insensitive, since the protein would be entirely in the F state at the beginning of the probe pulse. The steady-state value of probe fluorescence, on the other hand, would be voltage-sensitive. We predicted that the ratio between the initial probe fluorescence and the final probe fluorescence would provide a quantifiable readout of membrane potential. A cartoon showing how our proposed method would work is shown in Fig. 4-3b; note that at low voltages, the protein's predicted fluorescence drops dramatically during the probe pulse, while this drop is less pronounced at high voltages. Since we plan to measure fluorescence of a single species at a single excitation wavelength, our measurement should be robust to variations in illumination intensity and the collection efficiency of microscope optics.

In this chapter, we test our hypothesis that a two-color pump-probe illumination scheme can be used with Arch(D95H) to yield a quantitative measurement of membrane voltage. We found that voltage affected the amplitude of the fluorescence decay during the orange "probe" illumination pulse. This quantity provided a measure of absolute voltage that was insensitive to expression level, precise illumination intensity, or precise collection efficiency. We demonstrated this technique in Human Embryonic Kidney (HEK) cells.

4.2 Results

4.2.1 Repurposing Arch(D95H) as a reporter of absolute voltage: kinetic modeling

We first sought to confirm that our intuition regarding the expected behavior of Arch(D95H) under a sequential blue-orange illumination scheme was correct by simulating a kinetic model of this system in MATLAB. Using our knowledge of Arch(D95H) photophysics, we modeled the voltage-dependent response of Arch(D95H) to an illumination pulse sequence of intense blue light followed by orange light. Our goal was simply to get a qualitative sense of how the fluorescence of the protein would respond to this pulse sequence at different voltages – could we use the Flash Memory sensor Arch(D95H) as a reporter of absolute voltage?

To generate our model, we adapted the kinetic model of Chapter 3 (see Section 3.4.7). While we maintained the topology of the model (Fig. 4-3a), we made slight modifications to the rates to make them more consistent with the expected behavior of Arch(D95H) (in Chapter 3, rates were chosen to illustrate the qualitative behaviors of an ideal Flash Memory sensor). Specifically, we decreased the voltage sensitivity of the protein and increased the rate of photoconversion from D_2 to F ($k_{D2\rightarrow F}$) under blue illumination to model high-intensity blue illumination.

$D_1 \rightleftharpoons D_2$

	High voltage	Intermediate voltage	Low voltage
$k_{D1\rightarrow D2}$	1 ms	5 ms	10 ms
$k_{D2\rightarrow D1}$	10 ms	5 ms	1 ms

$D_2 \rightleftharpoons F$

	Intense blue illumination	Orange illumination
$k_{D2\rightarrow F}$	0.1 ms	50 ms
$k_{F\rightarrow D2}$	1000 s	50 ms

Table 4-1. Rates used to model the behavior of Arch(D95H) as a sensor of absolute voltage. This model is derived from the model of Flash Memory sensors that was proposed in Chapter 3. The rates have been slightly modified from those used in Chapter 3 to reflect differences in the illumination protocol when using Arch as a sensor of absolute voltage (e.g. $k_{D2\text{-}F}$ is faster under blue illumination in this model, because in this protocol we use intense blue light to initialize the protein in the F state; in the case of the light-gated voltage integrator of Chapter 3, dim blue light was used to increase the sensitivity of the sensor to brief voltage spikes.)

Table 4-1 gives the reaction time constants (inverse of the rate constants) for this model, which was used to simulate fluorescence traces at different voltages in response to a blue "pump" – orange "probe" illumination sequence (Fig. 4-4).

Figure 4-4 shows the results of our simulation; as predicted, the extent of fluorescence relaxation during the probe is a function of voltage (Fig. 4-4a). Figure 4-4b illustrates three voltage measurements in a slowly changing sample: the first at a low voltage, the second at a high voltage, and the third at an intermediate voltage. The fractional change in fluorescence during the probe pulse is a function of voltage but not of illumination intensity or protein concentration.

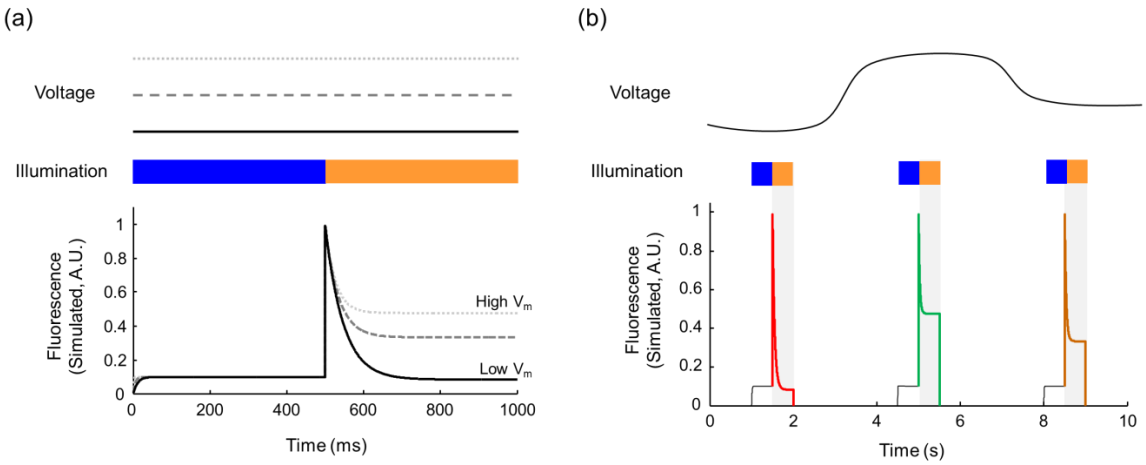

Figure 4-4. Modeling the response of Arch(D95H) to the paired pump/probe illumination protocol at different voltages. We used the photocycle model of Figure 4-3a with the rates in Table 4-1 to simulate the response of Arch(D95H) to the indicated voltage and illumination sequences. The traces in this figure are all simulated; real data appears in the next section.

4.2.2 Arch(D95H) quantitatively reports slowly varying membrane voltages

We used whole cell patch-clamp to set the membrane voltage of an isolated HEK cell expressing Arch(D95H)-eGFP to one of three constant values (V_m = -50, 0, or +50 mV). The cell was illuminated with a 488 nm "pump" for 500 ms, and this was immediately followed by a 594 nm "probe" for 500 ms. Fluorescence of Arch(D95H) was recorded throughout the pump and probe intervals. The relaxation of the fluorescence during the probe interval showed voltage dependence (Fig. 4-5). We quantified the fluorescence transient during the probe by the dimensionless metric $M(V_m) = F_i(V_m) / F_f(V_m)$, where $F_i(V_m)$ and $F_f(V_m)$ represent the initial and final fluorescence intensities during the probe interval, respectively.

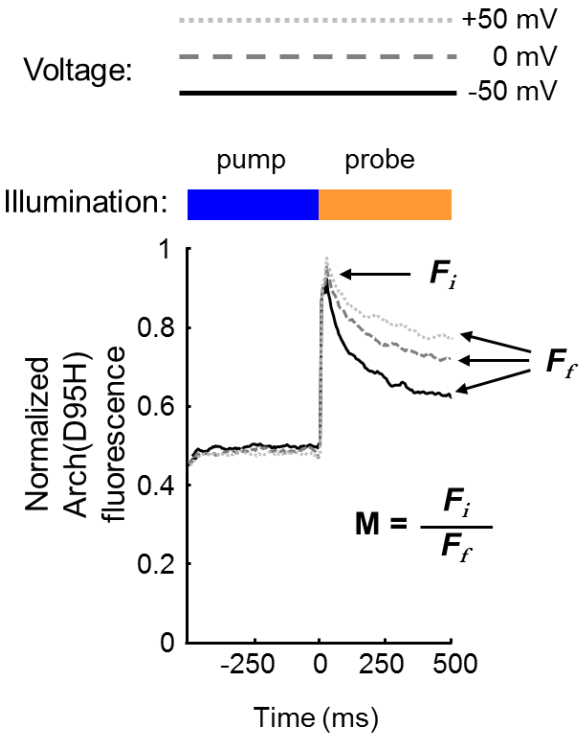

Figure 4-5. Probe intensity reports absolute voltage. Probe intensity traces of a HEK-293T cell expressing Arch(D95H)-eGFP, held at three voltages via whole-cell voltage clamp: -50 (solid), 0 (dashed), +50 (dotted) mV. We define a metric, M, as the ratio between the initial fluorescence and the final fluorescence of the probe (note that this definition differs slightly from the definition used in Chapter 3, but is conceptually the same).

We explored different imaging parameters to optimize the sensitivity of *M* to membrane potential. By choosing a pump fluence well into the saturation regime (I_{pump} = 40 W/cm^2, t_{pump} = 100 ms), measurements of *M* became robust to variations in I_{pump}. To achieve adequate fluorescence intensity during the probe interval, we operated at $I_{probe} \geq 80$ W/cm^2. In this regime, fluorescence was directly proportional to I_{probe}, so *M* was independent of probe intensity. The probe interval was selected to be long enough for fluorescence to reach steady state; we used $t_{probe} \geq 750$ ms. We inserted a dark interval between the pump and probe pulses, and varied t_{dark} from 0 to 2 s. We found that this dark interval only affected the voltage sensitivity of *M* by ~10%,

but was maximal for t_{dark} = 1 s. Thus, we settled on an optimal illumination scheme that consisted of a 100 ms pump pulse (488 nm, 40 W/cm^2), a 1 second dark interval, and a 750 nm probe pulse (594 nm, 80 W/cm^2).

With these optimal pump-probe parameters, we measured $M(V_m)$ in six cells from three dishes. For each cell, we used patch-clamp to vary V_m between -75 mV and 50 mV. Expression levels of the indicator varied widely between cells; hence, the plots of steady-state fluorescence vs. membrane voltage also varied widely between cells (Fig. 4-6a). The dimensionless measure $M(V_m)$ showed significantly less cell-to-cell variation than did the raw fluorescence (Fig. 4-6b). We asked how accurately one could estimate V_m from M in a cell given no prior information. The error in the voltage estimate, σ_V, depends on the error in the measurement of M, σ_M, by

$$\sigma_V = \left\langle \frac{\sigma_M}{\left| dM / dV_m \right|} \right\rangle_{V_m}$$

The plot of $M(V_m)$ was approximately a straight line between -75 and +50 mV, so it was acceptable to take the average over all cells and all voltages. The accuracy of voltage measurements was σ_V = 9.8 mV.

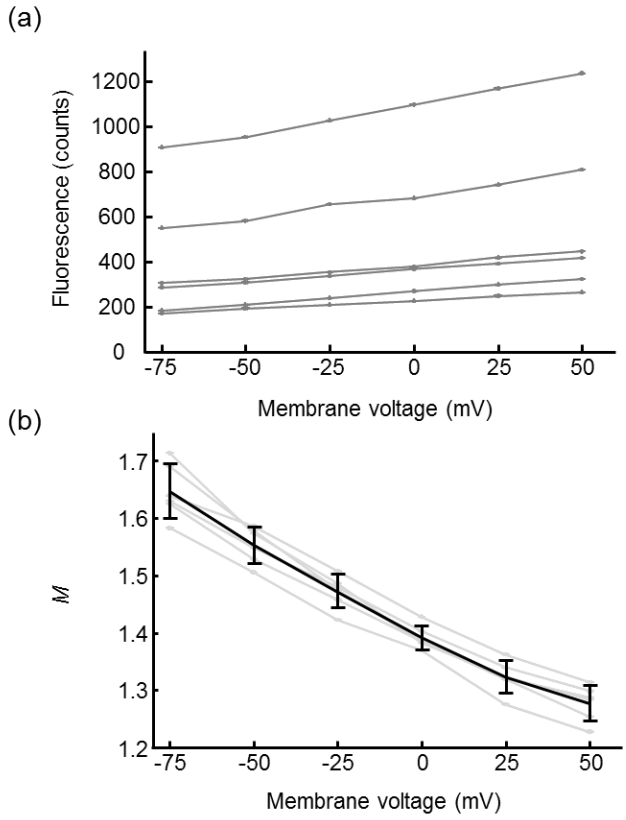

Figure 4-6. Arch(D95H) is an absolute voltage reporter. (a) Steady-state fluorescence of Arch(D95H) in six cells as a function of membrane voltage. Due to wide variations in protein expression levels, absolute fluorescence was not a robust measure of absolute voltage. (b) Gray lines show our measure of absolute voltage, $M(V_m)$, for the same six cells plotted in (a). $M(V_m)$ was calculated as in Fig. 4-5 from the fluorescence of a probe (594 nm, 80 W/cm^2, 750 ms) that was preceded by a pump (488 nm, 40 W/cm^2, 100 ms) one second prior. Note that a dark interval was introduced between the pump and probe in the collection of this data. The fractional amplitude of the fluorescence relaxation, M, reported voltage with an absolute accuracy of $\sigma V = 9.8$ mV.

4.3 Discussion

Detecting rapid changes is easily accomplished using genetically encoded fluorescent indicators; but slowly changing quantities are difficult to probe with such a readout. Several factors, such as photobleaching, expression levels of a sensor, and sample movement are difficult to control for over the course of a long-term measurement. Here, we exploit the fact that Arch(D95H) can be initialized in its bright

state under blue illumination in a voltage-independent manner, allowing us to determine exactly how much protein is present. We measure fluorescence of this sensor with orange light immediately after a flash of blue light (when all of the protein is in its fluorescent state), and we compare this to the steady-state voltage-dependent fluorescence of the sensor under orange illumination. The ratio of these two measurements reports absolute membrane potential to within 10 mV.

What phenomena might one study with the present accuracy of 10 mV? Bacterial resting membrane potential ranges from -80 to -140 mV depending on growth state and many environmental factors. Bacterial membrane voltage also undergoes "spikes" which may last up to tens of seconds and likely have voltage swings > 100 mV [10]. Direct electrode-based calibration of voltage reporters in bacteria has not been feasible, so an absolute reporter could quantify these phenomena. In the context of embryonic development, stem cells with membrane voltages near zero differentiate into electrically diverse tissues: fibroblasts with voltage near -65 mV, neurons with voltage near -70 mV, and cardiomyocytes with voltage near -90 mV. The dynamics and modifiers of these transitions in embryonic development are largely unexplored.

For absolute voltage measurements to become more broadly applicable, several aspects of the reporter need to be improved. Primarily, improved membrane trafficking will prevent conflation of intracellular membrane voltages with plasma membrane voltage, thereby simplifying data analysis and improving accuracy. Overall brightness and voltage-sensitivity are also important parameters to improve. Finally, the protein should have voltage- and illumination-dependent rates in its photocycle, and at least

one fluorescent state. A near-infinite variety of Arch mutants await exploration; and Arch is but one of more than 5,000 known microbial rhodopsins [79]. It is likely that mutants with better performance can be found. One candidate protein for further exploration is Arch(D95Y), whose complex dynamics could probably entertain and befuddle future photophysicists for quite a while. We previously observed that the fluorescence of Arch(D95Y) in response to red illumination shows an initial decrease, followed by an increase, followed by a decrease (Fig. 3-24); this mutant also had a non-monotonic F vs. V curve (Fig. 1-6).

While the ratiometric method that we employ to measure absolute voltage with Arch(D95H) is powerful, it has its limitations. A two-point measurement can only adjust for one varying parameter; in this case, that parameter is protein expression level. Therefore, our technique – as it has been presented – is not robust to variations in background autofluorescence. This did not affect the precision of our measurements, likely because the autofluorescence of our sample was low and we used a spinning disk confocal microscope, but background autofluorescence could pose a bigger problem *in vivo*.

To control for varying background, we need to extract more information from our data than just the fluorescence at two time points. Fortunately, our method gives us a bunch of extra measurements for free! Not only do we know the initial fluorescence and final fluorescence elicited by our probe pulse, but we also know exactly how the fluorescence varies with time during this pulse. While these time dynamics are unremarkable and provide little additional information for Arch(D95H),

one could imagine that somewhere in the rich photophysical repository of Arch(D95X) mutants, there is a mutant whose voltage-dependent fluorescence dynamics involve more than a simple exponential decay. In these mutants, a robust signature of the membrane voltage may be encoded in the temporal dynamics of fluorescence under a specific illumination protocol. One could extract this signature from a complex time-varying fluorescence trace using principal component analysis (PCA), as in ref. [4].

4.4 Materials and Methods

4.4.1 Molecular biology, cell culture, and electrophysiology

Arch(D95H)-eGFP was expressed in HEK-293T cells under a ubiquitin promoter and patch-clamp experiments were performed under whole cell voltage clamp as previously described in Chapter 3.

4.4.2 Microscopy and image analysis

Figure 4-7 shows the experimental apparatus.

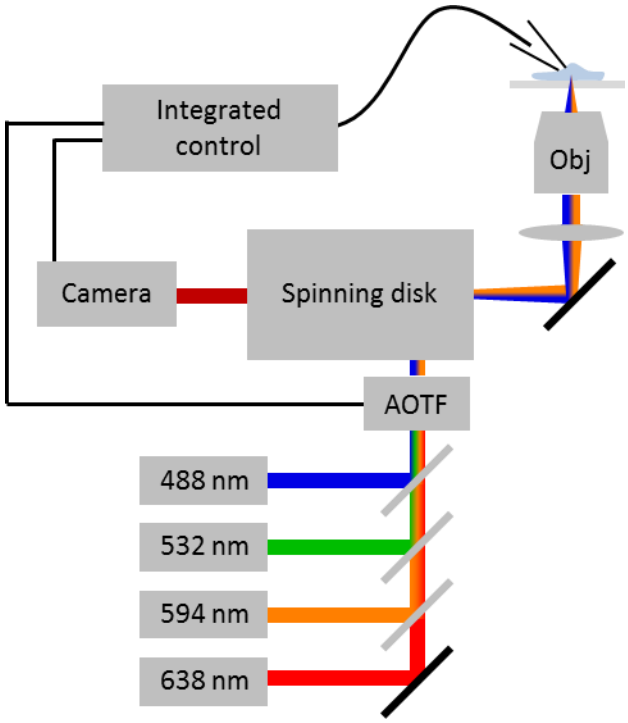

Figure 4-7. Experimental apparatus. Four lasers were combined with dichroic mirrors and passed through an AOTF to allow for rapid control of illumination intensity and wavelength. Excitation light was passed to the sample via a spinning disk; emission fluorescence passed through this same spinning disk and was collected on a camera.

This system comprised a spinning disk confocal microscope with up to four independently modulated laser lines. A patch-clamp apparatus controlled the membrane voltage in HEK cells expressing candidate indicators. Beams from solid state lasers at 488 nm (Coherent Obis, 50 mW), 532 nm (Coherent Compass 315M, 100mW), 594 nm (Cobalt Mambo, 100 mW), and 638 nm (CrystaLaser, 100 mW) were combined using dichroic mirrors (Semrock) and passed through an acousto-optic tunable filter (AOTF; Gooch & Housego 48058) that allowed for spectral and temporal control of sample illumination. Illumination was directed into a modified Yokogawa spinning disk confocal imaging system (CSU-X1) attached to an Olympus IX71 inverted base. Imaging was performed with a custom dichroic optimized for 405, 488, 594 nm excitation

(Chroma). Maximum intensities after the objective (Zeiss 20x Plan-Apochromat NA 1.0) were 43 and 82 W/cm2 for 488 and 594 nm, respectively. Emission fluorescence passed through a dual-band filter (Chroma) optimized for 488 and 594 excitation and was collected on an EMCCD camera (Andor iXon X3, 512 x 512 pixels).

Alternatively, illumination was directed onto the sample via widefield epifluorescence with a 650 nm dichroic mirror (Semrock). Intensities at the sample were 175, 80, 184, 193 W/cm^2 for 488, 532, 594, 638 nm light, respectively. Emission fluorescence was filtered through a 664 nm long pass filter (Semrock) before collection by the same Andor camera.

A custom LabView (National Instruments) script along with a National Instruments DAQ (PCIe-6323) controlled the AOTF, patch-clamp amplifier, and camera for data acquisition. Data from images and current recordings were analyzed in MATLAB. Membrane-localized protein was separated from intracellular protein by selecting voltage-sensitive pixels corresponding to the plasma membrane via the method described in [8].

Part II

Optogenetic control

5

The “Stoplight” technique: pairing functional fluorescence imaging with optogenetic control

To study the impact of neural activity on cellular physiology, one would like to combine precise control of firing patterns with highly sensitive probes of cellular physiology. Light-gated ion channels, e.g. Channelrhodopsin-2, enable the former, while GFP-based reporters, e.g. the GCaMP6f Ca^{2+} reporter, enable the latter. However, for most actuator-reporter combinations, spectral overlap prevents straightforward combination within a single cell. Here we explore multi-photon multi-wavelength control of channelrhodopsins to circumvent this limitation. The “Stoplight” technique uses channelrhodopsin variants that are opened by blue light and closed by orange light. Cells are illuminated with constant blue light to excite fluorescence of a GFP-based reporter. Modulated illumination with orange light negatively regulates activation of the channelrhodopsin. We performed detailed photophysical characterization and kinetic modeling of five candidate “stoplight” channelrhodopsins. The most sensitive, CoChR(C108S), enabled all-optical measurements of activity-induced calcium transients in single cultured rat hippocampal neurons.

5.1 Introduction

5.1.1 Combining optogenetic stimulation and fluorescence imaging

Activity dependent changes in neural physiology are a hallmark of neural metabolism and information processing. Action potential generation and neurotransmitter release constitute significant metabolic loads, and maintenance of homeostasis in the presence of changing energy demands engages multiple metabolic pathways [80]. Activity-dependent changes in neurons are integral in learning and memory, and contribute to the pathophysiology of diseases ranging from epilepsy to schizophrenia. Despite the fundamental importance of activity-dependent changes in neuronal physiology, we still do not fully understand many of the underlying pathways. A method to perturb neuronal activity with high spatiotemporal resolution while monitoring real-time cellular responses would be a valuable tool in this effort [81].

Optical tools for perturbing neural activity include photo-uncaged glutamate [82, 83], light-activated agonists of endogenous ion channels [84, 85], azobenzene-derivatized glutamate receptors [86], and heterologously expressed microbial rhodopsins [87]. Of these, the rhodopsins have been particularly effective because they can be genetically targeted to specific sub-classes of cells, are readily activated with modest doses of visible light, and typically do not require an exogenous cofactor (the retinal chromophore is present at sufficient levels in most vertebrate tissues). Channelrhodopsin-2 (ChR2), a light-gated cation channel from *Chlamydomonas reinhardtii*, allows optical control of neural activity in species ranging from worms to monkeys [88]. New channelrhodopsins are frequently added to the optogenetic toolkit,

distinguished by kinetic or spectroscopic features optimized for particular classes of experiments [89, 90, 91].

Protein-based fluorescent sensors have been developed for real-time measurements of membrane voltage, pH, calcium, ATP, NADH, cAMP, glutamate, reactive oxygen species, several redox potentials, activity of kinases and phosphatases, and many other modalities [92, 93]. Targeting of these reporters to sub-cellular domains in genetically specified subpopulations of neurons enables detailed studies of calcium fluxes, metabolic state, vesicle cycling, and signaling pathways. While fluorescent proteins have been developed with excitation maxima throughout the visible spectrum [94], the vast majority of single-wavelength or FRET-based reporters contain a derivative of GFP (ex. 488 nm, em. 509 nm).

To achieve simultaneous optical perturbation and readout within the same cell, one must minimize the degree of optical crosstalk: the light used to trigger the actuator should not perturb the fluorescence of the reporter; and the light used to excite the reporter should not trigger the actuator (Fig. 5-1a). Several approaches have been developed to achieve these goals. One- and two-photon glutamate uncaging is compatible with imaging of GFP-based reporters [95]. Channelrhodopsin actuation can be paired with red-shifted voltage- or calcium-sensitive organic dyes [96, 97] or proteins [98, 99, 100, 101], though the number of reporters sufficiently red-shifted is limited.

Efforts to produce red-excited channelrhodopsins have shifted the excitation peak to ~600 nm, but unfortunately these proteins retain 20-30% activation at the blue wavelengths used for excitation of GFP [89]. Fig. 5-1b shows the spectral overlap of

GCaMP3, a popular Ca^{2+} reporter, with a panel of channelrhodopsin actuators (adapted with permission from [89] and [53]). Spectral overlap has remained a significant barrier to paired optical actuation and sensing in single neurons.

The complex photocycles of microbial rhodopsins open the possibility of sophisticated optical control. One can use spectrally and temporally tuned pulses of light to interact with photocycle intermediates, thereby driving the population into states or distributions of states inaccessible under steady-state illumination. We previously applied this strategy to record stable photochemical imprints of membrane voltage (Chapter 3, ref. [3]) and to encode absolute values of membrane voltage into nonequilibrium dynamics of photocycle intermediates (Chapter 4, ref. [4]). Here we apply this strategy to modulate channelrhodopsin photocurrents in the presence of continuous blue illumination.

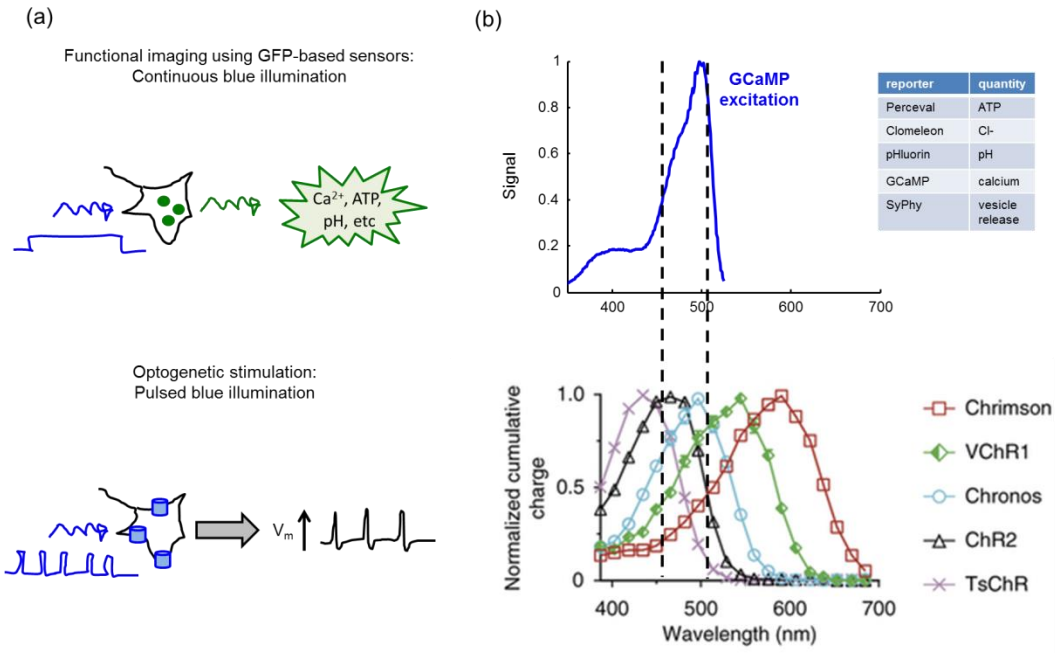

Figure 5-1. Spectral overlap limits combination of GFP-based reporters and channelrhodopsin-based actuators. (a) Top: continuous blue illumination is used to monitor GFP-based reporters of dynamic physiological quantities. Bottom: pulsed blue illumination is used for optogenetic stimulation. These two modalities cannot be combined in a single cell. (b) Top: Fluorescence excitation spectrum of GCaMP, a sensor of [Ca^{2+}]. The table lists some widely used reporters with similar spectra. Bottom: Action spectra of a panel of channelrhodopsins (from ref. [89]). All channelrhodopsins are activated to some extent by the blue light used to excite a GFP-based reporter.

5.1.2 Repurposing step function opsins as "stoplight" channelrhodopsins

Step-function opsins (SFO) are channelrhodopsin variants that are opened by blue light and closed by orange or red light [102]. Fig. 5-2a shows a simplified version of the SFO photocycle. We reasoned that under continuous blue illumination, one could modulate the population in the open state by modulating the intensity of simultaneously applied orange light (Fig. 5-2b). By collecting reporter fluorescence at wavelengths bracketed by the blue and orange wavelengths, one could image the reporter with negligible crosstalk from the modulated orange beam. The challenge, then, was to identify an SFO and illumination conditions (intensities, wavelengths,

times) that would facilitate robust crosstalk-free fluorescence imaging with simultaneous optogenetic stimulation. We call this scheme “stoplight” because the photocurrent is stopped by red (or orange) light.

Due to the countervailing effects of blue and orange light on the open-state population, the required orange intensity depends on the blue intensity. The blue intensity is set by the attributes of the fluorescent reporter and the demands for spatial and temporal resolution in the imaging. For instance, single-molecule or high-magnification experiments require much higher intensity than population-average measurements; voltage imaging at a 1 kHz frame rate to detect neuronal action potentials requires higher illumination intensity than imaging at a 50 Hz frame rate to detect Ca^{2+} transients. Take the example of imaging a GFP-based reporter expressed under a strong constitutive promoter (e.g. CaMKIIa or hSynapsin in neurons). To achieve ~1 μm spatial resolution and ~10 ms temporal resolution, one might illuminate with blue light (488 nm) at an intensity of 0.1 – 10 W/cm^2. We thus measured photocurrents with blue illumination in this range, and with a simultaneously applied second beam of variable intensity and wavelength.

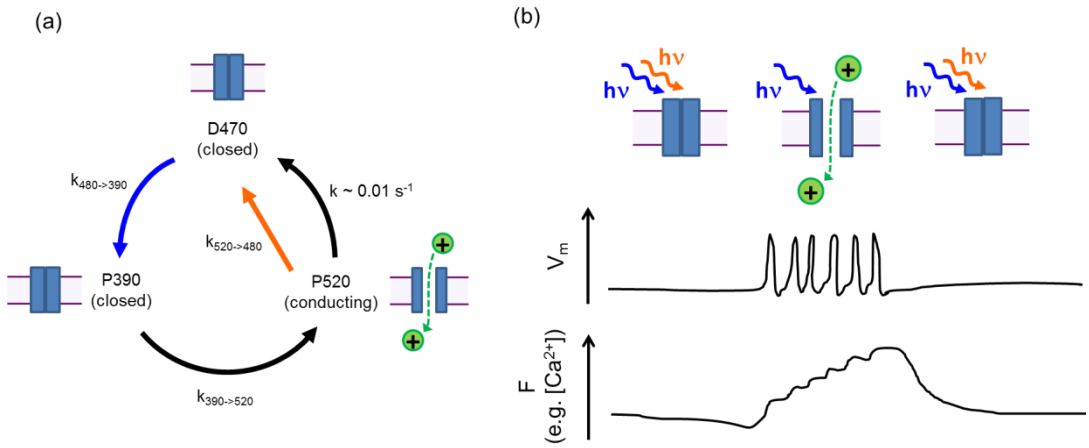

Figure 5-2. Stoplight optical control of a step-function opsin. (a) Simplified photocycle of a step-function opsin adapted from [102], comprising a blue-absorbing ground state (D470), and an orange-absorbing open state (P520). The P390 intermediate limits the maximum rate at which the protein can go from the ground state to the open state. The spectra of the states are centered around the indicated wavelengths, but note that they overlap. (b) Stoplight illumination scheme. Simultaneous application of weak (~1 W/cm^2) blue and strong (~300 W/cm^2) orange illumination leaves most channels closed. Removal of the orange light opens the channel. In a neuron, this conductance could induce a train of action potentials and induce a fluorescence response in a GFP-based reporter, here represented by a Ca^{2+} indicator. Re-application of orange light closes the channel and stops neural firing.

5.2 Results

Measurements were performed on a homemade system for simultaneous patch clamp electrophysiology and multi-wavelength fluorescence illumination and imaging, described in detail in Chapter 3. In brief, lasers at wavelengths of 488, 532, 561, 594, and 640 nm were combined by dichroic mirrors and modulated via an acousto-optic tunable filter to select the time-dependent intensity for each wavelength at the sample. Fluorescence imaging was performed in an inverted epifluorescence microscope equipped with a high numerical aperture objective and a scientific CMOS camera. Membrane electrical properties were measured via whole-cell patch clamp in either constant-current or constant-voltage mode. Illumination, imaging, and

electrophysiology were synchronized via custom LabView software. All experiments were conducted at 23 °C.

5.2.1 ChR2(C128S) can be closed under steady-state blue illumination by the addition of a 594 nm "stoplight"

We first tested the previously described SFO, ChR2(C128S) [102]. We expressed ChR2(C128S)-eGFP in HEK293T cells and applied the illumination sequence shown in Fig. 5-3a. We simultaneously monitored membrane current via whole-cell patch clamp, maintaining V_m= -70 mV. A pulse of red light (640 nm, 700 W/cm^2, 300 ms) initialized the protein in the fully closed D470 state. A pulse of blue light of variable intensity (0.03 – 20 W/cm^2, 1000 ms) opened the channel and induced an inward (negative) photocurrent. During the middle 500 ms of the blue pulse, a "stoplight" pulse of orange light (594 nm, 300 W/cm^2) was added to the illumination and the photocurrent decreased in magnitude. The photocurrent traces in Fig. 5-3a illustrate the countervailing influences of blue and orange light. For the weakest blue illumination, the orange light largely suppressed the photocurrent (99% fractional inhibition); but this blue intensity was too low for fluorescence imaging, and only opened the channel slowly. For the strongest blue illumination, the orange light only partially closed the channel (25% fractional inhibition).

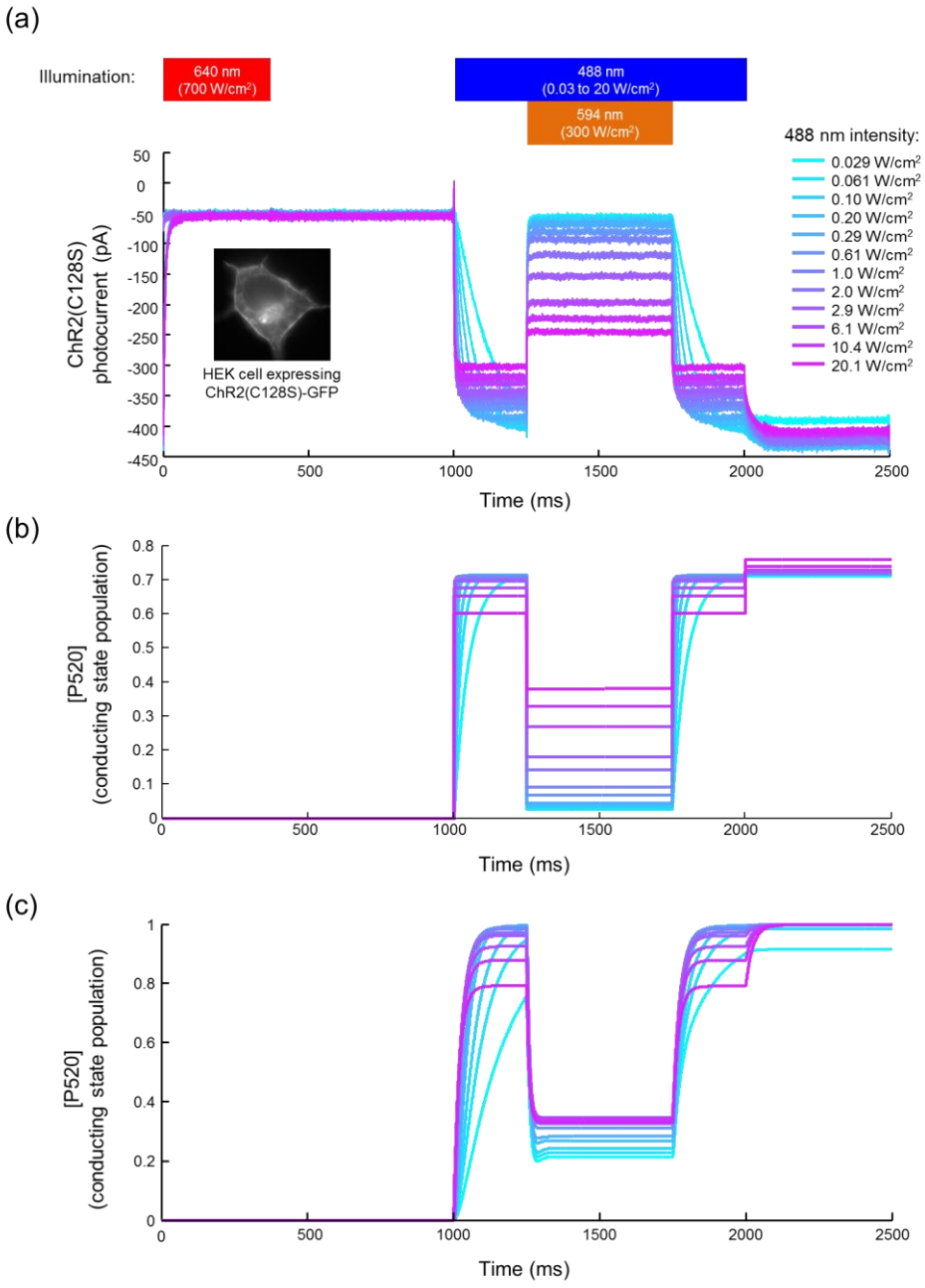

Figure 5-3. ChR2(C128S) can be closed under steady-state blue illumination by the addition of a "stoplight". (a) A HEK-293T cell expressing ChR2(C128S) was illuminated with the indicated pulse sequence under whole-cell voltage clamp at -70 mV. An open channel corresponds to a negative current. Intense orange light (300 W/cm², 594 nm) suppressed ~95% of the photocurrent induced by moderate blue light (~300 mW/cm², 488 nm). (b) Results of a kinetic simulation of the photocycle model in Fig. 5-2a using rates based upon guesstimation. (c) Results of a kinetic simulation of the photocycle model in Fig. 5-2a using rates calculated from our data. In both (b) and (c), each trace shows the expected population of the P520 conducting state at a different 488 nm illumination intensity (as in part (a)).

Two features of the data in Fig. 5-3a are less intuitive. First, the steady-state photocurrent under blue-only illumination (e.g. from t = 1000 – 1250 ms) was a decreasing function of blue intensity. Second, when the blue light was stopped (t = 2000 ms) the photocurrent increased in magnitude. Both effects can be understood by reference to the photocycle of Fig. 5-2a and by noting that all the light-driven transitions are spectrally broad. Thus, the blue light drives the P520 → D470 transition as well as the D470 → P390 transition. Under blue-only illumination at intensity I, we define the rates as $k_{470 \rightarrow 390} = k_1 I$, $k_{390 \rightarrow 520} = k_2$, and $k_{520 \rightarrow 470} = k_3 I$. We neglect thermal isomerization from P520 to D480. Solving the kinetic equations yields a steady-state fraction of the population in the conducting P520 state:

$$[P520]_{ss} = \frac{A}{B + I} \quad ,$$

where $A = k_2/k_3$, and $B = k_2/k_1 + k_2/k_3$. Thus $[P520]_{ss}$ is a decreasing function of I. The increase in photocurrent magnitude at the end of the blue illumination arises from spontaneous transfer of population from P390 → P520, while the rate of P520 → D480 becomes negligible.

We simulated the kinetic scheme of Figure 5-2a under the illumination conditions of the experiment in Figure 5-3a. To incorporate illumination with a 594 nm stoplight into the model, we introduced two new parameters, n and m. We define m and n as the fractional absorption cross sections of D470 and P520, respectively, at 594 nm (relative to 488 nm). Taking into account these new parameters, our rates with blue illumination at intensity I_{blue} and orange illumination at intensity $I_{stoplight}$ are $k_{470 \rightarrow 390}$ =

$k_1(I_{blue} + mI_{stoplight})$, $k_{390 \rightarrow 520} = k_2$, and $k_{520 \rightarrow 470} = k_3(I_{blue} + nI_{stoplight})$. Initially, we set k_1 = 0.5 $cm^2W^{-1}ms^{-1}$, k_2 = 15 ms^{-1}, k_3 = 0.2 $cm^2W^{-1}ms^{-1}$, n = 0.001 and m = 0.05; these parameters were chosen largely by trial-and-error guesswork. Using these parameters, we calculated the time-dependent population of the conducting state (P520) (Fig. 5-3b). This simulation recapitulated the main features of the data, lending credence to the kinetic model.

We then asked ourselves if there was a better way to set the parameters in our model; could we pull these parameters out of our data? In short, the answer is yes (a description of how we did this is given in Section 5.4, "Kinetic model"). The parameters that resulted from our calculations were: k_1 = 0.22 $cm^2W^{-1}ms^{-1}$, k_2 = 0.042 ms^{-1}, k_3 = 5.5 x 10^{-4} $cm^2W^{-1}ms^{-1}$, n = 0.0005 and m = 0.45. We calculated the time-dependent population of the conducting state (P520) using these new parameters (Fig. 5-3c). Comfortingly, our simulation once again recapitulated the main features of the data.

5.2.2 Optimization of stoplight wavelength and intensity for ChR2(C128S)

We next varied the wavelength and intensity of the stoplight to identify the optimal parameters for fast and high-contrast photoswitching. The illumination protocol was the same as in Figure 5-3. We measured steady-state photocurrents (i_{ss}) at V_m= -70 mV, as a function of blue illumination intensity (I_{blue}) either in the absence of a stoplight or with stoplight wavelength selected from λ_{SL} = 532, 594, or 640 nm. In all cases the stoplight intensity was I_{SL} = 200 W/cm^2 (Fig. 5-4a).

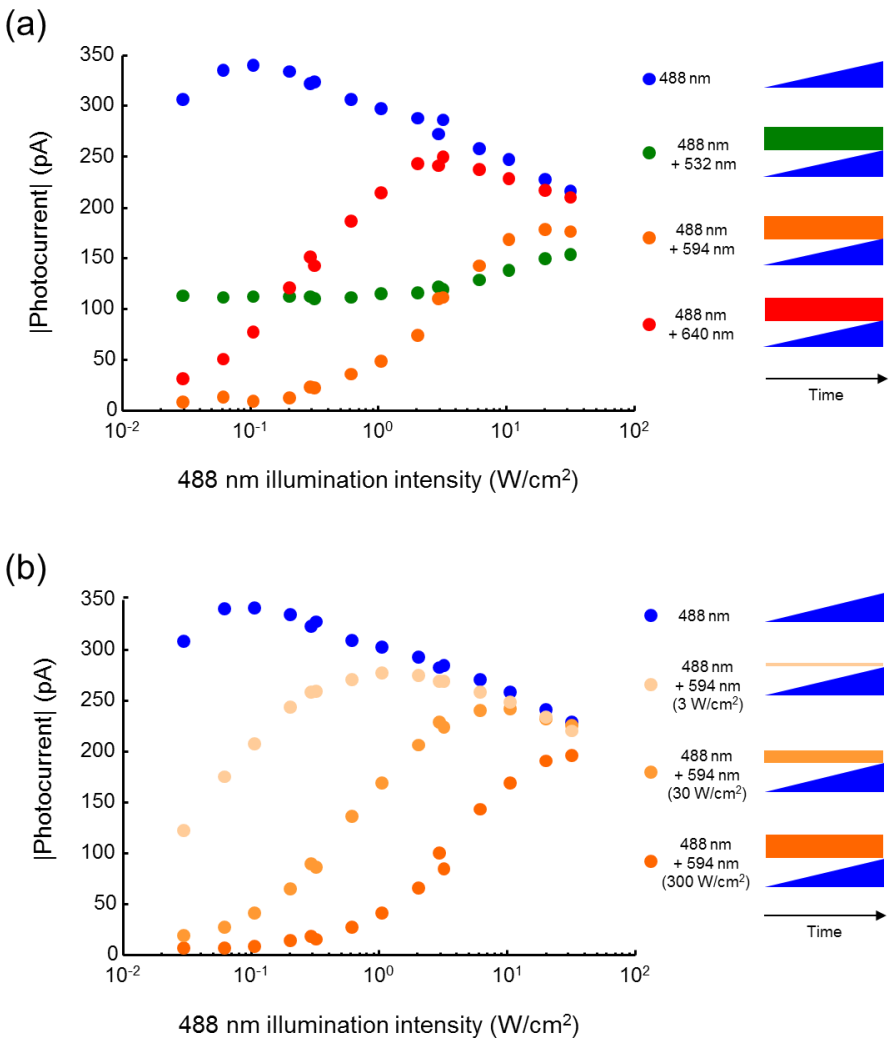

Figure 5-4. Optimization of illumination parameters for ChR2(C128S) (a) Varying the wavelength of a 200 W/cm^2 "stoplight" at different blue intensities. (b) Varying the intensity of a 594 nm "stoplight" at different blue intensities.

A good stoplight would minimize the photocurrent under all blue illumination intensities. The red (640 nm) stoplight effectively shut the channel at very low I_{blue}, but was overpowered by the blue beam for I_{blue} > 0.1 W/cm^2. The red beam was too far off resonance with the P520 transition to rapidly drive P520 → D470. The green (532 nm) stoplight led to significant current at all values of I_{blue}. Due to the finite width of the transitions, the green beam drove D470 → P390 in addition to P520 → D470. Thus the

green beam was also not an effective stoplight. The orange (594 nm) stoplight achieved a balance between maximizing the rate of P520 → D470, while minimizing crosstalk to D470 → P390. For I_{blue} between 0.1 and 1 W/cm^2, the orange beam suppressed photocurrent by 97 – 84 %.

We next investigated the effect of stoplight intensity (Fig. 5-4b). Ideally one would like to minimize the stoplight intensity to avoid risk of photodamage and to enable application over as wide a field of view as possible for a given laser power. As expected, weaker stoplights were less effective at counteracting the blue photocurrent. At I_{blue} = 300 mW/cm^2, the 300 W/cm^2 stoplight inhibited ~95% of the blue photocurrent, compared with ~75% inhibition at 30 W/cm^2, and ~25% inhibition at 3 W/cm^2. Thus for ChR2(C128S), the stoplight must be ~1000-fold more intense than the blue light used for imaging.

5.2.3 Characterization of "stoplight" behavior in novel SFOs

Our spectroscopic explorations of ChR2(C128S) elucidated the critical parameters for stoplight performance. The closed and open states should have minimal spectral overlap, to maximize the contrast in photocurrent between the blue-only and the blue-plus-stoplight illumination conditions. Furthermore, the protein should have high conductance in the blue-only state. This conductance is the product of the expression level, the efficiency of trafficking to the plasma membrane, and the unit conductance of the open channel. Visual inspection of neurons expressing ChR2(C128S) showed poor membrane trafficking, and indeed in our experiments and in previous

reports [102], this protein did not pass sufficient photocurrent to induce robust spiking in cultured neurons.

We introduced mutations homologous to C128S into other channelrhodopsin variants which had shown superior trafficking and sensitivity. The mutant ChR2(H134R) passes larger photocurrents than wild-type ChR2 [103], so we made ChR2(C128S, H134R). A recent screen for improved channelrhodopsins identified two with extremely large photocurrents: one from *Chloromonas oogama* (CoChR) and one from Scherffelia dubia (sdChR) [89]. We thus made CoChR(C108S) and sdChR(C138S). We found that the mutant sdChR(E154A) had a blue-shifted excitation peak for its ground state, so we also made sdChR(C138S, E154A).

We expressed each of these mutants in HEK cells and characterized their photocurrents and kinetics under blue illumination (488 nm, 300 mW/cm^2) and simultaneously modulated orange illumination (594 nm, 300 W/cm^2) (Fig. 5-5a). The ideal stoplight channelrhodopsin would show large photocurrent with blue-only illumination, and large fractional inhibition by orange light (i.e. reside in the top right region of Fig. 5-5a). CoChR(C108S) (*n* = 5 cells) had the highest blue-only photocurrents, while sdChR(C138S,E154A) (n = 3 cells) yielded the greatest fractional inhibition by orange light. Switching kinetics are also important: rapid opening is essential for inducing precisely timed action potentials, and rapid closing is essential for inducing high-frequency trains of action potentials. We characterized the opening time (τ_{on}), corresponding to the orange light turning off, and the closing time (τ_{off}), corresponding to the orange light turning on (Fig. 5-5b). All candidates had τ_{off} < 3 ms.

ChR2(C128S,H134R) and sdChR(C138S) had the fastest opening times of 7.5 ± 0.2 and 9.8 ± 0.7 ms, respectively (mean ± s.e.m., *n* = 2 cells for ChR2(C128S,H134R), *n* = 7 cells for sdChR(C138S)).

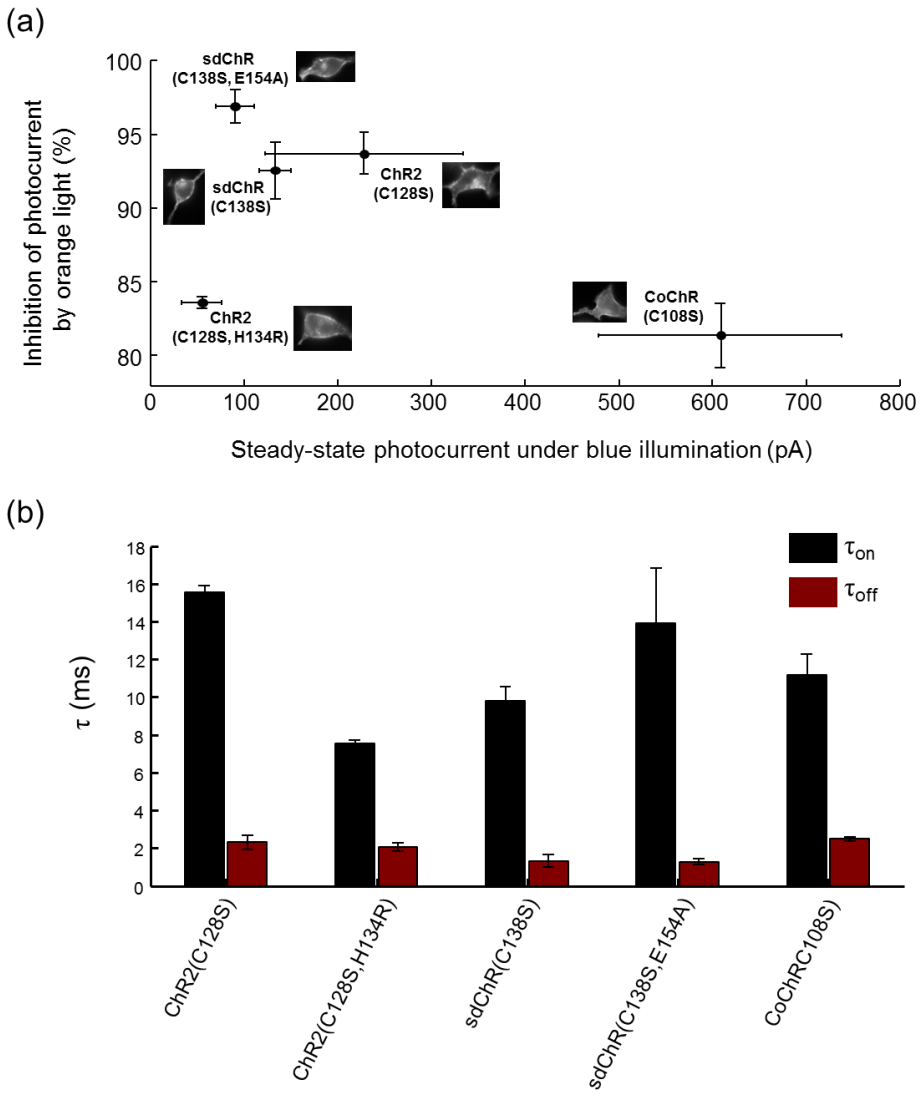

Figure 5-5. (a) Photocurrents (at V = -70 mV) in HEK cells were recorded with steady-state blue illumination (488 nm, 300 mW/cm2) and with simultaneously applied orange illumination (594 nm, 300 W/cm2). Ideal stoplight behavior would yield a large photocurrent under blue-only illumination, and a large fractional inhibition by orange light. b) Kinetics of channel opening (τon) and closing (τoff) under constant blue illumination and modulated orange illumination. Error bars represent s.e.m. on n = 2-7 cells.

5.2.4 Testing the "stoplight" technique in neurons

While no ChR mutant was optimal by all measures, for further characterization in neurons we selected sdChR(C138S, E154A) on account of its >95 % suppression by orange light and CoChR(C108S) on account of its large blue-only photocurrent. We expressed these mutants in cultured rat hippocampal neurons, using calcium phosphate transfection of the constructs in lentiviral vectors under the CaMKIIa promoter. We used manual patch clamp in whole-cell current-clamp mode to monitor the membrane voltage while we varied the blue and orange illumination.

First, we imaged a neuron expressing a WT ChR2-eGFP fusion protein with blue-only illumination, as one might try if one was pairing this conventional channelrhodopsin with a GFP-based fluorophore (Fig. 5-6). One could try to monitor the fluorescence of the fluorophore in response to activity by using intense blue light to induce action potentials, and dim blue light to monitor the reporter in the intervals between the intense stimuli. When the baseline blue intensity was zero, pulses of blue light (488 nm, 3 W/cm^2, 10 ms) robustly induced single action potentials. However, maintaining a constant background of 300 mW/cm^2 significantly depolarized the cell, leading to sodium channel inactivation and a severe distortion of the action potential waveform. At a blue illumination intensity of 3 W/cm^2 the neuron was completely depolarized and ceased firing. These results illustrate the need for a more sophisticated approach to avoiding optical crosstalk.

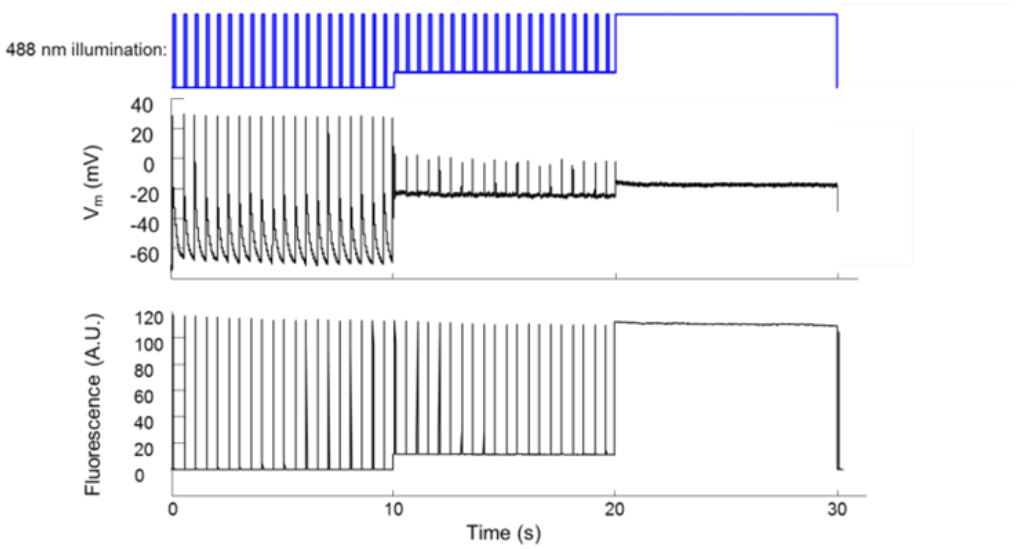

Figure 5-6. Using WT ChR2 to optically induce action potentials while imaging eGFP is difficult. A neuron expressing a WT ChR2 – eGFP fusion protein was subjected to the indicated illumination scheme while the membrane potential of the neuron and the fluorescence of GFP were recorded. From t = 0 s to t = 10 s, the baseline blue intensity was zero, and 10 ms pulses of 488 nm light at 3 W/cm^2 induced action potentials, as expected. From t = 10 s to t = 20 s, baseline blue intensity was increased to 300 W/cm^2 (to mimic a reasonable imaging intensity for a GFP-based reporter). This depolarized the neuron by ~40 mV; addition of 10 ms pulses of 488 nm light at 3 W/cm^2 to this baseline illumination failed to induce action potentials. From t = 20 s to t = 30 s, blue illumination was constant at 3 W/cm^2.

We next expressed sdChR(C138S, E154A) fused to eGFP in a neuron and illuminated the cell with continuous blue light of varying intensity (0 mW/cm^2, 50 mW/cm^2, and 300 mW/cm^2). To control channelrhodopsin activation, we simultaneously illuminated the cell with with orange light (594 nm, 300 W/cm^2) modulated in a square wave with t_{on} = 800 ms and t_{off} = 200 ms (Fig. 5-7). At I_{blue} = 0, the cell showed almost no change in membrane voltage in response to orange modulation. At I_{blue} = 50 mW/cm^2, the cell showed sub-threshold depolarizations when the orange light was off. At I_{blue} = 300 mW/cm^2, the cell fired action potentials when the orange light was off. Importantly, the baseline depolarization was only 5 mV under

300 mW/cm^2 illumination, indicating near complete suppression of the photocurrent by orange light. This imaging condition would be appropriate for monitoring the effect of neural activity on a GFP-based reporter.

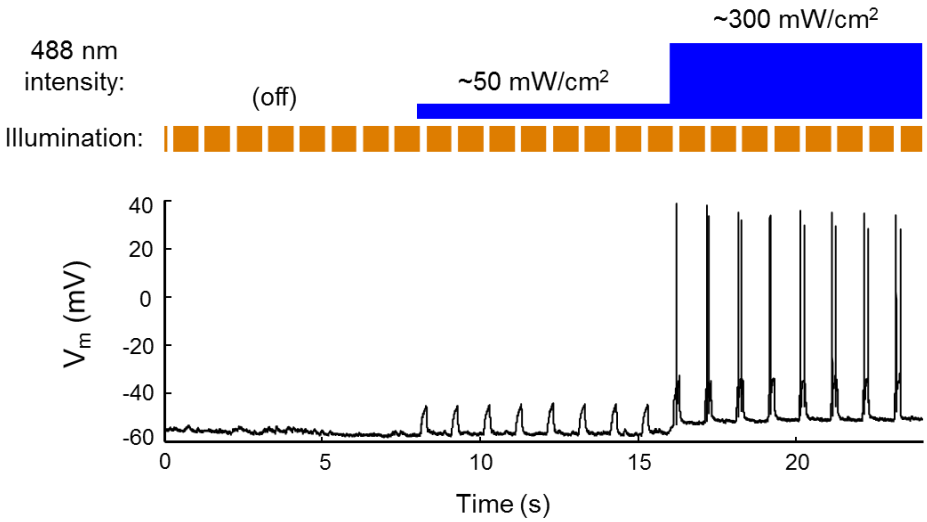

Figure 5-7. Optogenetic control of action potentials under continuous blue illumination using the stoplight technique with sdChR(C138S, E154A). sdChR(C138S,E154A) induces action potentials in cultured rat hippocampal neurons under continuous illumination with 488 nm light (300 mW/cm^2). The neuron only fires when the orange "stoplight" is turned off.

Finally, we tested whether our stoplight technique could be used to monitor calcium transients in response to optically induced activity. We co-expressed CoChR(C108S) and the genetically encoded Ca^{2+} reporter GCaMP6f. We maintained constant illumination at 488 nm (300 mW/cm^2) and temporally modulated illumination at 594 nm (300 W/cm^2). Figure 5-8 shows the experiment. We turned the 594 nm light off every 5 seconds with a variable off time, between 50 and 130 ms, while continuously monitoring the fluorescence of GCaMP6f. Cessation of the orange light induced positive-going transients in the gCaMP6f fluorescence. As we varied the orange t_{off} (corresponding to the CoChR open time), the amplitude of the Ca^{2+} transients grew in

discrete steps, which we ascribe to integer numbers of action potentials. This result demonstrates that one can monitor action potential-induced Ca^{2+} transients using light for stimulus and readout.

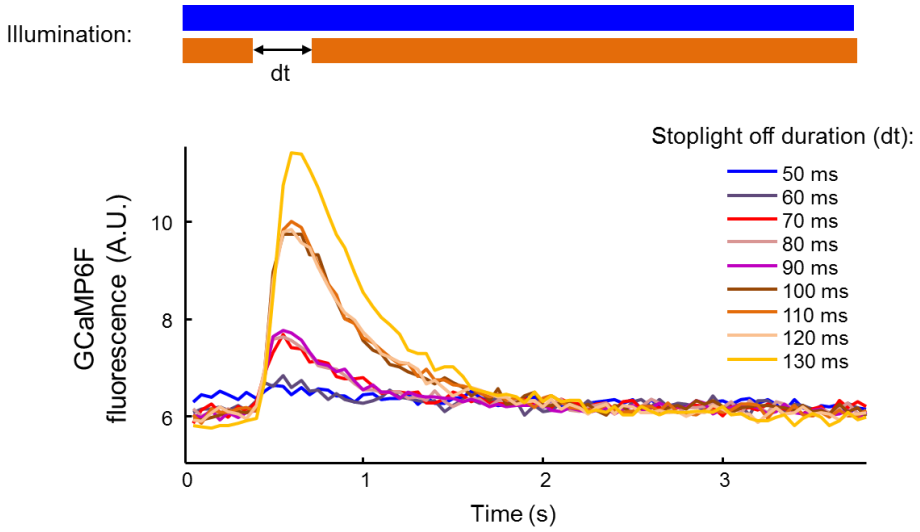

Figure 5-8. Calcium influx varies with the number of action potentials triggered by ChR86(C108S). Stoplight channelrhodopsins can be used in conjunction with GCaMP6F to study activity-dependent changes in $[Ca^{2+}]_i$. Here, continuous illumination at 488 nm (300 mW/cm^2) monitors GCaMP6f fluorescence, while 594 nm illumination (300 W/cm^2) is turned off for a period of time, dt, ranging between 50 ms and 130 ms. Neuronal activity is a function of the stoplight off time (dt).

Unfortunately, clearly interpretable responses as shown in Figure 5-8 occurred in only a minority of cells. More frequently, cells showed a range of complex Ca^{2+} transients which could not be clearly associated to action potentials. We ascribe this complex behavior to lack of dynamic range in the stoplight channelrhodopsins: under strong blue illumination the baseline depolarization was sufficient to partially activated voltage-gated Ca^{2+} channels, even in the presence of the orange stoplight. Under weak blue illumination, the channel opening was so slow that Na^+ channel inactivation prevented action potential firing. For the stoplight technique to become broadly

applicable, it will be necessary to identify channelrhodopsin variants which show larger blue-only photocurrents, and smaller blue-plus-orange photocurrents. These mutants would fall in the (currently empty) upper right-hand corner of Figure 5-5a.

5.3 Discussion

We have explored nonlinear control of channelrhodopsin mutants as a means to modulate photocurrent in neurons while maintaining constant blue light illumination at an intensity appropriate for imaging GFP-based reporters. This "stoplight" technique shows promise, though it suffers primarily from two limitations: first, it requires illumination with highly intense (300 W/cm^2) orange light. This intensity can only be achieved with laser illumination and with a high magnification objective covering a field of view comparable to a single cell. Thus this approach is best suited to neurons in culture. The high intensity illumination creates a risk of photodamage for long-term exposures. Second, the dynamic range of the stoplight is smaller than one might hope. It is worth exploring other mutants to identify stoplight variants that are completely shut by modest orange or red light, and that pass a large photocurrent under modest blue-only illumination.

5.4 Materials and Methods

5.4.1 Molecular biology

We performed point mutagenesis of ChR2, CoChR, and sdChR in a lentiviral vector under the CamKII promoter to generate the SFO constructs used for neuronal expression in this paper: ChR2(C128S)-eGFP, ChR2(C18S, H134R)-eGFP, sdChR(C138S)-TS-eGFP-ER, sdChR(C138S,E154A)-TS-eGFP-ER, and CoChR(C108S)-eGFP. The trafficking sequences (TS and ER) used in ref. [65] were added to sdChR to improve the membrane trafficking of this construct. A similar technique was attempted to improve the membrane trafficking of ChR2, but this was ineffective. CoChR showed excellent membrane trafficking in both HEK cells and neurons and did not need any additional trafficking motifs.

For experiments in HEK-293T cells, the same DNA constructs were used, with the notable exception that we expressed ChR2(C128S) under a ubiquitin promoter (not a CaMKII promoter).

5.4.2 Cell culture

HEK-293T cell culture and DNA transfection was performed as in outlined in Section 3.4.5. For experiments involving primary neuronal cell culture, we followed the protocol outlined in Section 3.4.6. All experimental protocols involving use of animals were approved by the Harvard Institutional Animal Care and Use Committee (IACUC).

5.4.3 Patch-clamp electrophysiology and fluorescence imaging

The microscope that we used to perform both fluorescence imaging and patch-clamp electrophysiology is described in section 3.4.1. All whole cell patch-clamp

experiments in HEK cells were performed under voltage clamp, while experiments in neurons were performed in current clamp mode. We imaged GFP-based fluorophores using excitation at 488 nm; fluorescence was collected on a scientific CMOS camera (Hamamatsu) after passing through a 525/30 emission filter. The extracellular and intracellular buffers that we used for all patch clamp experiments were the same as those described in section 3.4.1. All experiments were performed at 24°C.

Custom software written in MATLAB and LabView, similar to that described in Chapter 3, was used to deliver illumination light of different wavelengths and intensities with sub-millisecond temporal precision. Electrophysiology data was collected at 10 kHz.

5.4.4 Kinetic model

We model the kinetic scheme of Fig. 5-2a, allowing for optical crosstalk between the light-driven transitions. The rates of the transitions are:

$$k_{470 \rightarrow 390} = k_1(I_{blue} + mI_{SL})$$

$$k_{390 \rightarrow 520} = k_2$$

$$k_{520 \rightarrow 470} = k_3(I_{blue} + nI_{SL})$$

where I_{blue} is the blue intensity, I_{SL} is the stoplight intensity, m is the fractional absorption of D470 at λ_{SL} relative to λ_{blue}, and n is the fractional absorption of P520 at λ_{SL} relative to λ_{blue}. Applying mass-balance, one can calculate the steady-state population of each state. The conductance of the membrane is proportional to $[P520]_{ss}$ (we plan to calculate this for each of the illuminations conditions in Fig. 5-4, to test our model).

$$[P520]_{ss} = \frac{k_1 k_2 (I_{blue} + I_{SL} m)}{{I_{blue}}^2 k_1 k_3 + I_{SL}(k_2 k_3 n + k_1 m(k_2 + I_{SL} k_3 n)) + I_{blue}(k_2 k_3 + k_1(k_2 + I_{SL} k_3 (m+n)))}$$

The individual kinetic constants are extracted as follows. In ChR2(C128S), the rise in current upon going from blue-only illumination to darkness occurred with a time constant of 24 ms, so the corresponding rate constant $k_{390 \rightarrow 520}$ = 0.042 ms^{-1}. The fractional increase in steady-state current upon cessation of the blue light is:

$$\frac{[P390]_{ss}}{[P520]_{ss}} = \frac{k_{520 \rightarrow 480}}{k_{390 \rightarrow 420}} = \frac{k_3 (I_{blue} + n I_{SL})}{k_2}$$

The slope of this quantity as a function of I_{blue} (when the stoplight is off) then gives k_3. This slope is 0.013 (r^2 = 0.87); so k_3 = 0.013 cm^2W^{-1} * 0.042 ms^{-1} = 5.5 x 10^{-4} $cm^2W^{-1}ms^{-1}$. In the limit of low intensity blue illumination, the rate constant for channel opening is I_{blue} (k_1 + k_3). A plot of the rate of channel opening vs. I_{blue} has a slope of k_1 + k_3; this slope is 0.22, and k_3 is small, so k_1 = 0.22 $cm^2W^{-1}ms^{-1}$.

Based upon predicted absorption spectra of D470 and P520, we set m = .0005 and n = .45 for λ_{stop} = 594 nm.

References

[1] Park J*, et al.* (2013) Screening fluorescent voltage indicators with spontaneously spiking HEK cells*. PLoS One* 8:e85221.

[2] Maclaurin D, Venkatachalam V, Lee H, Cohen AE (2013) Mechanism of voltage-sensitive fluorescence in a microbial rhodopsin*. Proc Natl Acad Sci USA* 110:5939-5944.

[3] Venkatachalam V*, et al.* (2014) Flash memory: photochemical imprinting of neuronal action potentials onto a microbial rhodopsin*. J Am Chem Soc* 136:2529-2537.

[4] Hou JH, Venkatachalam V, Cohen AE (2014) Temporal Dynamics of Microbial Rhodopsin Fluorescence Reports Absolute Membrane Voltage*. Biophys J* 106:639-648.

[5] Ihara K*, et al.* (1999) Evolution of the archaeal rhodopsins: evolution rate changes by gene duplication and functional differentiation*. J Mol Biol* 285:163-174.

[6] Chow BY*, et al.* (2010) High-performance genetically targetable optical neural silencing by light-driven proton pumps*. Nature* 463:98-102.

[7] Kralj JM, Douglass AD, Hochbaum DR, Maclaurin D, Cohen AE (2012) Optical recording of action potentials in mammalian neurons using a microbial rhodopsin*. Nat Meth* 9:90-95.

[8] Kralj JM, Douglass AD, Hochbaum DR, Maclaurin D, Cohen AE (2011) Optical recording of action potentials in mammalian neurons using a microbial rhodopsin*. Nat Methods* 9:90-95.

[9] Boyden ES, Zhang F, Bamberg E, Nagel G, Deisseroth K (2005) Millisecond-timescale, genetically targeted optical control of neural activity*. Nat Neurosci* 8:1263-1268.

[10] Kralj JM, Hochbaum DR, Douglass AD, Cohen AE (2011) Electrical spiking in Escherichia coli probed with a fluorescent voltage indicating protein*. Science* 333:345-348.

[11] Scanziani M, Hausser M (2009) Electrophysiology in the age of light*. Nature* 461:930-939.

[12] Peterka DS, Takahashi H, Yuste R (2011) Imaging voltage in neurons*. Neuron* 69:9-21.

[13] Kaestner L, Tian Q, Lipp P (2012) Action potentials in heart cells. *Fluorescent Proteins II* 163-182.

[14] Adams DS, Masi A, Levin M (2007) H^+ pump-dependent changes in membrane voltage are an early mechanism necessary and sufficient to induce Xenopus tail regeneration. *Science STKE* 134:1323.

[15] Martinac B, Saimi Y, Kung C (2008) Ion channels in microbes. *Physiol Rev* 88:1449.

[16] Cohen LB, Keynes RD, Hille B (1968) Light scattering and birefringence changes during nerve activity. *Nature* 218:438-441.

[17] Tasaki I, Watanabe A, Sandlin R, Carnay L (1968) Changes in fluorescence, turbidity, and birefringence associated with nerve excitation. *Proc Natl Acad Sci U S A* 61:883-888.

[18] Chattoraj M, King BA, Bublitz GU, Boxer SG (1996) Ultra-fast excited state dynamics in green fluorescent protein: multiple states and proton transfer. *Proc Natl Acad Sci U S A* 93:8362.

[19] Enami N, *et al.* (2006) Crystal structures of archaerhodopsin-1 and-2: Common structural motif in archaeal light-driven proton pumps. *J Mol Biol* 358:675-685.

[20] Cartailler JP, Luecke H (2003) X-Ray Crystallographic Analysis of Lipid-Protein Interactions in the Bacteriorhodopsin Purple Membrane*. *Annu Rev Biophys Biomol Struct* 32:285-310.

[21] Varo G, Lanyi JK (1991) Thermodynamics and energy coupling in the bacteriorhodopsin photocycle. *Biochemistry (N Y)* 30:5016-5022.

[22] Varo G, Lanyi JK (1991) Kinetic and spectroscopic evidence for an irreversible step between deprotonation and reprotonation of the Schiff base in the bacteriorhodopsin photocycle. *Biochemistry* 30:5008-5015.

[23] Spudich JL, Yang CS, Jung KH, Spudich EN (2000) Retinylidene proteins: structures and functions from archaea to humans. *Annu Rev Cell Dev Biol* 16:365-392.

[24] Brown LS, Dioumaev AK, Needleman R, Lanyi JK (1998) Local-access model for proton transfer in bacteriorhodopsin. *Biochemistry (N Y)* 37:3982-3993.

[25] Brown LS, Dioumaev AK, Needleman R, Lanyi JK (1998) Connectivity of the retinal Schiff base to Asp85 and Asp96 during the bacteriorhodopsin photocycle: the local-access model. *Biophys J* 75:1455.

[26] Popp A, Wolperdinger M, Hampp N, Brüchle C, Oesterhelt D (1993) Photochemical conversion of the O-intermediate to 9-cis-retinal-containing products in bacteriorhodopsin films. *Biophys J* 65:1449-1459.

[27] Yamamoto N, Naramoto S, Ohtani H (1992) Photoreaction of N560 intermediate in the photocycle of bacteriorhodopsin. *FEBS Lett* 314:345-347.

[28] Ohtani H, Itoh H, Shinmura T (1992) Time-resolved fluorometry of purple membrane of Halobacterium halobium O640 and an O-like red-shifted intermediate Q. *FEBS Lett* 305:6-8.

[29] Ohtani H, Kikuchi O (1999) Excitation Spectrum of the N Intermediate in the Photocycle of Bacteriorhodopsin. *J Phys Chem B* 103:8186-8188.

[30] Dancshazy Z, Helgerson S, Stoeckenius W (1983) Coupling between the bacteriorhodopsin photocycle kinetics and the protonmotive force. I. Single flash measurements in Halobacterium halobium cells. *Photobiochem Photobiophys* 5:347-357.

[31] Groma G*, et al.* (1984) Coupling between the bacteriorhodopsin photocycle and the protonmotive force in Halobacterium halobium cell envelope vesicles. II. Quantitation and preliminary modeling of the M----bR reactions. *Biophys J* 45:985-992.

[32] Quintanilha A (1980) Control of the photocycle in bacteriorhodopsin by electrochemical gradients. *FEBS Lett* 117:8.

[33] Geibel S*, et al.* (2001) The voltage-dependent proton pumping in bacteriorhodopsin is characterized by optoelectric behavior. *Biophys J* 81:2059-2068.

[34] Nagel G, Kelety B, Möckel B, Büldt G, Bamberg E (1998) Voltage dependence of proton pumping by bacteriorhodopsin is regulated by the voltage-sensitive ratio of M1 to M2. *Biophys J* 74:403-412.

[35] del Rosario RCH, Oppawsky C, Tittor J, Oesterhelt D (2010) Modeling the membrane potential generation of bacteriorhodopsin. *Math Biosci* 225:68-80.

[36] Tsunoda SP*, et al.* (2006) H^+ -pumping rhodopsin from the marine alga Acetabularia. *Biophys J* 91:1471-1479.

[37] Bogomolni RA, Stubbs L, Lanyi JK (1978) Illumination-dependent changes in the intrinsic fluorescence of bacteriorhodopsin. *Biochemistry (N Y)* 17:1037-1041.

[38] Du M, Fleming GR (1993) Femtosecond time-resolved fluorescence spectroscopy of bacteriorhodopsin: direct observation of excited state dynamics in the primary step of the proton pump cycle. *Biophys Chem* 48:101-111.

[39] Kamiya N*, et al.* (1997) Picosecond fluorescence spectroscopy of the purple membrane of Halobacterium halobium in alkaline suspension. *Chemical Physics Letters* 265:595-599.

[40] Mukohata Y, Ihara K, Uegaki K, Mlyashita Y, Sugiyama Y (1991) Australian Halobacteria and their retinal-protein ion pumps. *Photochem Photobiol* 54:1039-1045.

[41] Ludmann K, Gergely C, Váró G (1998) Kinetic and thermodynamic study of the bacteriorhodopsin photocycle over a wide pH range. *Biophys J* 75(6):3110-3119.

[42] Scherrer P, Mathew M, Sperling W, Stoeckenius W (1989) Retinal isomer ratio in dark-adapted purple membrane and bacteriorhodopsin monomers. *Biochemistry (N Y)* 28:829-834.

[43] Stoeckenius W, Bogomolni RA (1982) Bacteriorhodopsin and related pigments of halobacteria. *Annu Rev Biochem* 51:587-616.

[44] Ohtani H, Kaneko M, Ishikawa M, Kamiya N, Yamamoto N (1999) Picosecond-millisecond dual-time-base spectroscopy of fluorescent photointermediates formed in the purple membrane of Halobacterium halobium. *Chem Phys Lett* 299:571-575.

[45] Zimanyi L*, et al.* (1992) Pathways of proton release in the bacteriorhodopsin photocycle. *Biochemistry (N Y)* 31:8535-8543.

[46] Hillebrecht JR*, et al.* (2005) Optimization of protein-based volumetric optical memories and associative processors by using directed evolution. *NanoBiotechnology* 1:141-151.

[47] El-Sayed WSM*, et al.* (2002) Effects of light and low oxygen tension on pigment biosynthesis in Halobacterium salinarum, revealed by a novel method to quantify both retinal and carotenoids. *Plant and Cell Physiology* 43:379-383.

[48] Ragan T*, et al.* (2012) Serial two-photon tomography for automated ex vivo mouse brain imaging. *Nat Meth* 9:255-258.

[49] Chung K*, et al.* (2013) Structural and molecular interrogation of intact biological systems. *Nature* 497:332-337.

[50] Takemura S*, et al.* (2013) A visual motion detection circuit suggested by Drosophila connectomics*. Nature* 500:175-181.

[51] Helmstaedter M*, et al.* (2013) Connectomic reconstruction of the inner plexiform layer in the mouse retina*. Nature* 500:168-174.

[52] Cai D, Cohen KB, Luo T, Lichtman JW, Sanes JR (2013) Improved tools for the Brainbow toolbox*. Nat Meth* 10:540-547.

[53] Chen T*, et al.* (2013) Ultrasensitive fluorescent proteins for imaging neuronal activity*. Nature* 499:295-300.

[54] Cao G*, et al.* (2013) Genetically Targeted Optical Electrophysiology in Intact Neural Circuits*. Cell* 154:904-913.

[55] Ahrens MB, Orger MB, Robson DN, Li JM, Keller PJ (2013) Whole-brain functional imaging at cellular resolution using light-sheet microscopy*. Nat Meth* 10:413-420.

[56] Guenthner CJ, Miyamichi K, Yang HH, Heller HC, Luo L (2013) Permanent Genetic Access to Transiently Active Neurons via TRAP: Targeted Recombination in Active Populations*. Neuron* 78:773-784.

[57] Zamft BM*, et al.* (2012) Measuring Cation Dependent DNA Polymerase Fidelity Landscapes by Deep Sequencing*. PLoS One* 7:e43876.

[58] Peron S, Svoboda K (2010) From cudgel to scalpel: toward precise neural control with optogenetics*. Nat Meth* 8:30-34.

[59] Ntziachristos V (2010) Going deeper than microscopy: the optical imaging frontier in biology*. Nat Meth* 7:603-614.

[60] Tsukamoto H, Terakita A (2010) Diversity and functional properties of bistable pigments*. Photochem Photobiol Sci* 9:1435-1443.

[61] Wagner NL, Greco JA, Ranaghan MJ, Birge RR (2013) Directed evolution of bacteriorhodopsin for applications in bioelectronics*. J R Soc Interface* 10:20130197.

[62] Manor D, Hasselbacher C, Spudich JL (1988) Membrane potential modulates photocycling rates of bacterial rhodopsins*. Biochemistry (N Y)* 27:5843-5848.

[63] Kolodner P, Lukashev EP, Ching Y, Rousseau DL (1996) Electric-field-induced Schiff-base deprotonation in D85N mutant bacteriorhodopsin*. Proc Natl Acad Sci U S A* 93:11618-11621.

[64] Gong Y, Li JZ, Schnitzer MJ (2013) Enhanced Archaerhodopsin Fluorescent Protein Voltage Indicators. *PLoS One* 8:e66959.

[65] Gradinaru V, *et al.* (2010) Molecular and Cellular Approaches for Diversifying and Extending Optogenetics. *Cell* 141:154-165.

[66] Mattis J, *et al.* (2012) Principles for applying optogenetic tools derived from direct comparative analysis of microbial opsins. *Nature Methods* 9:159-172.

[67] Goslin K (1998) *Culturing nerve cells* (The MIT Press, Cambridge, MA).

[68] Zou P, *et al.* (2014) Bright and fast voltage reporters across the visible spectrum via electrochromic FRET (eFRET). *ArXiv Preprint arXiv:1403.4636*

[69] Jin L, *et al.* (2012) Single action potentials and subthreshold electrical events imaged in neurons with a fluorescent protein voltage probe. *Neuron* 75:779-785.

[70] Lam AJ, *et al.* (2012) Improving FRET dynamic range with bright green and red fluorescent proteins. *Nat Meth* 9:1005-1012.

[71] Akemann W, Mutoh H, Perron A, Rossier J, Knöpfel T (2010) Imaging brain electric signals with genetically targeted voltage-sensitive fluorescent proteins. *Nat Methods* 7:643-649.

[72] Tsutsui H, Higashijima S, Miyawaki A, Okamura Y (2010) Visualizing voltage dynamics in zebrafish heart. *J Physiol* 588:2017-2021.

[73] Aw S, *et al.* (2010) The ATP-sensitive K -channel (KATP) controls early left-right patterning in Xenopus and chick embryos. *Dev Biol* 346:39-39-53.

[74] Sundelacruz S, Levin M, Kaplan DL (2009) Role of membrane potential in the regulation of cell proliferation and differentiation. *Stem Cell Rev* 5:231-246.

[75] Beane WS, Morokuma J, Adams DS, Levin M (2011) A Chemical Genetics Approach Reveals H, K-ATPase-Mediated Membrane Voltage Is Required for Planarian Head Regeneration. *Chem Biol* 18:77-89.

[76] Nicholls DG, Ward MW (2000) Mitochondrial membrane potential and neuronal glutamate excitotoxicity: mortality and millivolts. *Trends Neurosci* 23:166-174.

[77] Mousavi SA, Chauvin A, Pascaud F, Kellenberger S, Farmer EE (2013) GLUTAMATE RECEPTOR-LIKE genes mediate leaf-to-leaf wound signalling. *Nature* 500:422-426.

[78] Volkov AG (2006) *Plant electrophysiology,* (Springer, Berlin),

[79] Spudich JL (2006) The multitalented microbial sensory rhodopsins. *Trends Microbiol* 14:480-487.

[80] Rangaraju V, Calloway N, Ryan TA (2014) Activity-driven local ATP synthesis is required for synaptic function. *Cell* 156:825-835.

[81] Cohen AE, Venkatachalam V (2014) Bringing bioelectricity to light. *Annu Rev Biophys* in press:

[82] Nikolenko V, Poskanzer KE, Yuste R (2007) Two-photon photostimulation and imaging of neural circuits. *Nat Meth* 4:943-950.

[83] Kwon HB, Sabatini BL (2011) Glutamate induces de novo growth of functional spines in developing cortex. *Nature* 474:100-104.

[84] Kokel D*, et al.* (2013) Photochemical activation of TRPA1 channels in neurons and animals. *Nature Chemical Biology* 9:257-263.

[85] Kramer RH, Mourot A, Adesnik H (2013) Optogenetic pharmacology for control of native neuronal signaling proteins. *Nat Neurosci* 16:816-823.

[86] Levitz J*, et al.* (2013) Optical control of metabotropic glutamate receptors. *Nat Neurosci* 16:507-516.

[87] Packer AM, Roska B, Häusser M (2013) Targeting neurons and photons for optogenetics. *Nat Neurosci* 16:805-815.

[88] Yizhar O, Fenno LE, Davidson TJ, Mogri M, Deisseroth K (2011) Optogenetics in neural systems. *Neuron* 71:9-34.

[89] Klapoetke NC*, et al.* (2014) Independent optical excitation of distinct neural populations. *Nat Meth* 11:338-346.

[90] Wietek J*, et al.* (2014) Conversion of channelrhodopsin into a light-gated chloride channel. *Science* 344:409-412.

[91] Berndt A, Lee SY, Ramakrishnan C, Deisseroth K (2014) Structure-guided transformation of channelrhodopsin into a light-activated chloride channel. *Science* 344:420-424.

[92] Depry C, Mehta S, Zhang J (2013) Multiplexed visualization of dynamic signaling networks using genetically encoded fluorescent protein-based biosensors. *Pflügers Archiv-European Journal of Physiology* 465:373-381.

[93] Mehta S, Zhang J (2011) Reporting from the field: genetically encoded fluorescent reporters uncover signaling dynamics in living biological systems. *Annu Rev Biochem* 80:375-401.

[94] Shaner NC, Steinbach PA, Tsien RY (2005) A guide to choosing fluorescent proteins. *Nat Meth* 2:905.

[95] Vogt KE, Gerharz S, Graham J, Canepari M (2011) Combining membrane potential imaging with L-glutamate or GABA photorelease. *PLoS One* 6:e24911.

[96] Tsuda S, *et al.* (2012) Probing the function of neuronal populations: combining micromirror-based optogenetic photostimulation with voltage-sensitive dye imaging. *Neurosci Res* 75:76-81.

[97] Lim DH, *et al.* (2012) In vivo Large-Scale Cortical Mapping Using Channelrhodopsin-2 Stimulation in Transgenic Mice Reveals Asymmetric and Reciprocal Relationships between Cortical Areas. *Front Neural Circuits* 6:11.

[98] Wu J, *et al.* (2013) Improved orange and red Ca^{2+} indicators and photophysical considerations for optogenetic applications. *ACS Chem Neuro* 4:963-972.

[99] Zhao Y, *et al.* (2011) An expanded palette of genetically encoded Ca^{2+} indicators. *Science* 333:1888-1891.

[100] Canepari M, Zecevic D, Vogt KE, Ogden D, De Waard M (2013) Combining calcium imaging with other optical techniques. *Cold Spring Harbor Protocols* 2013:pdb. top066167.

[101] Hochbaum DR, *et al.* (2014) All-optical electrophysiology in mammalian neurons using engineered microbial rhodopsins. *Submitted*

[102] Berndt A, Yizhar O, Gunaydin LA, Hegemann P, Deisseroth K (2009) Bi-stable neural state switches. *Nat Neurosci* 12:229-234.

[103] Nagel G, *et al.* (2005) Light activation of channelrhodopsin-2 in excitable cells of *Caenorhabditis elegans* triggers rapid behavioral responses. *Curr Biol* 15:2279-2284.